R&D STUDIES ON THE HADRONIC CALORIMETER AND PHYSICS

SIMULATIONS ON THE STANDARD MODEL AND MINIMAL

SUPERSYMMETRIC STANDARD MODEL HIGGS BOSONS IN THE CMS

EXPERIMENT

by

Firdevs Duru

A thesis submitted in partial fulfillment
of the requirements for the Doctor of
Philosophy degree in Physics
in the Graduate College of
The University of Iowa

July 2007

Thesis Supervisor: Professor Yasar Onel

Graduate College
The University of Iowa
Iowa City, Iowa

CERTIFICATE OF APPROVAL

_____

PH.D. THESIS

_____

This is to certify that the Ph.D. thesis of

Firdevs Duru

has been approved by the Examining Committee
for the thesis requirement for the Doctor of Philosophy
degree in Physics at the July 2007 graduation.

Thesis Committee: _____
                  Yasar Onel, Thesis Supervisor

                  _____
                  Mary Hall Reno

                  _____
                  Edwin Norbeck

                  _____
                  Paul D. Kleiber

                  _____
                  Tuong Ton-That

To my parents Zuhal Duru and Ismail Hakki Duru, and my sister Nadire Duru.
Without them this would not be possible.

I am not leaving a spiritual legacy of dogmas, unchangeable petrified directives. My spiritual legacy is science and reason.

Science is the most reliable guide for civilization, for life, for success in the world. Searching for a guide other than the science is carelessness, ignorance and heresy.

Mustafa Kemal ATATURK
The founder of Turkish Republic

ABSTRACT

This thesis consists of two main parts: R&D studies done on the Compact Muon Solenoid (CMS) Hadronic Calorimeter (HCAL) and physics simulations on the Higgs boson for a Minimal Supersymmetric Standard Model (MSSM) and a Standard Model (SM) channel. In the first part, the air core light guides used in the read-out system of the Hadronic Forward (HF) calorimeter and the reflective materials used in them are studied. Then, tests and simulations were performed to find the most efficient way to collect Čerenkov light from the quartz plates, which are proposed as a substitute for the scintillator tiles in the Hadronic Endcap (HE) calorimeter due to radiation damage problems.

In the second part physics simulations and their results are presented. The MSSM channel H/A→ττ →l l υ υ υ υ is studied to investigate the jet and missing transverse energy (MET) reconstruction of the CMS detector. The effects of the jet and MET corrections on the Higgs boson mass reconstruction are investigated. In the last part the SM channel gg → HH → (W⁺ W⁻)(W⁺ W⁻) → (j j μ υ) (j j μ υ) is simulated using fast simulation software of the CMS. The results at every step of the simulation are compared to the theoretical results from previous studies.

TABLE OF CONTENTS

LIST OF TABLES

LIST OF FIGURES

Figure

INTRODUCTION

<u>The Large Hadron Collider and the Compact Muon</u>

<u>Solenoid Experiment</u>

The University of Iowa is a participating institute in the Compact Muon Solenoid (CMS) experiment [1, 2] of the Large Hadron Collider (LHC) project at the European Organization for Nuclear Research (CERN), in Geneva, Switzerland (see Figure I.1). Hardware projects to improve the CMS detector, as well as physics simulations are being performed at The University of Iowa.

Figure I.1: Arial view of the LHC at the border of Switzerland and France.

LHC, soon to be the largest hadron collider in the world, is scheduled to become operational in 2008, while the engineering runs will begin in September 2007. The collider will be placed in the already existing LEP (Large Electron-Positron Storage) tunnel (Figure I.2) at the border of Switzerland and France, and it will provide proton-proton collisions with a center of mass energy $\sqrt{s} = 14$ TeV.

Figure I.2: The LEP tunnel.

A linear accelerator (LINAC) will speed protons up to 50 MeV followed by a Booster up to 1.4 GeV, a (proton synchrotron) PS up to 25 GeV and the (super proton syncrotron) SPS up to 450 GeV. In the final stage, protons will be injected into LHC

where they will be accelerated up to 7 GeV. The schematic view of the accelerator complex is shown in Figure I.3.
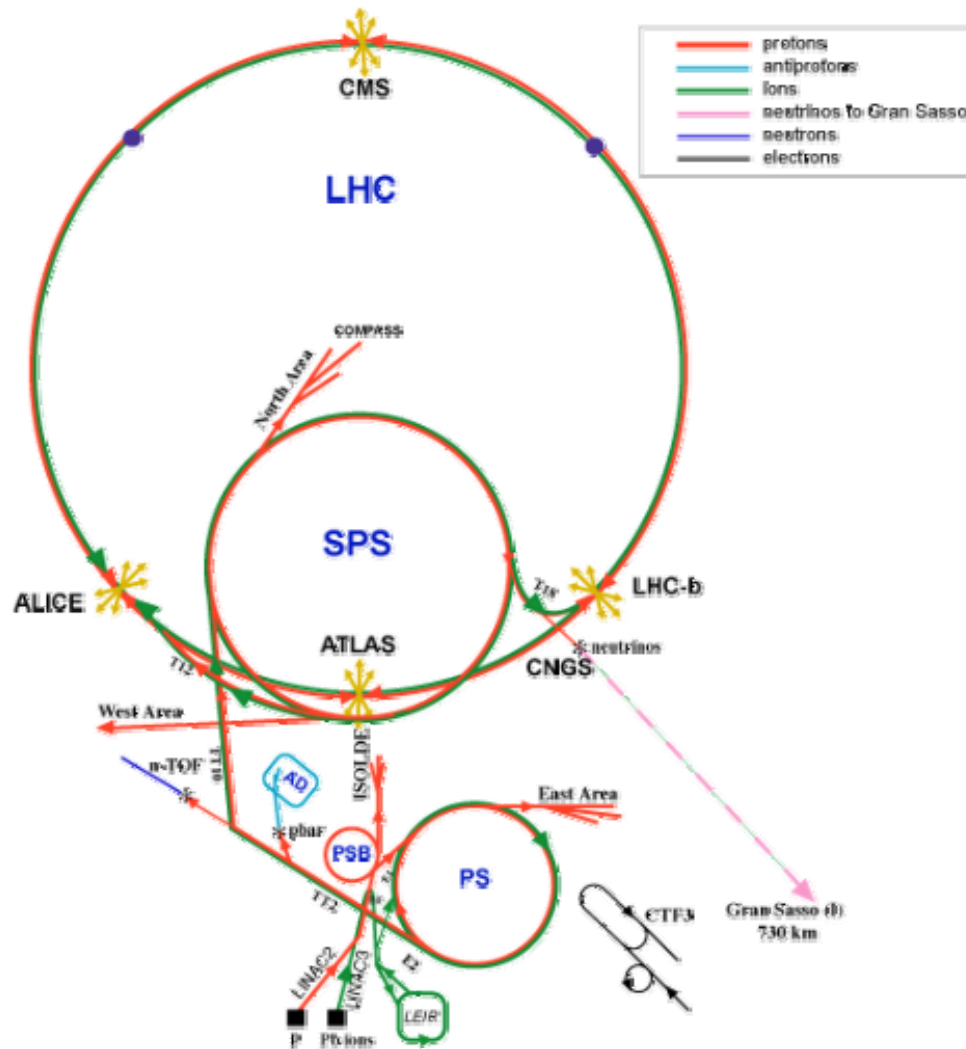
Figure I.3: The accelerator complex at CERN which is a succession of machines with increasingly higher energies, injecting the beam each time into the next one [3].

The beam luminosity will reach 10^{34} cm^{-2} s^{-1}, the bunch separation will be 24.95 ns, and every bunch will contain 10^{11} protons. The constituents of the protons carry a

fraction of the proton energy. They will interact with each other during the collision and exchange a fraction of the initial proton energy. Each collision will result in a different type of event, determined by the cross section of possible interactions. The cross section for some processes as a function of the center of mass system in proton-proton collisions is shown in Figure I.4.
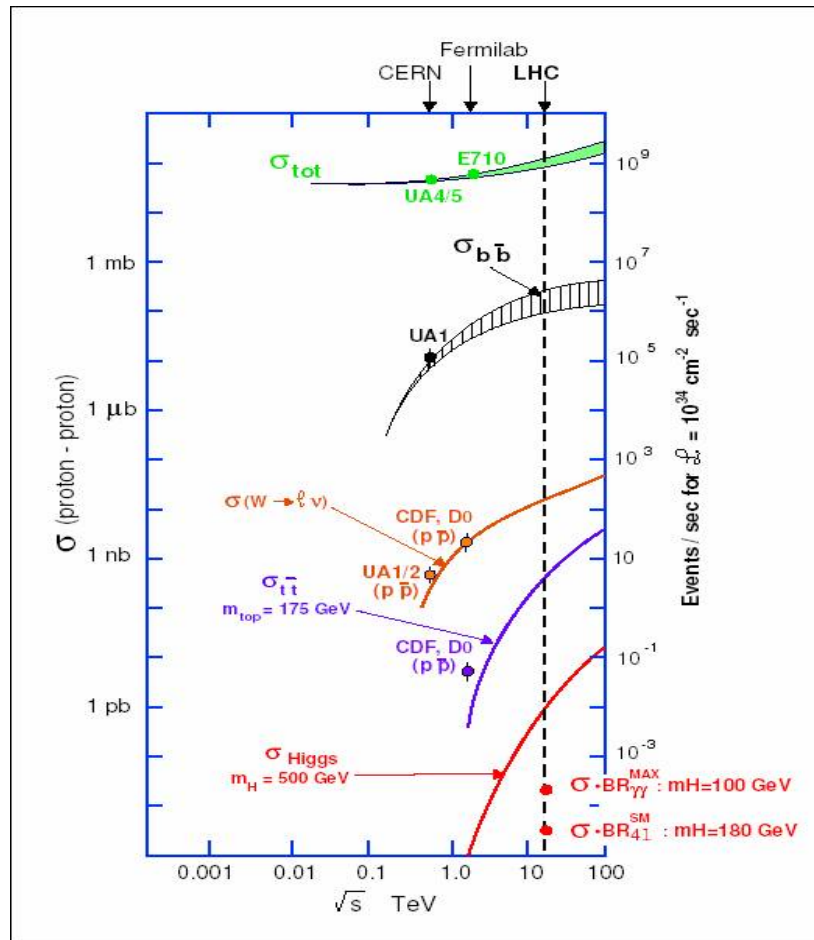
Figure I.4: Event rates and cross sections of some physics processes as changing center of mass energy [5].

The luminosity L is proportional to the number of particles (n_1 and n_2) at each beam and to the revolution frequency f. It is given by:

$$L = \frac{f n_1 n_2}{4 \pi \sigma_x \sigma_y},$$

where σ_x and σ_y are the widths characterizing the Gaussian transverse beam profiles in the horizontal and vertical directions respectively. The cross section multiplied by the luminosity gives the rate of a process: $R = L \times \sigma$ [4].

In addition to proton-proton collisions, the LHC will also provide heavy ion [6] (such as Pb) beams reaching center of mass energies up to 5.52 TeV per nucleon. Table I.1 lists the parameter values for proton-proton and heavy ion collisions at the LHC.

Parameters	pp	PbPb
Center of mass energy (TeV)	14	5.52
Number of bunches	2808	592
Number of particles per bunch	$\sim 10^{11}$	$\sim 5 \times 10^7$
Bunch spacing (ns)	25	100
Luminosity (cm^{-2} s^{-1})	10^{34}	10^{27}
Luminosity lifetime (h)	15	6

Table I.1: LHC parameters for pp and ^{208}Pb^{82+} ^{208}Pb^{82+} collisions.

There are four primary detectors at the LHC: The CMS detector, the ATLAS Detector [7], ALICE [8] and LHCb [9]. The first two are multi-purpose detectors which will record interactions created by both proton-proton and heavy ion collisions. ALICE is primarily designed for heavy ion collisions and LHCb will search for B-mesons produced in proton collisions. Figure I.5 is a schematic view of the LHC accelerator and the experiments mentioned above. The tunnel is 100 m below the ground and has a circumference of 27 km.
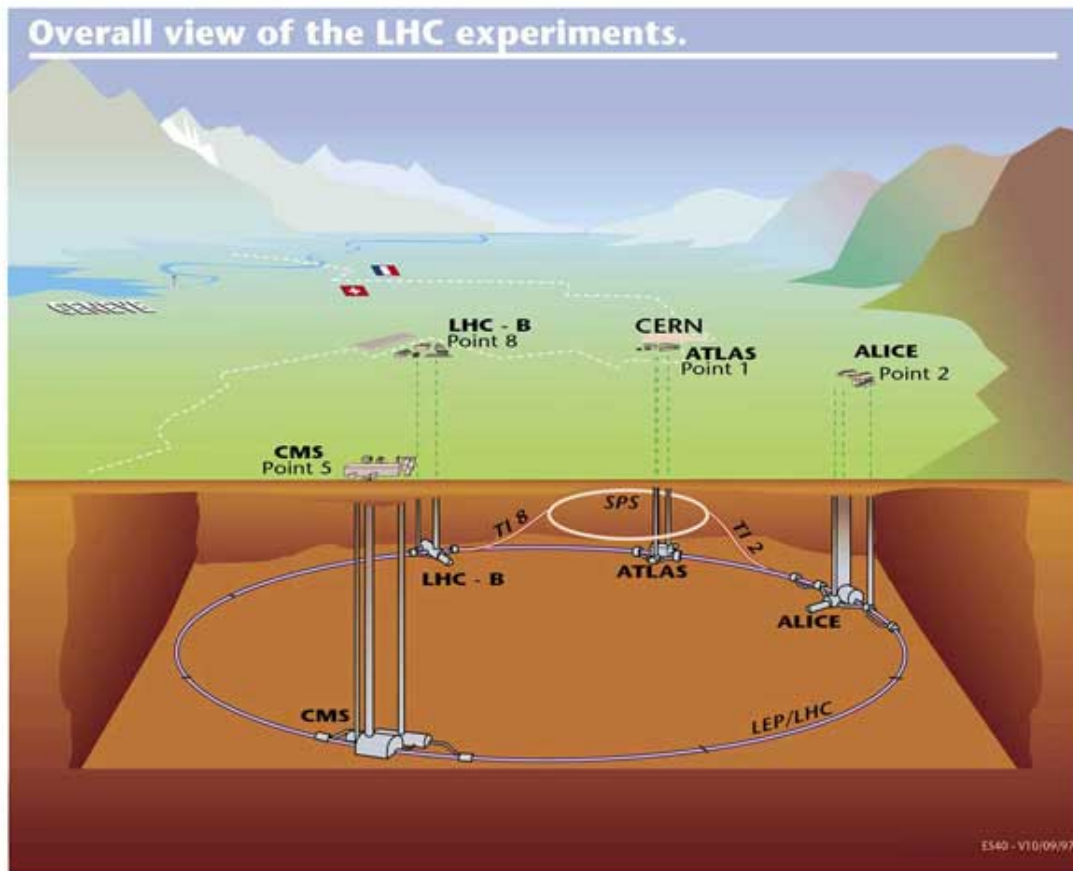
Figure I.5: The four big experiments at the LHC: CMS, ATLAS, ALICE, and LHC-B.

CMS Overview

Physics Performance

One of the main physics goals of the LHC is to finalize the argument for the existence of the Higgs boson and to measure its properties. In addition, it will search for new physics at the TeV energy scale.

The CMS detector at the LHC has been designed to cleanly detect the diverse signatures from new physics by identifying and precisely measuring muons, electrons and

photons over a large energy range and at high luminosity. It is also aimed to take advantage of the expected lower luminosity that will be running in the early years of the LHC [1]. Table I.2 summarizes the event rates for some physics processes at the LHC for a luminosity of L = 2 x 10^{33} cm^{-2} s^{-1}.

Physics Process	Events / s	Events / year
W $\rightarrow$ e υ	40	4 x 10^8
Z $\rightarrow$ e e	4	4 x 10^7
t $\bar{t}$	1.6	1.6 x 10^7
b $\bar{b}$	10^6	10^{13}
$\widetilde{g}\widetilde{g}$ (m = 1 TeV)	0.002	2 x 10^4
Higgs (m = 120 GeV)	0.08	8 x 10^5
Higgs (m = 800 GeV)	0.001	10^4
QCD jets p_T > 200 GeV	10^2	10^9

Table I.2: Event rates for several physics processes at the LHC for a luminosity of L=2x10^{33} cm^{-2}s^{-1} [10].
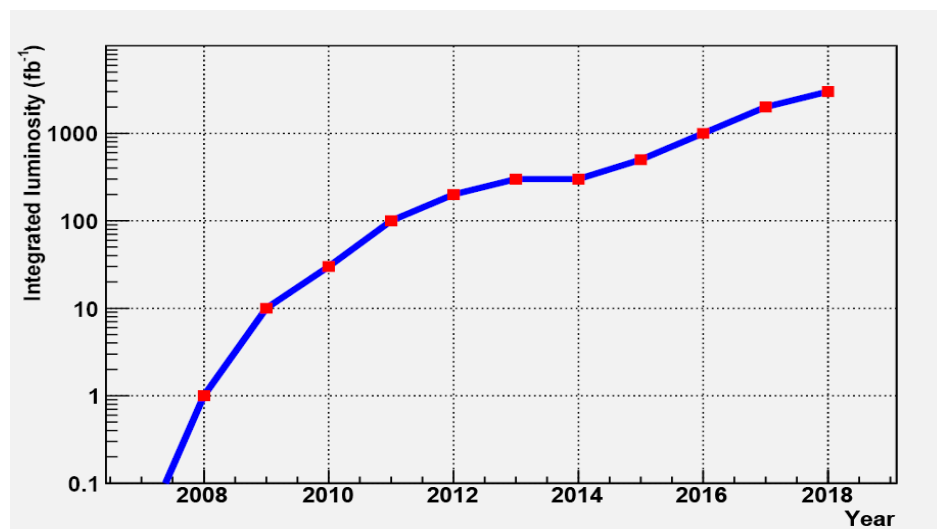
Figure I.6: The luminosity profile of the LHC.

For some standard physics processes, a single day of data taking at the LHC, corresponds to ten years of operation at previous machines, in terms of event statistics [11]. The LHC will have ~100 times the luminosity of the Tevatron where the CDF and D0 experiments successfully found the top quark, which has a cross section ~10^{-10} the total cross section. The luminosity profile of the LHC over the years is shown in Figure I.6.

Studies have been done of the performance of the CMS in detection and measurement of various physics signals from proton-proton and heavy ion collisions. The wide range of physics interests of the CMS can be summarized as: Searches for the Standard Model (SM) Higgs boson and the various Minimum Supersymmetric Standard Model (MSSM) Higgs bosons, gluino, squark searches, CP-violation measurements in the B sector, observation of B_s^0 oscillations, and possible signals for QCD deconfinement via the relative suppression within the γ family in heavy ion collisions, top physics, searches for the new heavy gauge bosons and resonant strong interaction spontaneous symmetry-breaking models [10]. Studies on CP-violation and supersymmetry may answer questions about the origin of the matter-antimatter asymmetry of the universe and of the dark matter [12].

The data obtained by the LHC should provide information about the electroweak symmetry breaking mechanism and provide evidence for the existence of physics beyond the standard model. If the Higgs and SUSY (supersymmetric) sparticles have TeV scale masses, the LHC will be able to produce many of them along with W and Z bosons, b and top quarks. The large number of particles produced will allow precision measurements to

be made. Also, heavy ion collisions will clarify the quark-gluon plasma, and the formation of a deconfined state of hadronic matter.

CMS Detector

The CMS detector [1, 2] (see Figure I.7 and I.8) is a 21.6 m long (very forward calorimeters excluded) cylinder with a 14.6 m diameter and a total weight of 14,500 tons. It is azimuthally symmetric. The detector, which has almost 4π solid angle coverage, is made of four main subsystems: magnet, muon system, tracking and calorimetry. The centre of the detector is placed in a 4 Tesla magnetic field parallel to the beam direction. In the CMS reference frame, the x-axis is towards the center of the collider, the y-axis points upward and the z-axis is along the beam direction. However, most of the time, a pseudo-spherical coordinate system which, in the transverse plane, is defined by the radius r, the azimuthal angle Φ with respect to y-axis and the polar angle θ with respect to z-axis for which instead of the polar angle the pseudorapidty η is used. The pseudorapidity is an approximation of the rapidity y given by $y = \frac{1}{2}\ln(E + P_z)/(E - P_z)$ where E is the energy and P is the momentum of the particle. The pseudorapidity is a good approximation of the rapidity when $P \gg$ m and $\theta \gg 1/\gamma$.

A high performance muon system, a high resolution electromagnetic calorimeter, a high quality central tracking system and a full calorimetric coverage are the main design objectives of the CMS calorimeter [13].
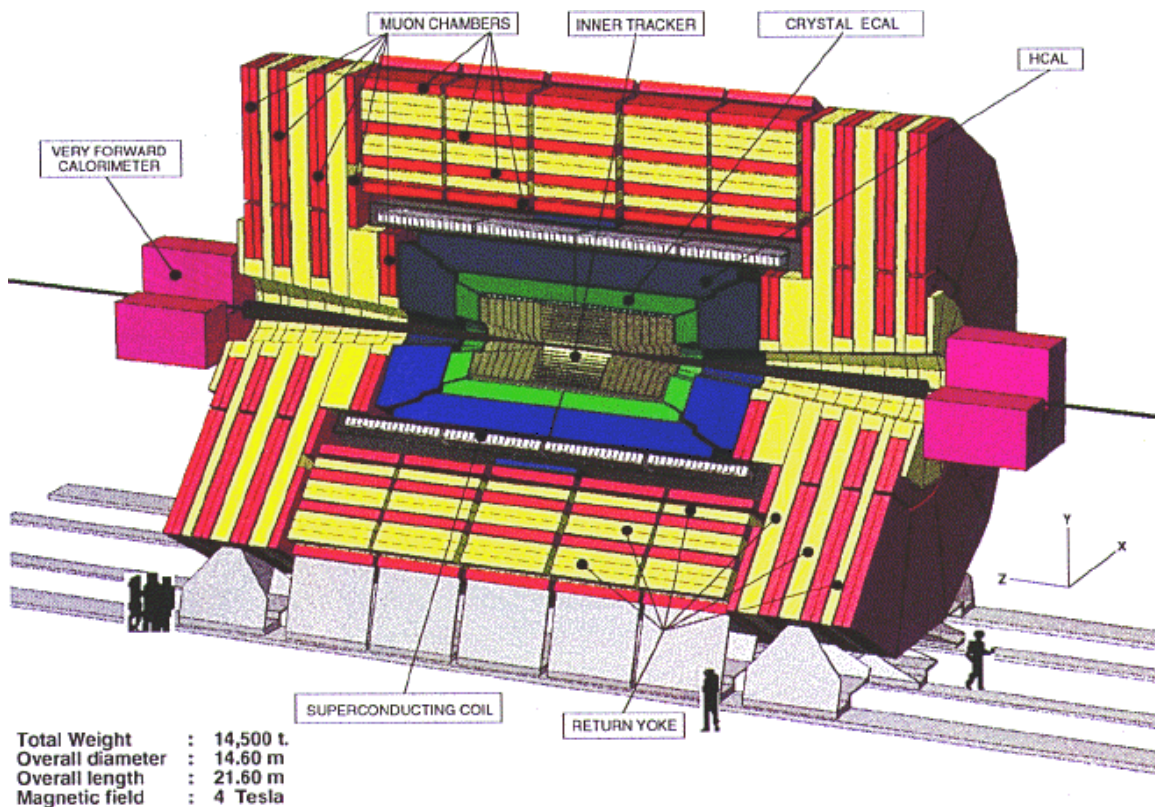
Figure I.7: Three dimensional view of the CMS Detector.
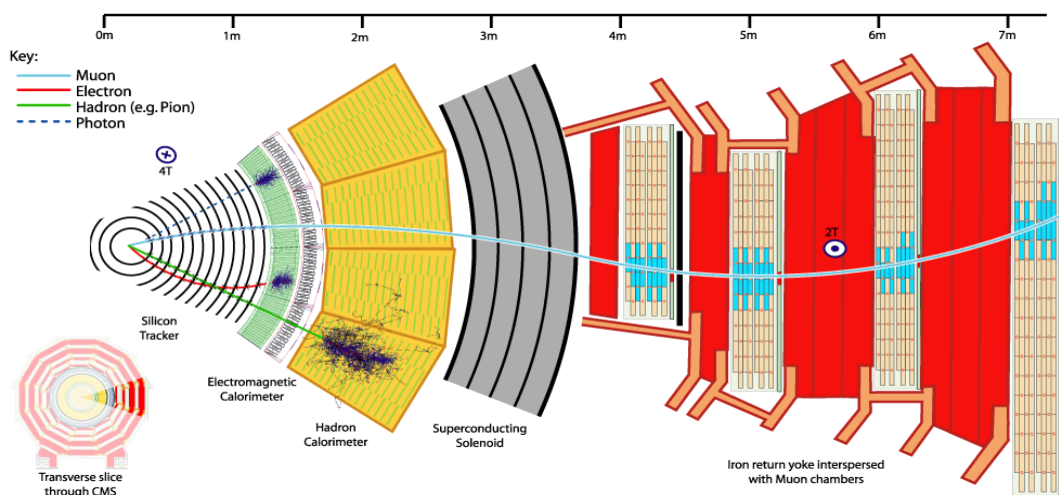
Figure I.8: Slice of CMS detector.

a) Magnet and Magnetic Field

The configuration and parameters of the magnetic field are very important. The momenta of the charged particles are measured according to the bending of their trajectories in the detector. A large bending power or a highly precise spatial resolution and alignment of the detector are necessary to obtain high momentum resolution [2].

The magnet of the CMS detector (see Figure I.9), which will be the largest magnet system in the world, is made of a long superconducting solenoid, the magnet yoke –barrel and endcap -, a vacuum tank and ancillaries. The superconducting coil system is composed of a solenoid of 13 m in length and 5.9 m in free inner diameter, and the ancillary subsystems. With this magnet, a magnetic field of 4 Tesla is created. The magnetic flux is generated by the superconducting coil and returned via a 1.5 m thick saturated iron yoke instrumentated with four muon chamber stations. The solenoidal type of magnetic field is chosen to obtain a compact design with strong magnetic field inside the coil [14]. The yoke is formed of a barrel and endcap yoke. The 13.2 m long barrel yoke is a 12 sided cylindrical structure. It is divided into five rings, each of which is made of three iron layers. The two endcap yokes are made from three independent disks which can be separated to give access to the forward muon stations. The two inner disks are 60 cm thick in order to withstand the attraction force, and the outer disk is 25 cm thick. The yoke diameter is 14 m across flats and the axial yoke length is 21.6 m including the endcaps. The magnet's total weight is about 12,000 tons. The stainless steel vacuum tank houses the superconducting coil [1, 2].

The favorable length to radius ratio of the solenoid allows efficient muon detection and measurement up to the rapidity of 2.4 without the need for forward toroids. Thus the muon spectrometer uses a single magnet, simplifying the detector design. The inner coil diameter is large enough to accommodate the tracker and the calorimeters. Since the magnet is the main element of the CMS in terms of size, weight, and structural rigidity, it is used as the principal structural element to support all other barrel detector components [1].
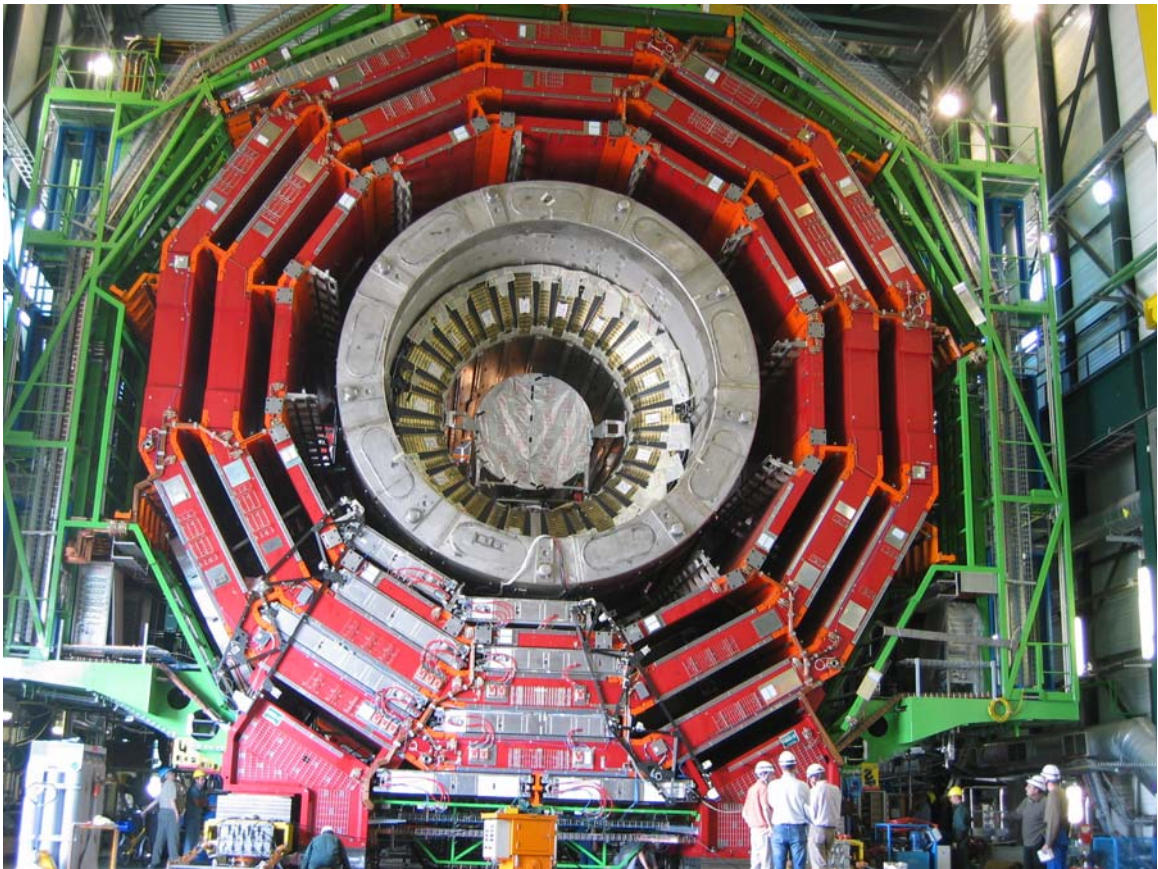
Figure I.9: Closing for the CMS magnet.

b) Muon System

The muon system has the task of identifying muons and, in association with the tracker, measuring their momenta. It is expected that muons will provide information for many physics processes. Muon identification is possible thanks to the existence of at least 10 interaction lengths (lambdas) of calorimeters before the first station and an additional 10 lambdas of iron yoke before the last station. The thick absorber material can only be traversed by muons and neutrinos. The bending of the charged tracks in the magnetic field is studied to obtain the momenta of the muons [2].
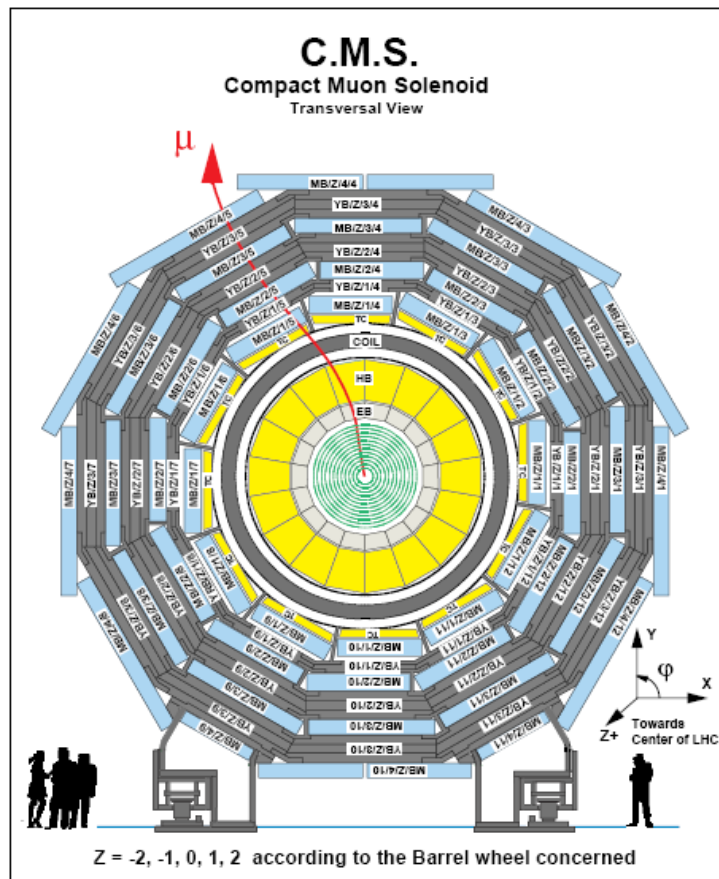
Figure I.10: Transverse view of the CMS detector.

The CMS muon system is designed to allow for the identification of muons and for the measurement of their transverse momentum online for triggering purposes. Reconstruction of muons and measurement of their momenta, and using these information for triggering purposes is important since muons have a crucial role for the discovery studies [15]. The performance of the muon trigger system is important to be able to reduce the high proton-proton interaction data rate to a few kHz.

The muon detectors are placed behind the calorimeters and the coil. They consist of four muon stations interleaved with the iron yoke plates. The detectors are placed as concentric cylinders around the beam line in the barrel region and as disks perpendicular to the beam line in the endcap region. Each station has multiple chambers, which provide many measurement points. Figure I.11 shows the schematic view of the moun system.

Figure I.11: The schematic view of the muon system.

In the CMS detector a muon sees four muon stations over most of its solid angle (see Figure I.10). Each of the four barrel stations (MS1 to MS4) consists of twelve

planes of aluminum drift tubes (DTs), arranged in twelve azimuthal sectors, such that there are no cracks pointing to the primary vertex. The endcap muon system also consists of four muon stations MF1 to MF4. Each station consists of sectors of Cathode Strip Chambers (CSCs) overlapping in azimuth to maintain full coverage. The two stations MF1A and MF1B have been added to ensure that all muon tracks transverse four stations at all rapidities, including the transition region between the barrel and the endcaps ($1 < |\eta| < 1.5$) [1, 2].

Resistive parallel plate chambers (RPCs), which are fast gaseous detectors, are put in both barrel and endcap regions. The DTs and CSCs are used for the measurement of the position and momenta of muons, whereas, the RPCs provide information for the Level 1 trigger.

Efficient muon detection is guaranteed up to $|\eta| = 2.4$ for $P_T > 4$ GeV. The acceptance of the Hadronic Endcap (HE) has been extended up to $|\eta| = 3$ to allow the insertion of a thicker conical iron structure. This cone significantly reduces the background rate in the four forward stations (MF1 to MF4). It can also support the endcap calorimeters without cutting into the azimuthal acceptance [1].

c) Tracker

The goal of the tracking system is to reconstruct the high P_T muons, isolated electrons, hadrons with high momentum resolution and with an efficiency of better than 98% over the rapidity range $|\eta| < 2.5$, and to identify the tracks coming from detached vertices which arise from b-quark decays.

The tracker system of the CMS detector is powerful and has the ability to fulfill the requirement of improved measurements [16].
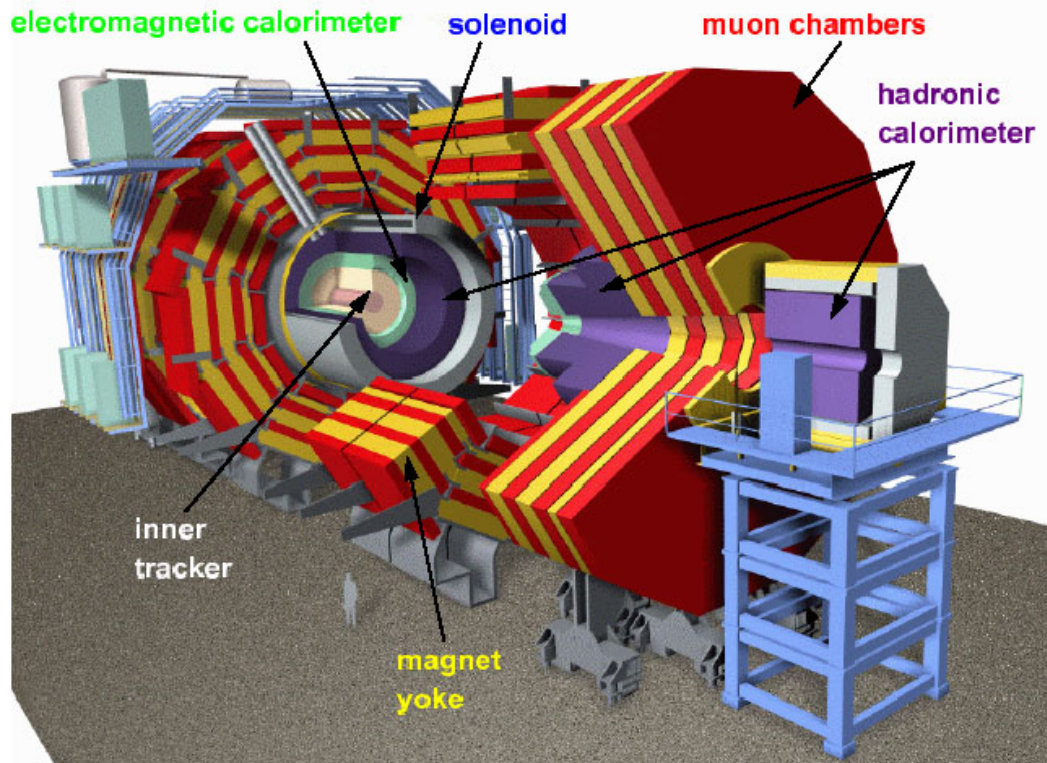
Figure I.12: Another three-dimensional view of CMS detector.

In the central rapidity region, the isolated tracks with high transverse momentum are reconstructed with a transverse momentum resolution better than $\Delta p_T / p_T \cong 15\ p_T$ % (p_T in TeV). When combined with the outer muon chamber system, the resolution of muon momentum measurements of muons with more than 100 GeV momentum becomes very good. Thanks to the high granularity of the CMS tracking system, the reconstruction efficiencies for charged hadrons with p_T above 10 GeV/c, muons and electrons are 95%, 98% and above 90% respectively [2].

Figure I.13: A picture of the tracker.

Silicon is used for the entire CMS tracker, which implements 25000 silicon strip sensors covering an area of 210 m^2. The interaction region is surrounded by the two barrel Silicon Pixel detectors at small radii from the beam line and by two endcap disks at radii from 6 to 15 cm. The silicon pixel detectors close to the interaction vertex are designed to give a 20 μm resolution in the transverse plane and a 100 μm resolution in the z direction. The solid-state pixel and microstrip detectors and gas microstrip detectors will provide the granularity and precision for pattern recognition at high luminosities [1].
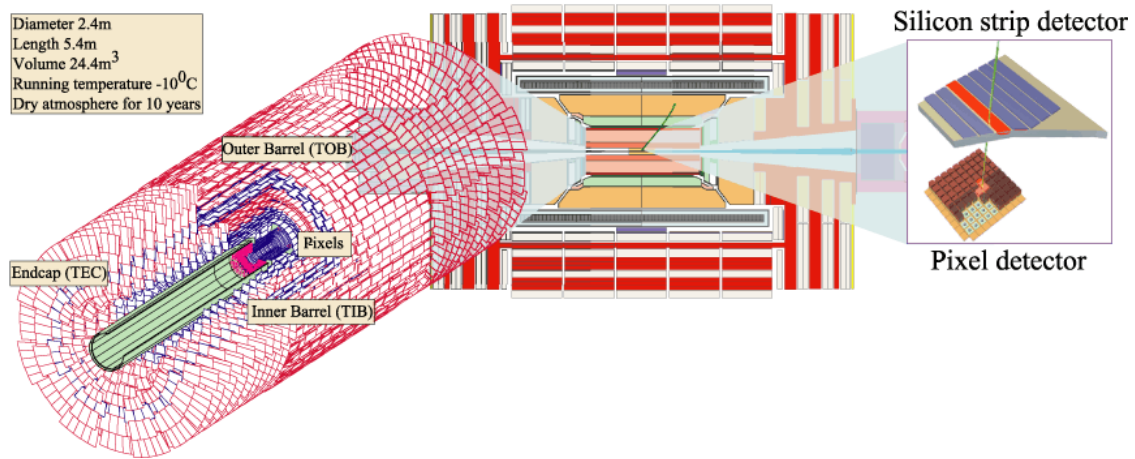
Figure I.14: The schematic view of the CMS tracker.

d) Calorimetry

Calorimeters will stop electrons, photons and hadrons and measure their energies. The electromagnetic calorimeter (ECAL) [1, 2] makes high precision measurements of the energies of electrons and photons which interact electromagnetically, whereas, particles interacting via strong interaction, hadrons, will be stopped by the second layer of calorimeter, which is called the hadronic calorimeter (HCAL) [1, 2]. Neutrinos cannot be detected either by ECAL, or by HCAL, but their presence will be seen as an energy imbalance in the collisions.

The electromagnetic calorimeter

The performance of the electromagnetic calorimeter will be important especially for the Higgs boson search. The decay of the Higgs boson with a mass in the range of 100-140 GeV into two photons is the channel that requires the good performance of the ECAL. Also, the production of electrons and positrons from the decay of a Higgs boson

to two Z's or W's for 140 GeV < m_H < 700 GeV needs strict performance of ECAL. To obtain good results, it is important to have very good energy resolution and fast response from the crystals. All the terms making up the energy resolution have to be kept small and should be roughly equal at photon energies corresponding to half the Higgs mass. The ECAL should also have a good two shower separation capability and a large rapidity coverage.

Over 80,000 high resolution $PbWO_4$ (lead tungstate) crystals (see Figure I.15) will be used in the design of the CMS electromagnetic calorimeter. $PbWO_4$ is radiation hard. Since the detector is in a high radiation area, the material it is made of should not be affected by radiation. Also, since $PbWO_4$ crystals have a high density, a small Moliere radius (allowing narrow showers), and a short radiation length, the scintillation process is fast (20 ns).

The ECAL is composed of barrel (η < 1.48) and end-caps (η < 3.0). Due to the strong magnetic field, it will not be possible to use photomultipliers. Instead, silicon avalanche photodiodes will be used in the barrel region and radiation-hard vacuum photodiodes will be used in the end-caps.

After being captured by a photodetector, the signal will be amplified and digitized. Figure I.15 shows the ECAL read-out system.
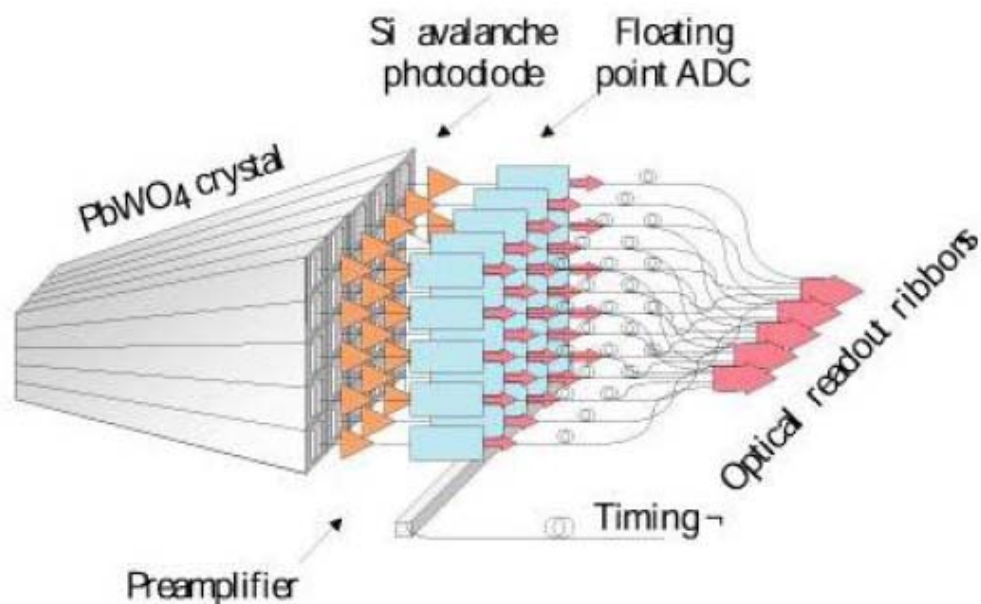
Figure I.15: The schematic view of the ECAL read-out system.

2) The Hadronic Calorimeter (HCAL)

The hadron calorimeter (HCAL), which is the outhermost detector inside the magnet, surrounds the ECAL (see Figure I.12). It acts together with the ECAL, tracker and muon system to measure the energies and directions of particle jets, and to provide hermetic coverage for measuring missing transverse energy. These are essential for the identification and measurement of quarks, gluons, and neutrinos.

The missing transverse energy is crucial for the detection of new particles, such as supersymmetric partners of quarks and gluons, and a good energy resolution can be achieved with a wide hermeticity coverage. For some reactions, a coverage up to $|\mu| = 5$ is needed. HCAL measurements will be important especially for the search of the high mass Higgs boson and of supersymmetric particles. Aside hermeticity and transverse granularity, adequate depth is also important. It is needed to contain high-energy jets and

to eliminate the hadrons in the jets in order to obtain a better muon and trigger measurement. A good transverse granularity is necessary to measure the jet directions and to separate two-jet combinations. The performance of the HCAL is not constrained too much by the physics processes. The jet energy resolution is adjusted by the jet-finding algorithm, the fragmentation process, the magnetic field and the energy pile-up when running at high luminosity.
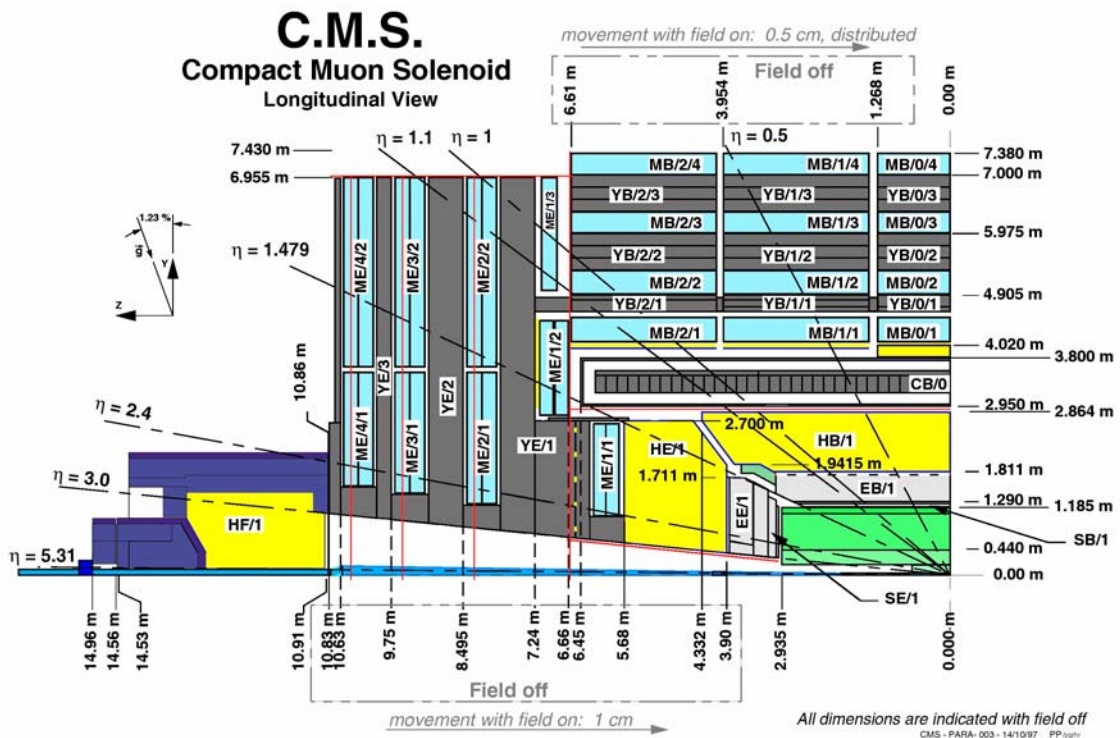
Figure I.16: The CMS HCAL calorimeter.

The HCAL has three components: the Hadronic Barrel (HB) Calorimeter, the Hadronic Endcap (HE) Calorimeter and the Hadronic Forward (HF) Calorimeter [1]. HB and HE are sampling calorimeters with 50 mm thick brass absorber plates with 4 mm thick scintillator sheets between them. They sit inside the 4 Tesla field of the CMS

solenoid, and cover the pseudorapidity range of |η| < 3.0. The HF is made of radiation-hard quartz fibers inserted between steel absorber plates. The HF is put around the beam-pipe outside the muon system and extends the pseudorapidity coverage up to |η| < 5.3.

The light from the fibers is carried to read-out boxes via clear optical waveguide fibers. For the endcap and barrel detectors, hybrid photodiodes (HPDs), for the forward detectors, photomultiplier tubes (PMTs) will be used as photosensors.

The achievable energy resolutions are:

$\frac{\sigma_E}{E} = \frac{65\%}{\sqrt{E}} + 5\%$ for the HB, $\frac{\sigma_E}{E} = \frac{85\%}{\sqrt{E}} + 5\%$ for the HE, and $\frac{\sigma_E}{E} = \frac{100\%}{\sqrt{E}} + 5\%$ for the

HF, where E is measured in GeV.

e) Trigger and Data Acquisition (DAQ)

Due to high luminosity, there will be a large amount of information coming from the detectors of the LHC. The proton beams will cross each other 40,000,000 times every second. It is estimated that initially, the event size in the CMS experiment will be 1 MB. Performing an online analysis and storing all of these data will be very difficult. Since not all the events are physically meaningful, a reduction of the data should be done so that the analysis will be possible. In this way interesting events will be kept and part of the unwanted background will be rejected.

In the CMS experiment, the data reduction is done in several steps, called levels. In the Level 1 trigger (LV1), the data is received at the LHC beam crossing frequency of 40 MHz and reduced to 100 kHz. Because of the low luminosity, at the beginning of the

LHC, this valued will be 50 kHz. In this level, the trigger selection is made using trigger candidates reconstructed based on the information from the muon system and the calorimeter and by applying threshold cuts on them [17].

In the High Level Trigger (HLT), selections are made by the software running on a large farm of commercial computers. The LV1 output rate is reduced with dedicated fast algorithms. The measurements on trigger candidates from LV1 (jets, leptons, photons, and missing transverse energy) will be defined by higher levels such as Level-2, Level-2.5, and Level-3. At the end, these raw objects can be used for physics channel identification. The type and number of trigger levels are flexible in the HLT and can be adjusted according to the running conditions [18].
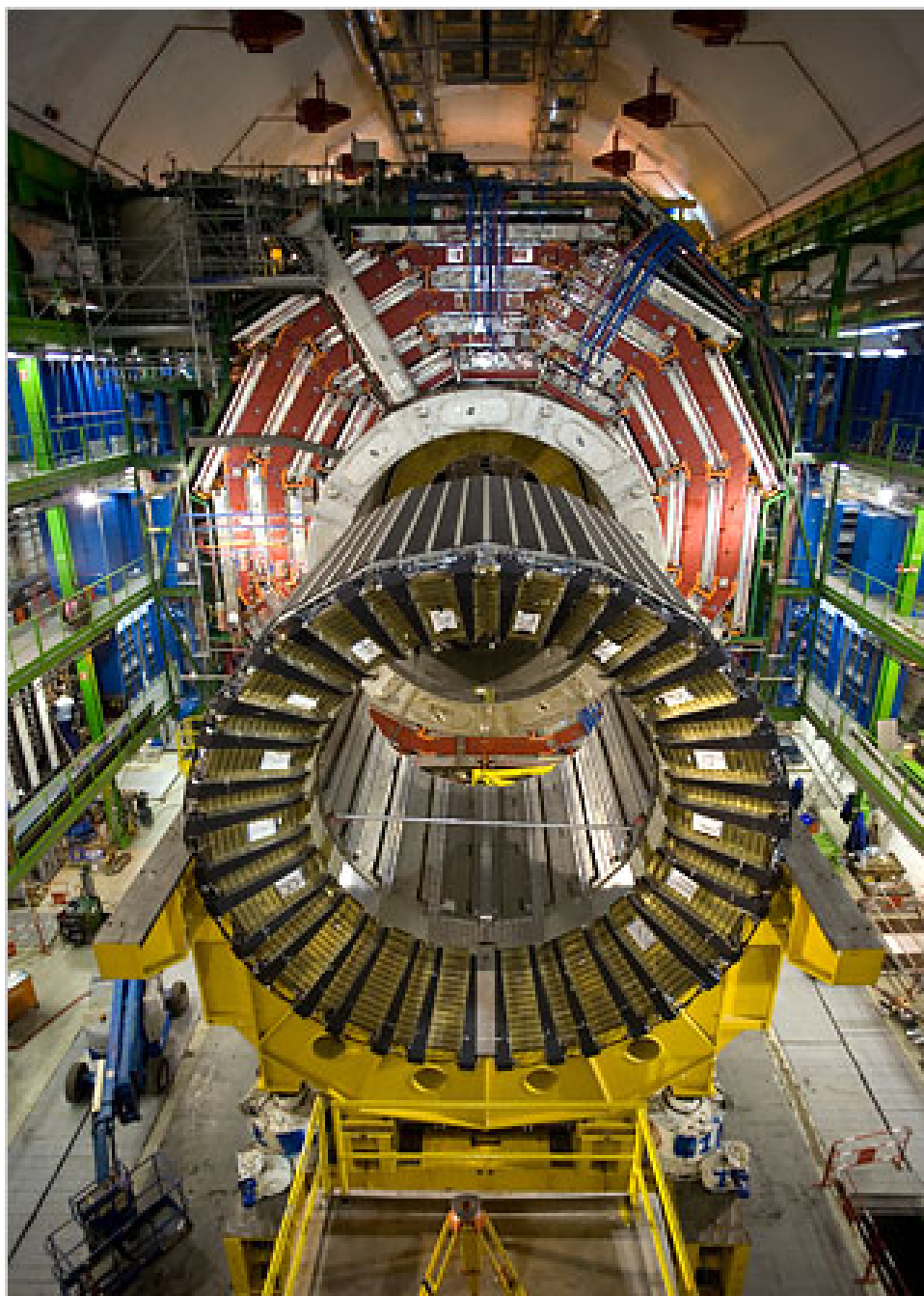
Figure I.17: A photograph from the construction site of the CMS detector.

PART A: R&D STUDIES ON THE HADRONIC CALORIMETER OF THE CMS

EXPERIMENT

CHAPTER I

RADIATION DAMAGE AND LIGHT TRANSMISSION STUDIES

DONE ON AIR CORE LIGHT GUIDES

1.1 Introduction

Air core light guides are routinely used in a wide range of high energy physics experiments to carry the photons to photomultiplier tubes (PMT). There is a loss of light during the transmission which depends on the length, shape, and the reflecting film of the air core light guide. On the other hand, their use helps to smear the photocathode nonuniformities of the PMTs [19].

Figure 1.1: Light guides.

The HF calorimeter of the CMS detector is composed of steel absorber plates with embedded quartz fibers and an optical read-out system that is composed of PMTs and

light guides (see Figure 1.1). The high radiation and long term exposure of detector materials in addition to budget issues necessitated the use of the light guides. Due to both the HF location and the operating conditions, light guides will be placed between the fiber bundles and the PMTs (Figure 1.2). The air core light guides used in the HF are hollow aluminum tubes with a 25 mm diameter and 43 cm length, except at three low η towers where tapered light guides are used (see section 1.4 for detailed information).

The distal ends of the quartz fibers extend beyond the steel where they are collected into bundles of a size that can fit into the ends of the light guides. The insides of the light guides are lined with a highly reflective film. The reflective films used in the air core light guides are multilayered such that the material thicknesses are scaled in order to produce constructive interference effects on different incident light wavelengths and angles.
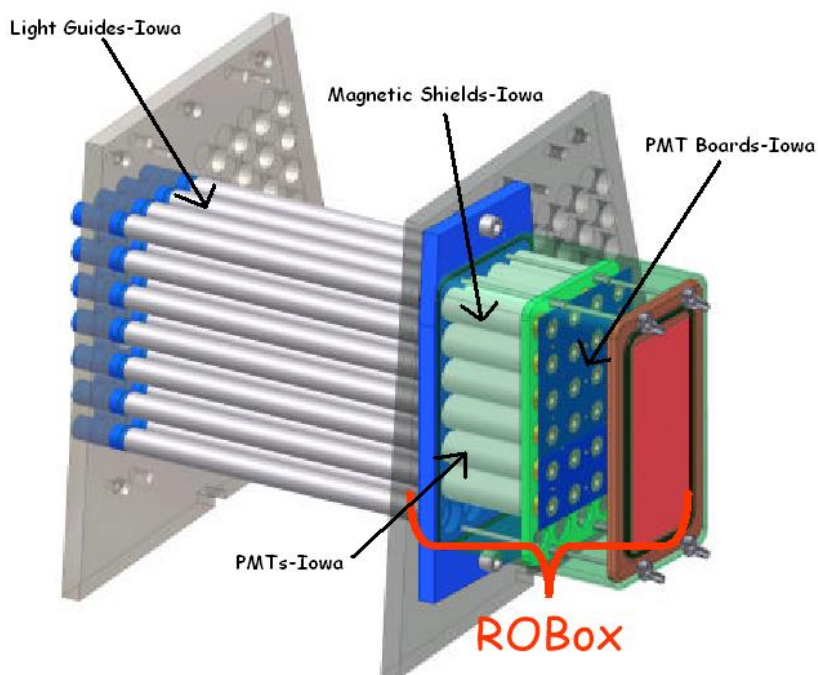
Figure 1.2: The CMS HF calorimeter Read-Out Box (ROBOX) design.

It is important to study the light transmission efficiency, as well as radiation hardness of the light guides to find out the best choice of shape and material for a given experiment. Especially important in future collider experiments (such as the LHC experiments), which are going to run at unprecedented energy levels for years, are the issues of radiation hardness and light transmission efficiency of the reflective films.

1.2 Experimental Setup

The light guide tests were performed at the University of Iowa CMS laboratories [20]. As shown in Figure 1.3, two dark boxes were used in the setup. The first box contained a 337 nm nitrogen laser (LSI, model VSL-337ND) light source with a scintillator block in front. The laser had a wavelength shifter, a blue filter, and a neutral density (ND) filter to adjust the light intensity. The contribution of the laser pulse to individual measurements was negligible since the pulse was very sharp. The light coming out of the scintillator block had a wavelength range of 390-500 nm with a peak light intensity corresponding to the maximum PMT sensitivity at 420 nm. The laser stability was monitored with a PIN diode.

The light from the laser was then carried to the other dark box which contains the air core light guides by a 600 μm core diameter quartz fiber. Light guides were attached to a computer controlled X-Y scanner which scanned the light through the surface of the light guide. The scanner could move along the x and y directions with a 6.35 μm step size. The transmitted light intensity was measured with a Hamamatsu R7525HA PMT [21]. The PMT and the light guide were coupled with a black tube holder with a distance between them of 5 mm. The horizontal position for the dynode was defined to be the x-axis.

For all of the light guides the light transmission was measured as a function of x and y position. With the help of the X-Y scanner, the light guide and the PMT were moved so that the end of the fiber sent light down the tube from left to right and from top to bottom with 1.4 mm step sizes.
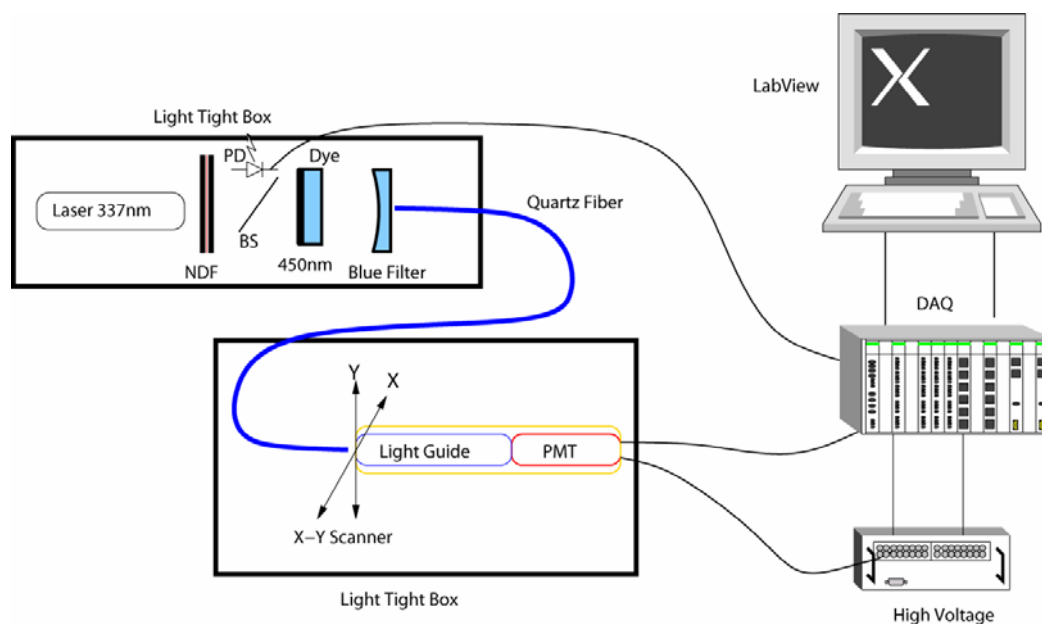
Figure 1.3: Light guide test setup.

A control tube was run before and after each light guide to ensure consistency in the results. Each time the tube was attached to the X-Y scanner, the reflector seams inside the tube, as well as the PMT base label, were always directed straight up. This ensured that the PMT dynodes were aligned relative to the seam of the reflecting material in the same way for all measurements. The light guide was clamped into the scanner so that the end of the tube came to the tip of the fiber, but did not actually touch the fiber. The PMT

anode signal was integrated by an ADC (LeCroy 2249A) CAMAC-LabView data acquisition (DAQ) system to determine the total charge on the PMT from the light pulse.

1.3 Radiation Damage and Light Transmission Tests

The effects of radiation on the light transmission efficiency of an air core light guide with different reflective materials were tested at the University of Iowa.

Here we have the results of the radiation damage and light transmission studies done on air core light guides with three different reflective films. According to previous studies, reflective films show some structural damages [22], and degradation of reflectivity [23, 24] under irradiation. Aluminum tubes of 2.5 cm in diameter and 43 cm in length were used as light guides, and the insides of the tubes were lined with a reflecting film. The films used in this study were; a 25 μm thick aluminized Mylar (Type-1 AM), a new and thicker aluminized Mylar (Type-2 AM) which has extra Nb_2O_5 and SiO_2 layers, and a new highly reflecting film (3M^{TM} Radiant Mirror Film) often referred to as High Efficiency Mirror (HEM). Thicker Type-2 aluminized Mylar was developed by the Fraunhofer Institute for Electron Beam and Plasma Technology for the purpose of maximizing the reflectivity at higher angles of incident light [25]. The HEM consists of hundreds of layers of a polymer with non-isotropic indices of refraction in thicknesses chosen to produce optical interference that results in an exceptionally high reflectivity [26].

1.3.1 Radiation Damage Studies

Three air core light guides prepared with each reflecting film were exposed to 10 Mrad radiation using the 9.5 kCurie ^{137}Cs source at the University of Iowa Radiation Research Center. Measurements were done at varying irradiation levels from 2 to 10

Mrad. These nine air core light guides were tested before and after irradiation at the University of Iowa PMT test station.

Figure 1.4 shows the summary of the results of the radiation damage tests [19]. Since we have irradiated three light guides from each reflecting film, the average of the corresponding groups are shown. The x-axis represents the position of the fiber along the light guide diameter in arbitrary units. The y-axis shows the ratio of the total collected charge by the PMT before and after the irradiation. Since the light guides have no preferred orientation, the results for the x and y positions with respect to the PMT dynode are averaged. The ratios for the signal before and after the radiation are consistent within a 3% variation for the Type-2 AM and the HEM, showing that they are almost not affected by the 10 Mrad radiation. The Type-1 AM shows some degradation up to 14% ± 2%, after the irradiation. The results are in agreement in previous reflective material studies [27].

The results for the HEM and Al Mylar reflectors separately are shown in Figure 1.5 and 1.6 [28]. The y-axis demonstrates the ratios of the PMT outputs before and after irradiation. Different shapes represent different irradiation levels: ● – 2 Mrad, □ – 4 Mrad, Δ - 6 Mrad, * - 8 Mrad, ○ – 10 Mrad.
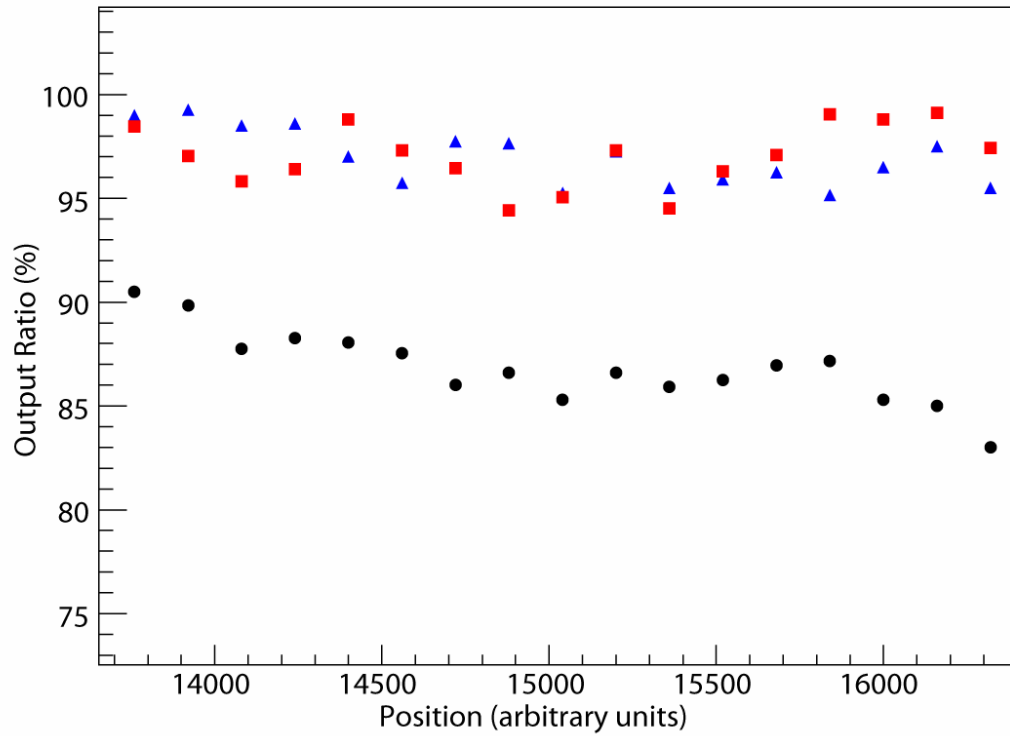
Figure 1.4: Light transmission ratios as a function of position along a diameter of the light guides, with three different reflecting films, after the irradiation. The outputs are normalized with respect to the values before the irradiation. The circles, squares, and triangles denote Type1 AM, Type 2 AM, and the HEM, respectively.
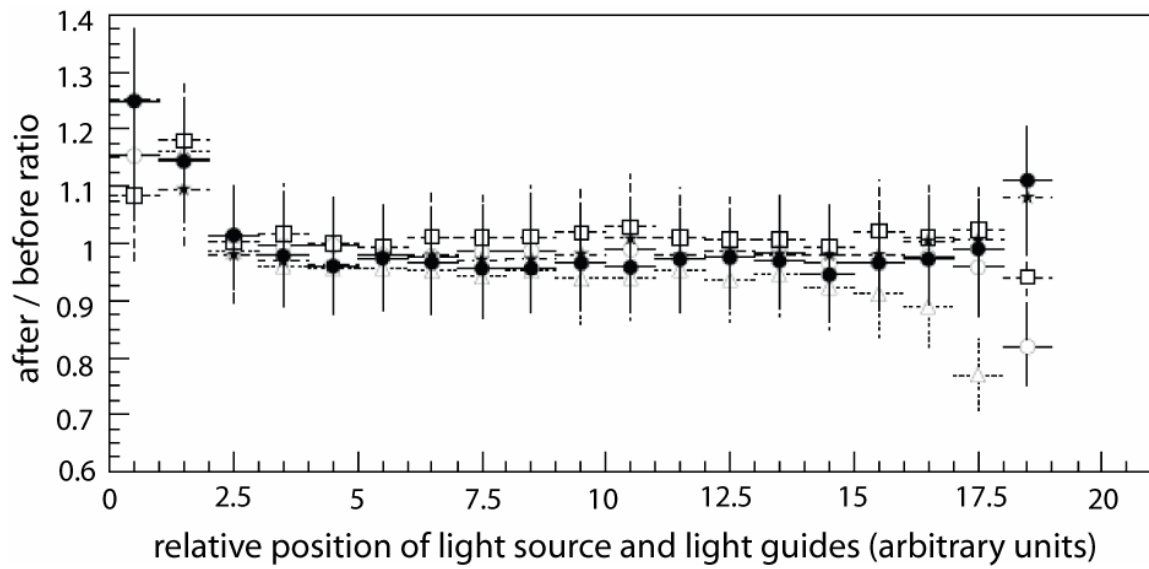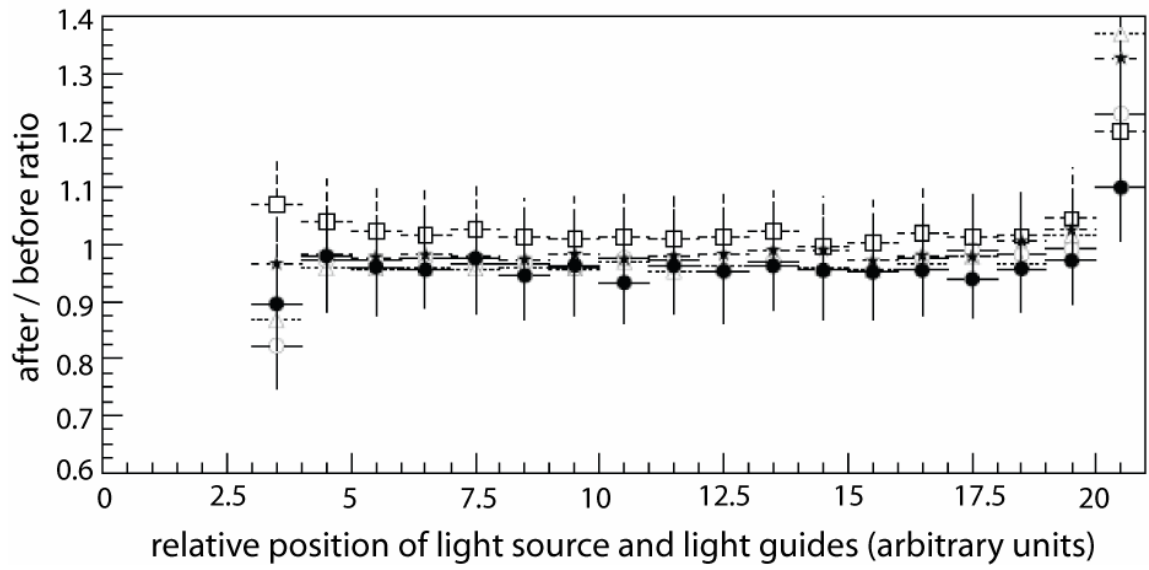
Figure 1.5: The ratios between PMT output after and before irradiation for HEM reflector.
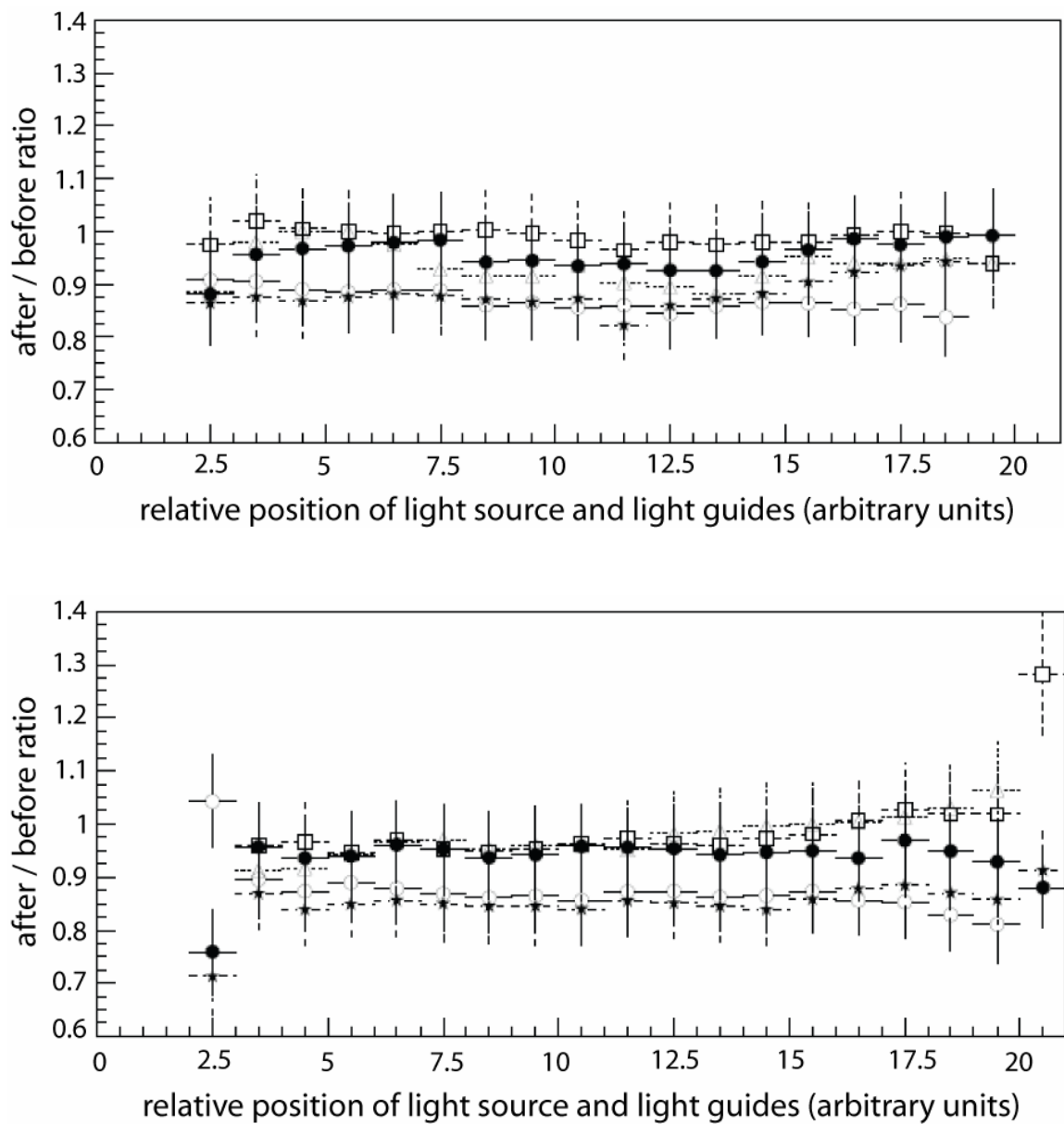
Figure 1.6: The ratios between PMT output after and before irradiation for Al Mylar reflector.

1.3.2 Light Transmission Efficiency Studies

The light transmission with the reflective films through the air-core light guides was tested with different light sources; a 450 nm Blue LED, a 380 nm UV LED and a mercury light bulb. We tested three air core light guides prepared with each reflective film. The test setup was kept the same as the radiation tests described above except for the light source. In case of the mercury light bulb, which was a DC light source, a picoammeter (Keithley), rather than an ADC, was used to measure the PMT output.

The top part of Figure 1.7 shows the data taken with the blue LED as the light source. When the incident light had a wavelength of 450 nm, the Type-2 AM transmits light about 8% better than the HEM, while the Type-1 AM transmits only as much as 50% of the Type-2 AM.

The middle part of Figure 1.7 shows the results with the mercury light bulb. The mercury light spectrum has photons from different wavelength regions (see Figure 1.8). The photons that can be detected by the Hamamatsu R7525HA PMT are in the 300-650 nm wavelength regions.

The integration of different light intensities and wavelengths from the mercury source gives comparable transmittance values for all three reflective films. However the Type-2 AM is still slightly more efficient than the others.

The bottom part of Figure 1.7 shows the results with the 380 nm UV LED as the light source [19]. In contrast to the above measurements, the Type-1 AM performs better than the other reflective films in the UV range. The Type-2 AM transmits light at 70 % of the Type-1 AM value. The HEM loses its transmission ability drastically in the UV range and transmits light at around 30 % of Type-1 AM.
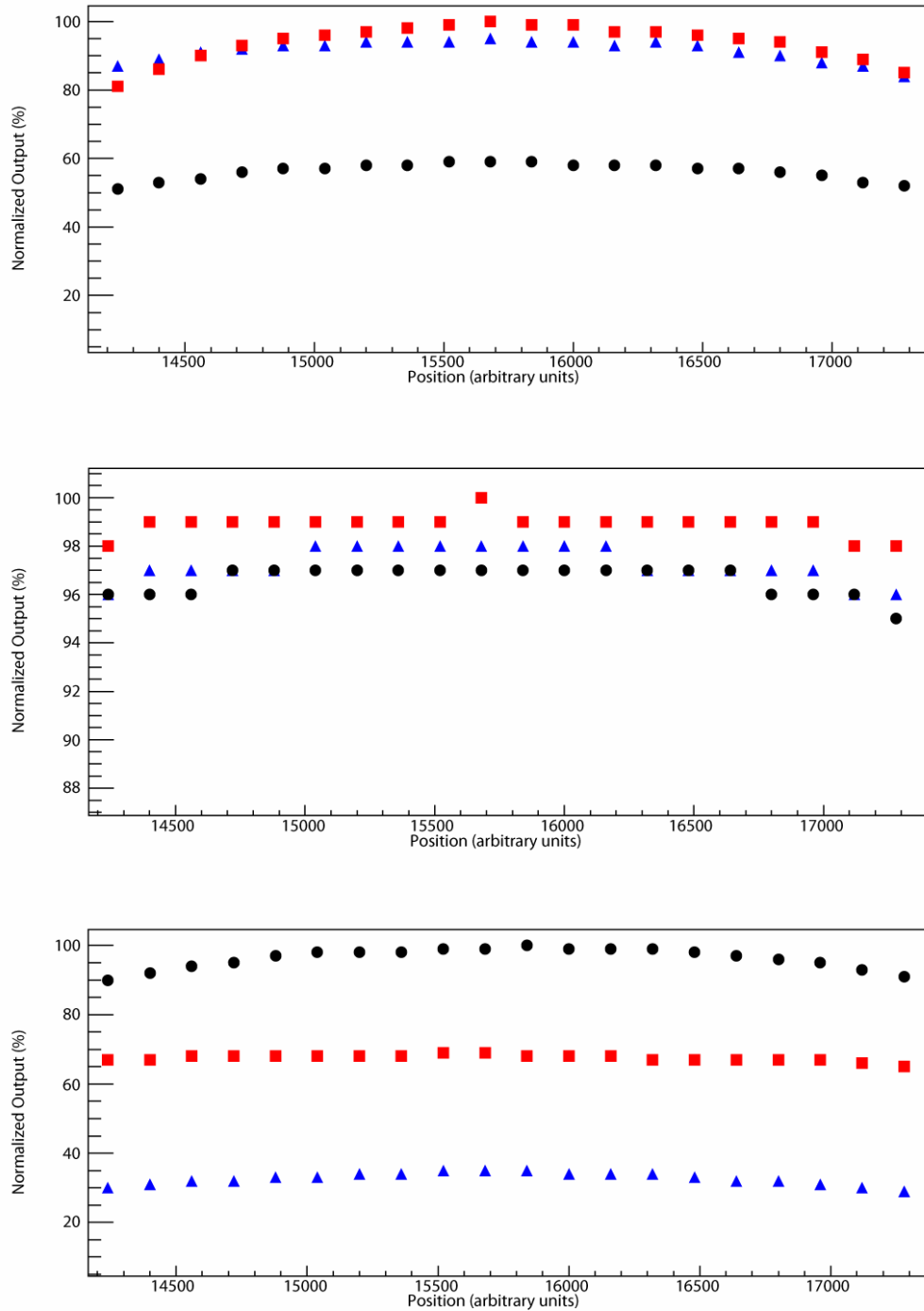
Figure 1.7: Normalized light transmission ratios as a function of position along a diameter of the light guides with three different reflecting films and the light sources: 450 nm blue LED (top), mercury light bulb (middle), 380 nm UV LED (bottom). The circles, squares, and triangles denote the Type1 AM, the Type 2 AM, and the HEM, respectively.
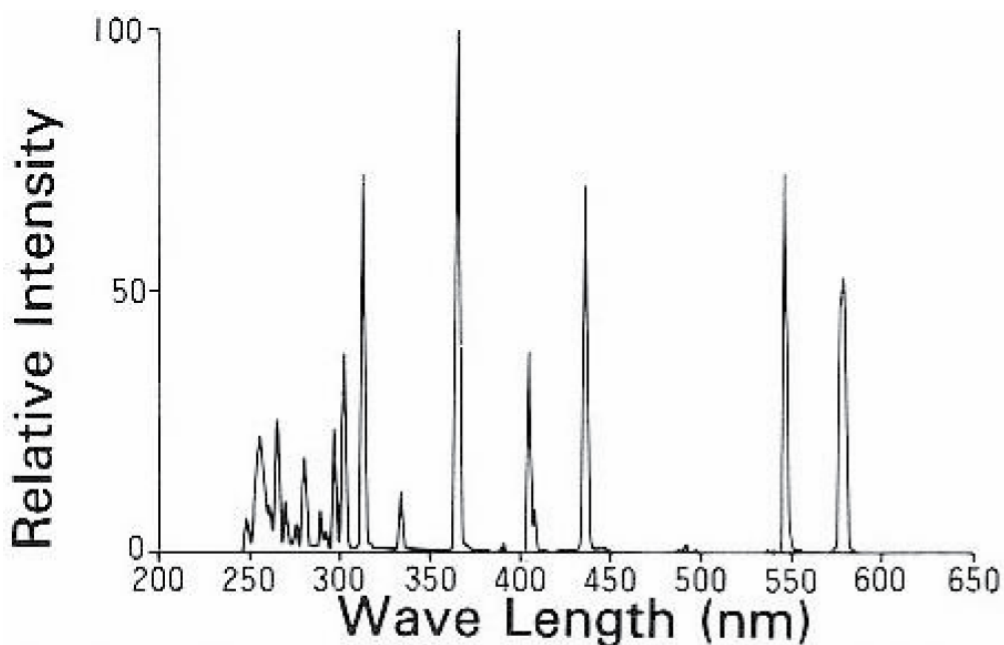
Figure 1.8: The emission spectrum of the mercury light bulb.

1.4 Surface Uniformity Tests

The variation of the output sensitivity of the PMT with respect to the position of the light spot on the PMT cathode is called the X-Y uniformity. Two different light guide shapes were considered in this study. The first one was a cylindrically shaped aluminum tube with a 43 cm length and a 25 mm diameter. The second type was an aluminum tapered shape with the same length but with two different end diameters, 25 mm and 26 mm (see Figure 1.9). These two types are used at different towers of the HF calorimeter depending on the fiber bundles.
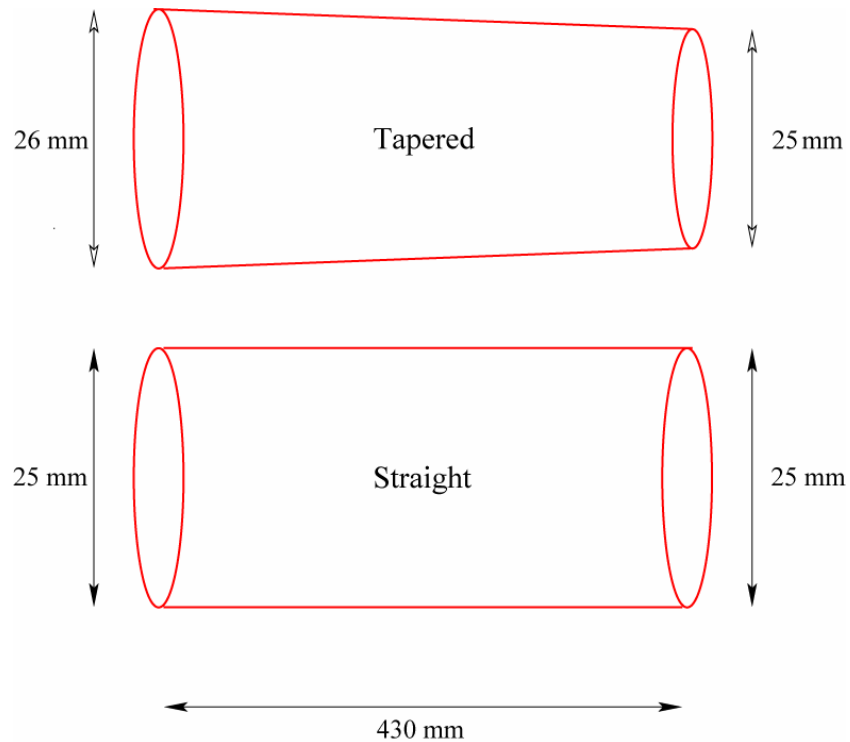
Figure 1.9: The two light guide shapes: Tapered at the top and straight at the bottom.

We studied the X-Y uniformity of the PMT for four different cases [29]:

a) Without a light guide

b) With a tapered light guide, and a HEM reflective material

c) With a straight light guide, and a HEM reflective material

d) With a straight light guide, and an AM reflective material

The X-Y uniformity without a light guide (configuration a) is shown in Figure 1.10. The data were taken at every 1.27 mm. The top plot shows the case when the PMT cathode surface was scanned along the x-direction with a fixed y-coordinate (at the center) of the PMT surface. The lower plot shows the case when the scanning was

performed along the y-axis with a fixed x-coordinate (at the center) of the PMT surface. The measured X-Y uniformity conforms to the manufacturer's specifications.

The X-Y PMT uniformities for the other cases (b, c and d) are shown in Figure 1.11. For the HEM case, the PMT response uniformity improves and reaches a plateau as the light source moves away from the edges of the photomultiplier tube. This is, in fact, a result of multiple reflections of the photons in the light guide. The points near the left/right and top/bottom edges of the PMT surface are relatively lower than the plateau due to the loss of the photons that strike the insensitive area of the PMT front window. We will call this the 'edge effect'.

In order to compare the effect of the light guide geometry, the data from configurations (b), and (c) were used. The ratios of PMT responses were calculated and plotted in Figure 1.12. For both the x and y directional scans, the ratios are level at around unity. Therefore we conclude that there is no superiority of the straight light guide over the tapered one. The ratio plots are distorted near the edges of the PMT front window due to the 'edge effect' discussed earlier.

Finally, to understand the influence of the reflecting material on the X-Y uniformity, the straight light guide was used. We used the data set (c), and (d) to calculate the response ratios. As seen in the lower two plots of Figure 1.12, the use of the AM material as the reflecting material reduces the light intensity by a factor of two (2.2 ± 1.2) with respect to the HEM material.
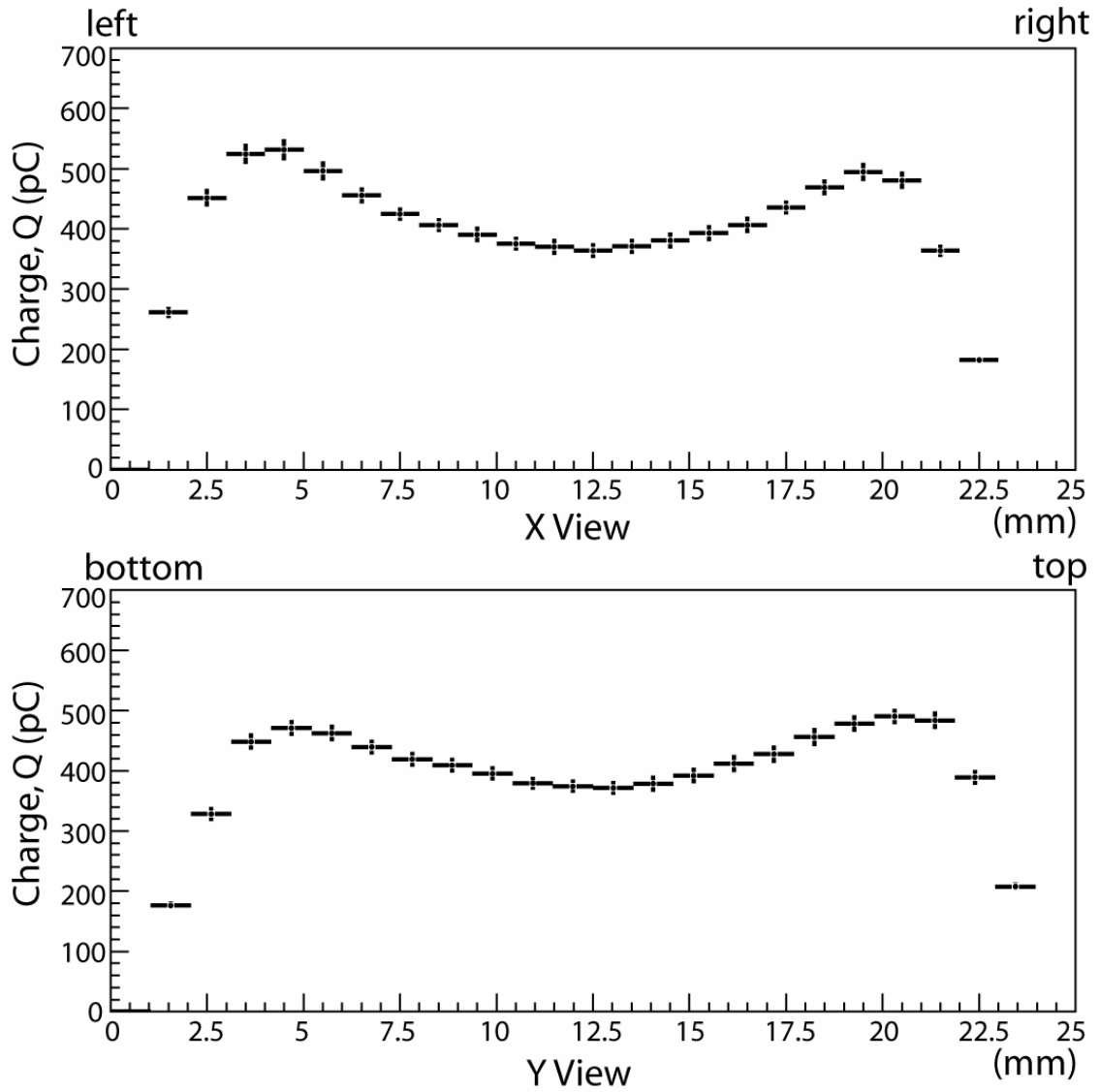
Figure 1.10: PMT x-y uniformity without a light guide. The spacing between the points is 1.27 mm.
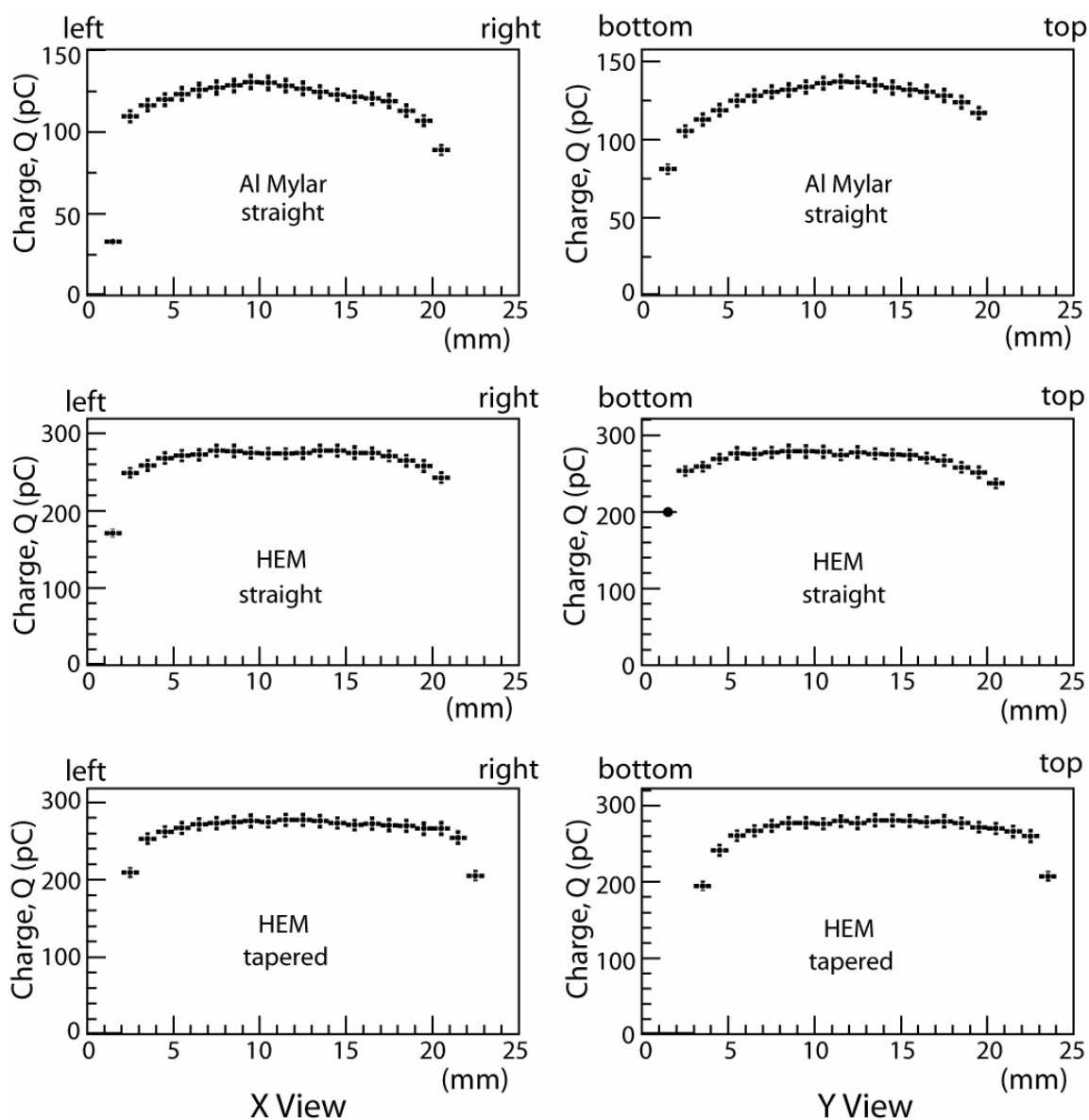
Figure 1.11: The PMT x-y uniformity with different light guide and reflecting material configurations.
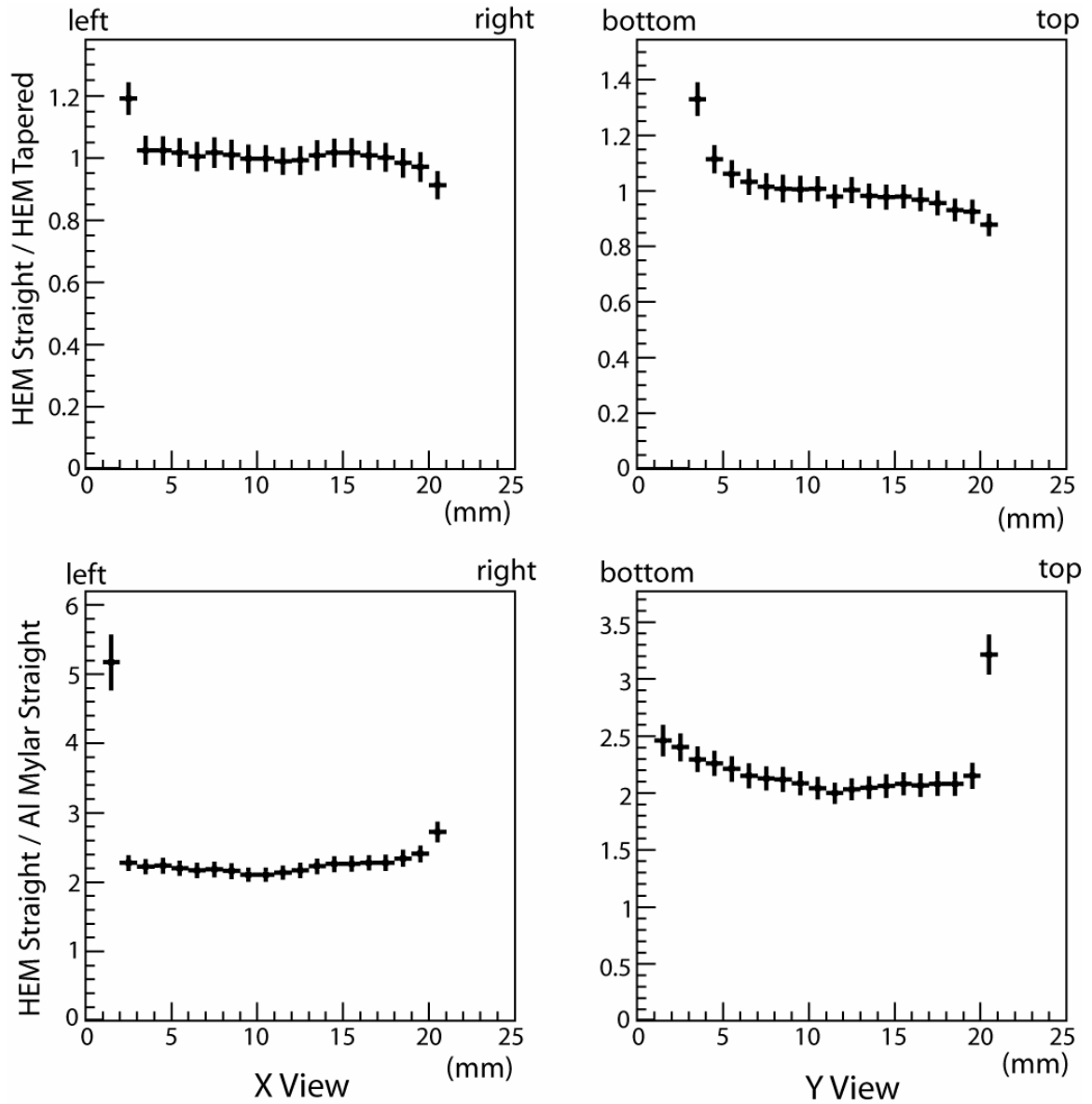
Figure 1.12: Ratios of PMT responses with different light guide and reflective material configurations.

<u>1.5 Reflectivity Tests</u>

The reflectivity of three different air-core light guide reflective materials was tested at the University of Iowa CMS Laboratories.

The reflective materials investigated were aluminized Mylar, high efficiency mirror (HEM), and German Mylar. We prepared three air core light guides from each material. The reflectivity ratios of these light guides were tested by using three different light sources: A blue LED at 450 nm wavelength, a UV-LED at 380 nm and a mercury lamp. All tests were done with the Hamamatsu R7525 PMT with a 10^4 anode gain.
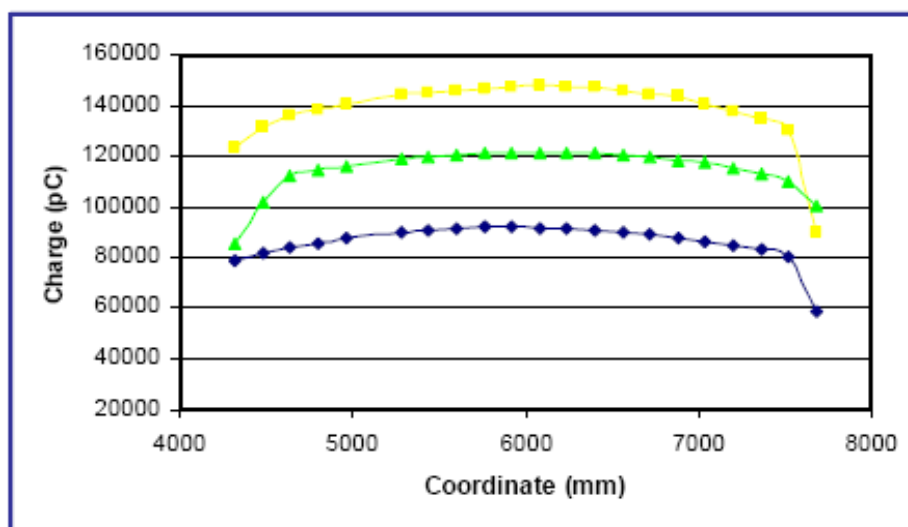
Figure 1.13: The results of the tests taken with the mercury lamp. Green triangle - German Mylar, yellow square -HEM, blue diamond-Al Mylar.

The tests showed that the German Mylar and HEM are better reflective materials than the Al-Mylar when the blue LED and mercury lamp are use as the light sources. However, at shorter wavelengths, the reflectivity of the Al-Mylar becomes more efficient than German Mylar and HEM. German Mylar and HEM are produced so that they have

low sensitivity in the UV region. These results are summarized in the Figures 1.13, 1.14 and 1.15, where the y-axis shows the collected charge and x-axis are the coordinates on the surface of the PMT. Towards the ends of the PMT, the collected charge decreases due to edge effect.
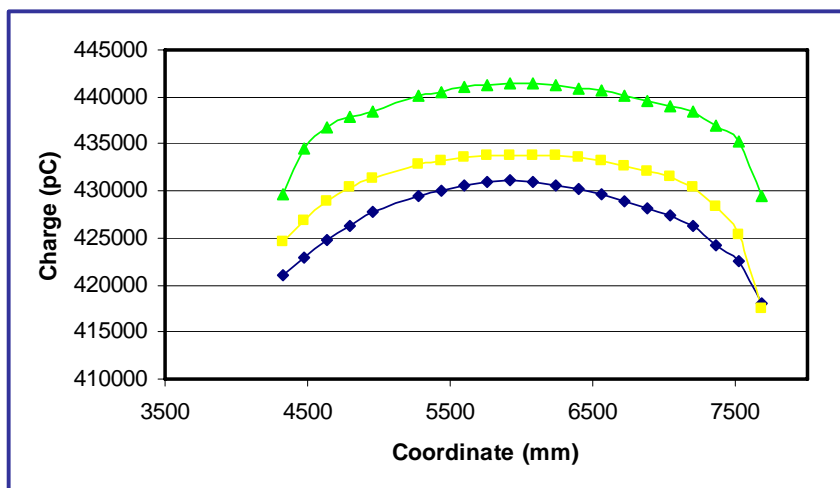
Figure 1.14: The results of the tests taken with the blue LED. Green triangle - German Mylar, yellow square -HEM, blue diamond-Al Mylar.
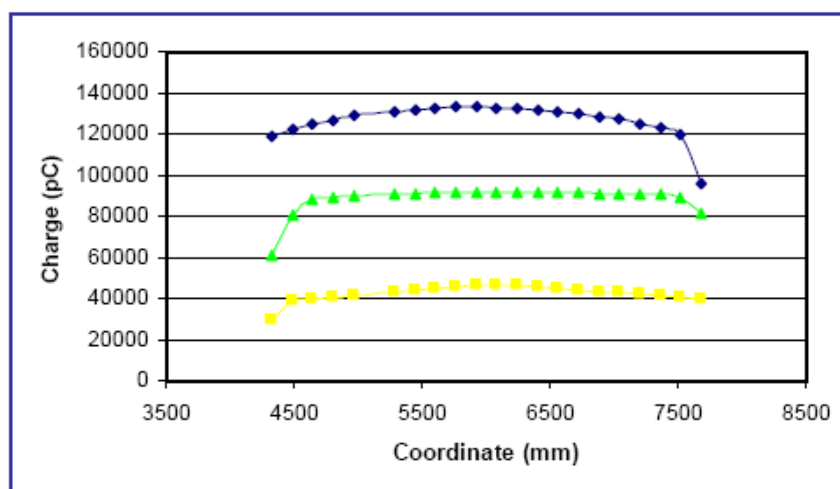
Figure 1.15: The results of the tests taken with the UV LED. Blue diamond - Al Mylar, green triangle - German Mylar, yellow square - HEM.

1.6 Simulations

We also performed simulations of light guides to compare the light transmission efficiencies of different shapes (tapered and straight) and of different wavelengths.

We simulated a 43 cm long aluminum light guide of 25 mm diameter with LITRANI, GEANT4 and ROOT based software. We tested the effect of tapering the light guide to 26 mm on one side. Photons were emitted from a fiber located at one end of the light guide with the fiber opening set to 60 degrees. The photons that reach the other end of the light guide were counted using a PMT. We scanned the diameter of the light guide with a 1 mm step size. 100,000 photons were sent at every run. Two different wavelengths, 337 nm and 450 nm, were selected for simulations imitating the nitrogen laser and blue LED, respectively. The ratio of photons detected at the PMT to the number of photons directed into the light guide is defined as the efficiency.

Simulation results are in agreement with bench tests. It is seen in Figure 1.16 that tapered and straight geometries yield almost the same efficiency. Figure 1.16 shows the light transmission efficiencies of the straight and tapered light guides. The peak of the efficiency curve, which is at around 40%, is comparable to the bench test efficiency, which is around 50%. There is a small difference that can be explained with the fact that the reflective properties of the materials used during the bench tests and the simulations were not identical. In the simulations the real part of the refraction index for the aluminum is used (see Figure 1.18).
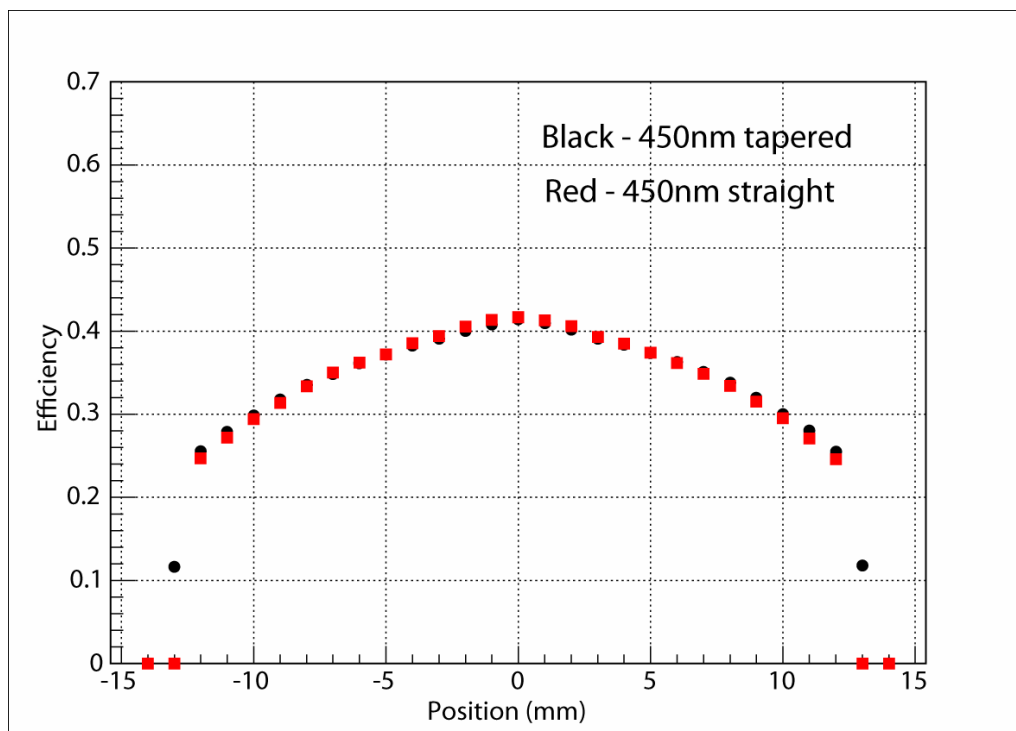
Figure 1.16: Light transmission efficiencies of the straight (red) and tapered (black) light guides.

Figure 1.17 shows the efficiencies of a tapered light guide for a 337 nm and 450 nm wavelength. Again, the efficiencies are very close to each other, especially at the center of the PMT. Going towards the sides of the PMT, the efficiency of the 450 nm light source gets slightly better.
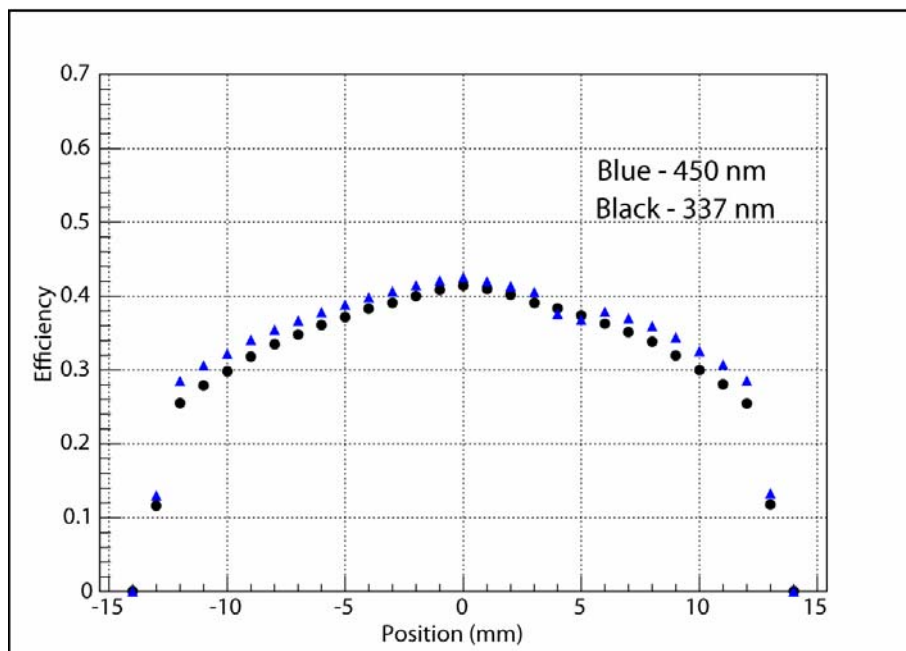
Figure 1.17: The efficiencies of a tapered light guide for 337 nm (black) and 450 nm (blue).

1.7 Conclusion

Three different types of reflecting material were tested for their radiation hardness in an air core light guide at the University of Iowa. The light guides were exposed to gamma rays with ^{137}Cs as the radiation source. The comparison of the light transmission efficiencies for three types of reflective films before and after 10 Mrad of irradiation shows that the Type-1 AM reflective film lost almost 14% of light transmission capability after 10 Mrad of radiation, while the HEM and Type-2 AM lost only about 3%.

Contrary to what would be expected, the reflectivity of aluminum on Mylar is not very resistant to radiation. Since the aluminum layer on the Type-1 AM sample was quite thin (60 nm), the Mylar layer was responsible for part of the reflection and its degradation

after irradiation caused the light loss. This can be avoided with a thicker aluminum layer which will reflect all the photons.

In the case of the Type-2 AM, there are 2 extra layers of 53 nm Nb_2O_5 and 66 nm SiO_2 on 10 nm of Cr adhesion and 70 nm aluminum reflective surfaces. A 75 μm thick polyester film was used for mechanical and thermal stability of the reflective film [25]. Extra layers make the photons reflect directly from aluminum which in turn makes the film radiation hard.

On the other hand, although the HEM material shows almost no degradation, it is known to luminesce after irradiation [27].

The light transmission efficiencies of the three reflective films were compared using three different light sources; a blue LED (450 nm), a UV LED (380 nm), and a mercury light bulb. The results showed that the Type-1 AM was better than the other two in the UV range. Even though the Type-2 AM reflective film has poorer light transmission in the UV region, it is superior in visible region. Also, the HEM is a good reflective film in the visible range but transmits light at 30 % of that of the Type-1 AM in the UV region.

Depending on the application one might prefer to use one or another of the reflective materials tested. The tests show that under high radiation environment the Type-2 AM would be a better reflective material choice for an air core light guide, provided that the incoming signal is in the visible region.

X-Y uniformity tests showed that the PMT X-Y uniformity improves and reaches a plateau when the HEM reflecting material is used instead of the AM. The tests also

show that there is no significant difference in the PMT responses when the straight and the tapered light guides are used. These results are confirmed with the simulations too.

Finally, according to the investigation of reflective properties of different materials, German Mylar and HEM are better reflective materials than Al-Mylar for 450 nm wavelength light.
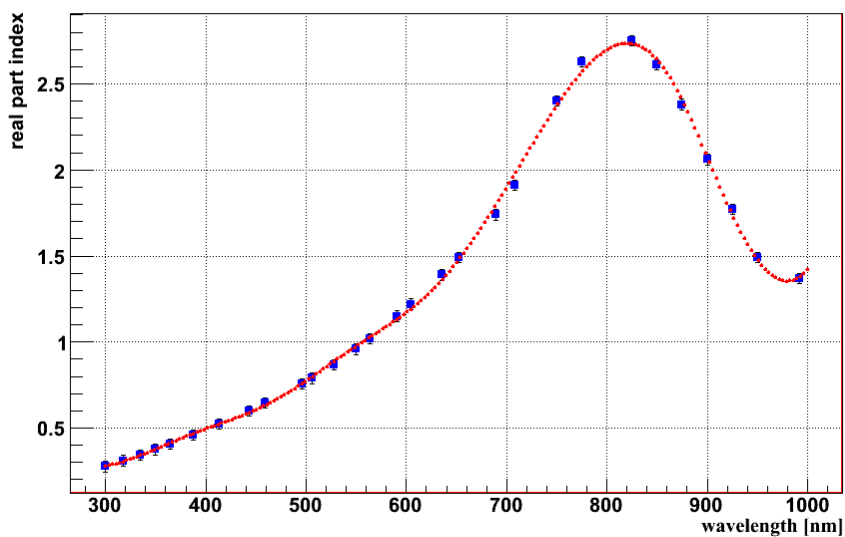
Figure 1.18: Real part of the refraction index for aluminum with respect to the wavelength.

CHAPTER II

CMS HADRONIC ENDCAP CALORIMETER UPGRADE STUDIES
FOR SUPERLHC: ČERENKOV LIGHT COLLECTION FROM
QUARTZ PLATES

2.1 Introduction

The nominal LHC performance for a beam energy of 7 TeV corresponds to a total beam-beam tune spread of 0.01, with 1.1 x 10^{11} protons per bunch, resulting in a luminosity of L ≈ 10^{34} cm^{-2} s^{-1} in the CMS. Upgrade scenarios for increasing both the luminosity and the beam energy are being discussed. The luminosity will be upgraded (later than 2010) to L ≈ 10^{35} cm^{-2}s^{-1}. We refer to this upgrade as the SuperLHC (SLHC). The comparison of some of the detector variables in LHC and SLHC is shown in Table 2.1.

	LHC	SLHC
√s	14 TeV	14 Tev
L	10^{34} cm^{-2} sec^{-1}	10^{35} cm^{-2} sec^{-1}
Integrated L	100 fb^{-1}/year	1000 fb^{-1}/year
Bunch spacing (dt)	25 ns	12.5 ns
N (interactions/x-ing)	~ 12	~ 62
Pile-up noise	1	~ 2.2
dN$_{ch}$/deta per x-ing	~ 75	~ 375
Tracker occupancy	1	5
Dose central region	1	10

Table 2.1: Comparison between the LHC and SLHC conditions.

The physics potential of the SLHC can be summarized as improvement in the accuracy in the determination of Standard Model (SM) parameters and of parameters of New Physics possibly discovered at LHC, extension of the discovery reach in the high-mass region and extension of the sensitivity to rare processes such as Higgs-pair production [30].

The detector performance at high luminosity will have an important impact on the physics output. Therefore, R&D is needed for the development of a detector technology able to operate safely and efficiently in such an environment [31].

2.1.1 Hadronic Endcap Calorimeter

As stated above, the hadronic endcap (HE) and hadronic barrel (HB) calorimeters are sampling calorimeters with 50 mm thick brass absorber plates interleaved with 4 mm thick scintillator sheets.

Figure 2.1: Mounting of the HCAL endcap (HE) on the disk of the endcap yoke.

The HE calorimeter consists of two large structures which are placed at each end of the barrel detector in the region of high magnetic field. Brass has been chosen as the absorber because it is not magnetic and has a high density (8.6 g/cm^{-3}). The barrel HCAL inside the coil is not sufficiently thick to contain all the energy of high energy showers. To solve this problem, additional scintillation layers (Hadronic Outher Barrels (HOB)) are placed just outside the magnet coil [2].
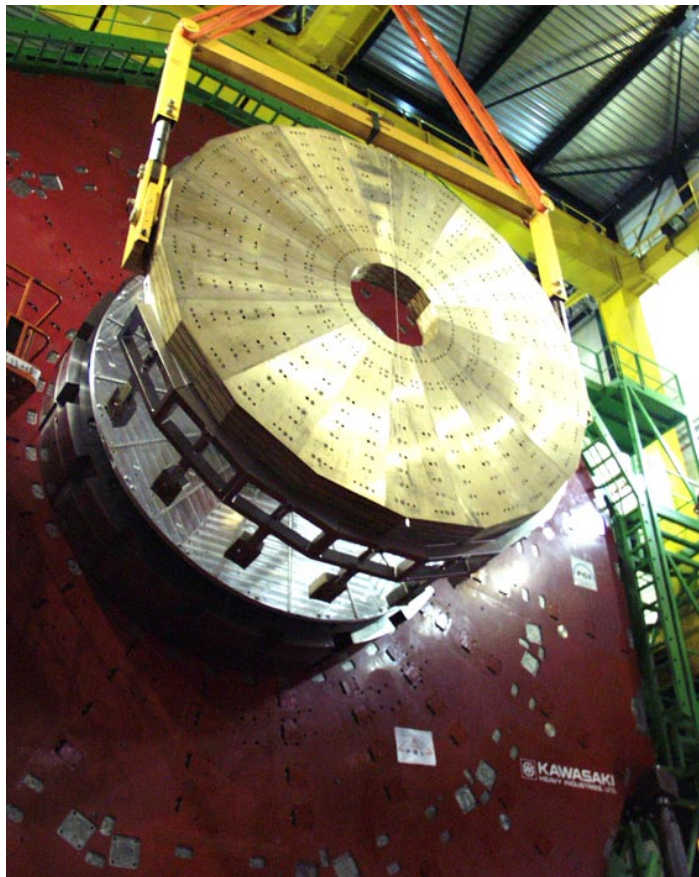
Figure 2.2: Mounting of the HCAL endcap.

Figure 2.3 shows scintillator sheets used to absorb light. Scintillator tiles are made of megatiles of large plastic scintillator sheets subdivided into components. Megatiles are

of the size $\Delta\eta$ x $\Delta\varphi$ = 0.087 x 0.087. Scintillation signals from the megatiles are collected using waveshifting fibers of just under 1 mm diameter. Megatiles are cut out on a special milling machine called a Thermwood which cuts tiles of varying dimensions and also makes keyhole grooves in the plastic into which the waveshifting fibers are inserted. To obtain optical isolation, gaps between adjacent tiles are filled with diffuse reflective paint [2].

Light is emitted in the blue-violet wavelength region of λ = 410-425 nm from the scintillators. Wavelength shifting (WLS) fibers absorb the light and emit green at λ = 490 nm. The green, wavelength sifted light is carried to the connectors at the ends by clear fiber waveguides [2].
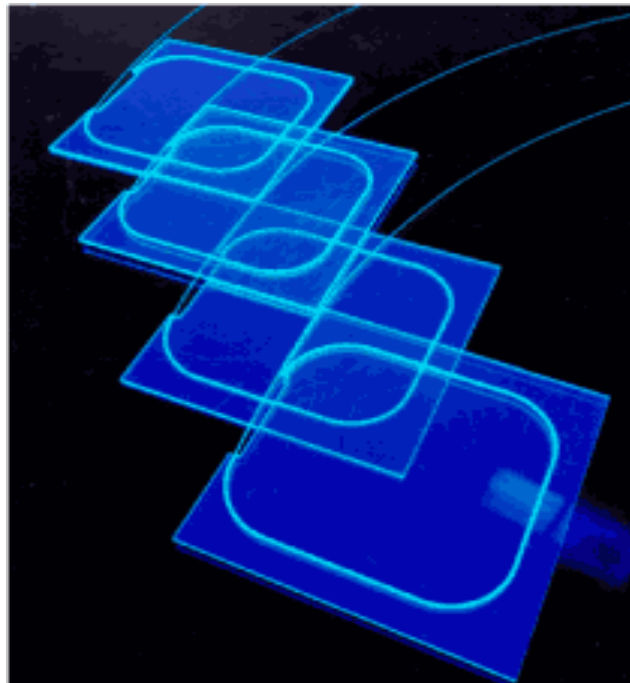
Figure 2.3: Scintillator sheets along with waveshifting fibers.

These scintillators are used in the hadronic calorimeter up to $|\eta| < 3$. They loose half of their light output after a dose of about 50 kGy. Since the CMS hadron calorimeters have ($|\eta| < 1.5$) in the barrel region, they will not experience radiation problems. However, the situation is different for the HE calorimeter. Scintillators in that region will loose their efficiency due to high radiation [2]. Table 2.2 and Table 2.3 show the radiation dose in Gy deposited in the scintillators of the HE and HB respectively for an integrated luminosity of 5×10^5 pb^{-1}. As can be seen, there is a big increase in the radiation dose at $\eta = 2.8$. The maximum dose is found to be 37 kGy [32].

z (cm)	$\eta = 1.5$	$\eta = 2.0$	$\eta = 2.8$
388	570	3800	24000

Table 2.2: Radiation dose (Gy) in the HE scintillators for an integrated luminosity of 5×10^5 pb^{-1}.

Radius (cm)	$\eta = 0.1$	$\eta = 0.6$	$\eta = 1.1$
198	190	250	300

Table 2.3: Radiation dose (Gy) in the HB scintillators for an integrated luminosity of 5×10^5 pb^{-1}.

2.1.2 Quartz Plates

The lifetime radiation dose for the HE is 2.5 Mrad for present LHC conditions. For the SLHC this value will increase to 25 Mrad. In the current HE design, Kuraray SCSN81 scintillator tiles, and Kuraray Y-11 double clad wavelength shifting (WLS) fibers are used. These materials were shown to be moderately radiation hard up to 2.5

Mrad. They lose about 20% of their light yield at 1 Mrad and 60% of it at 5 Mrad, which is unacceptable [32].

The scintillator tiles, as well as WLS fibers, used in the current design of the HE calorimeter will lose their efficiency due to high radiation doses. As a solution to the radiation damage problem at the SLHC era, we propose to substitute the scintillators by quartz plates and carry out the light via UV absorbing, blue emitting WLS fibers.

The radiation hardness tests performed on seven different types of quartz material show that quartz will not be affected by the radiation dose of the SLHC. However, when quartz plates are used, the detected photons come from Čerenkov radiation which yields 100 times less light than the scintillation process.

Čerenkov detectors are based on the fact that the light is emitted by a fast charged particle passing through an optically transparent medium which has an index of refraction greater than $1/\beta$ (= c/v) [33]. These detectors are in some regards similar to scintillation detectors. Čerenkov detectors are very fast since the light is emitted over a very short time. However, for Čerenkov detectors, a minimum particle velocity is needed and created photons have a direction centered along the particle velocity [34].

As stated, the most important disadvantage is the fact that the light level produced is very low. The total light yield due to Cerenkov photons is given by:

$$\frac{d^2N}{dxd\lambda} = 2\pi\alpha z^2 \left(\frac{\sin^2\theta_c}{\lambda^2}\right) = \frac{2\pi\alpha z^2}{\lambda^2 [1 - \frac{1}{\beta^2 n^2(\lambda)}]} \quad ,$$

where α is the fine structure constant, θ_c is the Čerenkov angle, λ is the wavelength of the emitted light, x is the path of the particle in the medium and z is the charge of the incident

particle. As can be seen, the number of photons and wavelength are inversely proportional to each other.

The aim of our study, which took place at the University of Iowa, Fermilab and Cern, was to develop a highly efficient method to collect Čerenkov photons from quartz plates.

Light will be collected with the help of waveshifting fibers. With quartz plates we propose to collect photons in the wavelengthrange from 400 to 200 nm and re-radiate them as blue light at 420 nm. To find the best solution we performed tests on quartz plates with different dimensions and with different waveshifting fiber configurations embedded in them.

2.2 Test Beams and Bench Tests

2.2.1 Radiation Hardness Tests

Quartz is known in general to be radiation hard. However, not all the quartz types have the same amount of radiation hardness. Therefore it is important to find the best quartz replacement for the CMS HE calorimeter tiles. For this purpose, seven different types of quartz material in the form of fiber from Polymicro Technologies were selected and tested. The quartz types chosen were FVP 300-315-345, FSHA 300-330-350, FDP 300-315-345, FBP 600-660-710, FVP 600-660-710, FVP 600-660-710 UVM, and FSHA 600-630-800 [35]. The fibers were tested for light transmission degradation in a high radiation environment for 313 hours by being bombarded with pulses of high-energy neutrons produced by the Intense Pulsed Neutron Source (IPNS) at Argonne National Laboratory.

Seven sets, with five fibers each, were placed in an irradiation tube about 25 cm away from the IPNS target. These fibers were irradiated for a three-week period during which the integrated current delivered to the IPNS target was 4456 A-hrs. The fibers were exposed to total of 17.6 MRad of neutron and 73.5 MRad of gamma radiation. The maximum fast-neutron fluence at the fibers was 7.42×10^{17} n/cm^2.

The optical transmission of the fibers was measured and compared to the baseline measurements. The setup, which is shown in Figure 2.4, has a light source and a spectrometer. The light was sent into a bifurcated optical fiber where it was split into two channels.
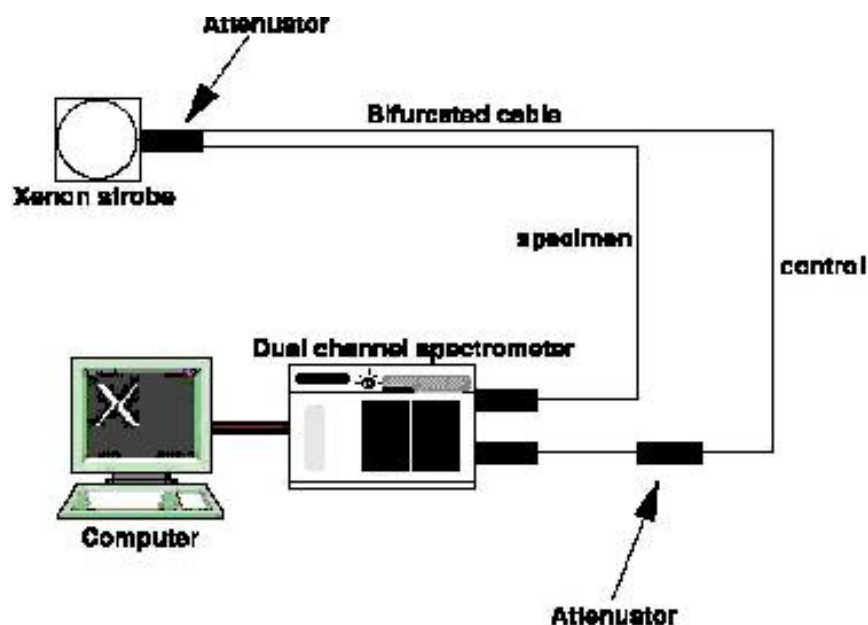
Figure 2.4: Radiation Setup.

According to the tests, a special radiation-hard solarization resistant quartz fiber (FBP 600-660-710) gives the best results. Solarization is defined as the change in

material properties due to the illumination of the material with UV light. In the quartz fibers exposed to high UV light, photo-thermal damage occurs resulting in an increase in scattering and attenuation. With solarization resistant quartz produced by Polymicro, it is possible to obtain long life and deep UV transmission [36]. The response of FBP 600-660-710, which is a 600 μm quartz core, quartz fiber clad with a polyamide buffer, to the radiation can be seen in Figure 2.5. The blue line shows the response of the plate after being subject to the radiation and red line shows the response before radiation.
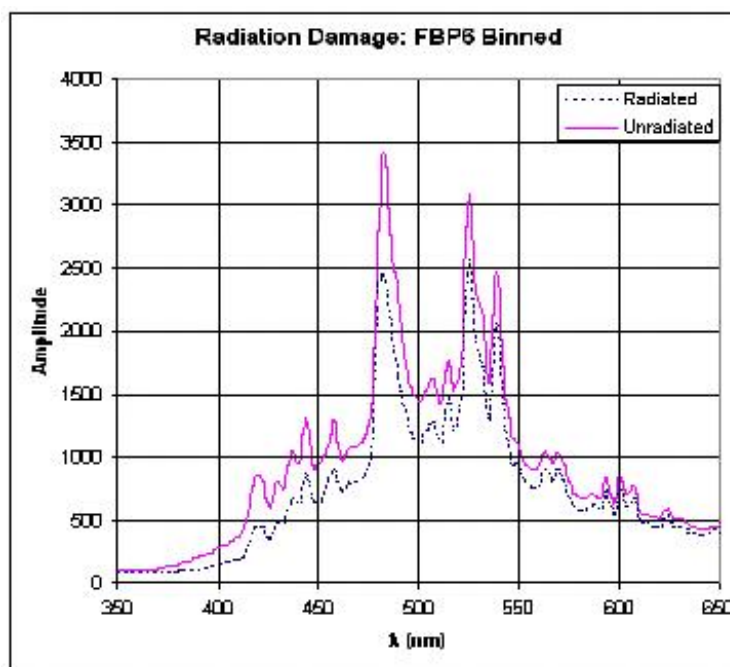
Figure 2.5: Response of the quartz fiber FBP 600-660-710
to the radiation: There is a very small difference in amplitude
before (red line) and after (dotted line) the radiation.

2.2.2 Reflective Material Tests

To trap the Čerenkov photons inside the quartz plates, we considered different wrapping materials; Mylar (M), High Efficiency Mirror (HEM), Tyvek (T) [37], and

Aluminum (Al) foil. For the reflectivity tests, we modified the light-guide tests setup explained in previous section. Each sample was mounted on a ring and placed at the end of a light guide. A Hamamatsu R7525 PMT [20] was mounted at the other end of the light guide to measure reflected light. An optical fiber carried light into the light guide and bounced it off the reflective surface back to the PMT. The mean charge values for each substance were measured. Also, another PMT was mounted behind the reflective sample to collect any light that may have transmitted through the sample. Some parts of the setup are shown in Figure 2.6.

Figure 2.6: Parts of the reflectivity tests setup.

To read the signal of the PMTs, a program for the CAMAC was developed. A tiny source tube was used to position the fiber inside the HEM-lined light guide. From the light guide studies, HEM is known to be good reflective material in visible region. A 337 nm Nitrogen LASER was used as a light source and a neutral density (ND) filter was set in the beam after the gate in order to attenuate the light.The thicknesses and other properties of the different samples used are shown in Table 2.4.

The sample	Thickness (in)	Properties
Al	0.0010	Opaque to room light; shiny and dull side
HEM	0.0019	Transparent to room light; shiny and dull sides
M1	0.0011	Opaque to room light; shiny and dull sides
M2	0.0010	Transparent to room light; shiny and dull sides
M3	0.0009	Opaque to room light; shiny and dull sides
M4	0.0010	Transparent to room light; shiny and dull side
T1	0.0138	Opaque to room light; shiny and dull sides
T2	0.0041	Translucent; shiny and dull sides

Table 2.4: The wrapping materials tested.

Each sample was measured for reflection and transmission on the dull (d) and shiny (s) sides. The voltage on the PMT was set to 1000 V and each sample was tested for 1000 gated pulses on each side. Figure 2.7 gives the results of reflectivity tests. The mean charge collected for each sample is shown.

Tyvek, with a thickness of 0.0138 in, was selected for wrapping the plates since it has the best reflectivity.
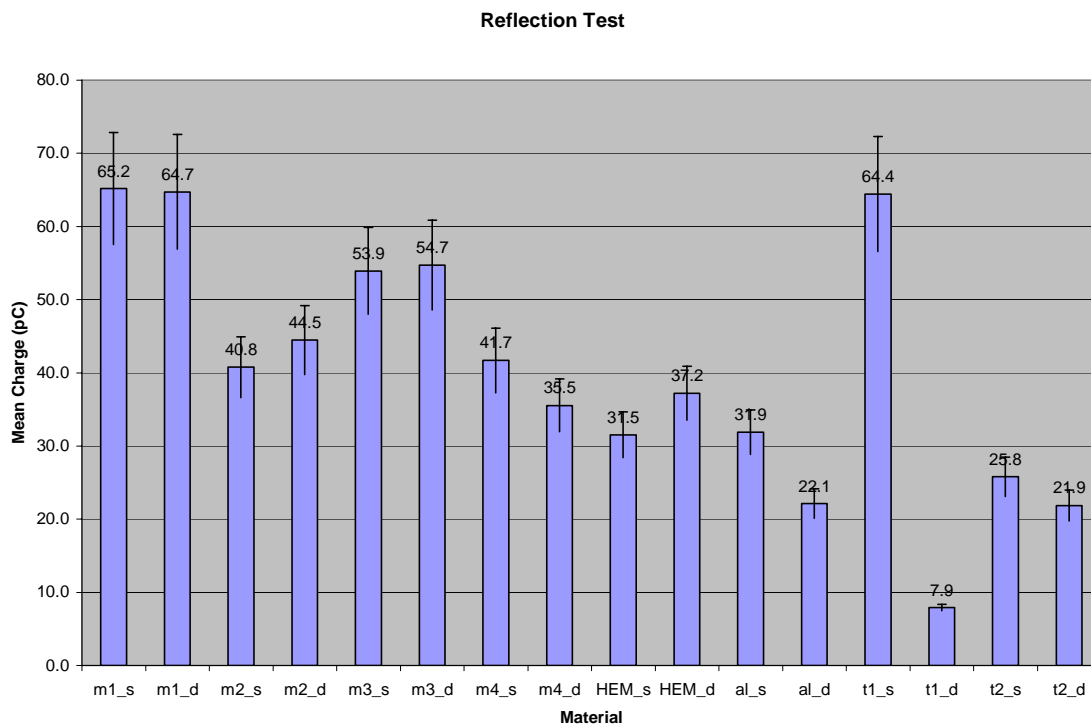
Figure 2.7: Results of the wrapping material tests.

2.2.3 Light Collection Tests

The number of generated Čerenkov photons increases as $1/\lambda^2$. Therefore, the emission is concentrated in the short wavelength region of the spectrum. To make up for the big deficit of light production, we decided to collect photons from the deep UV range. For this purpose, Saint Gobain BCF-12 WLS fibers, which can absorb photons down to 280 nm, and emit at 435 nm, were chosen. As can be seen in Figure 2.3, fibers in the original design of the HE scintillators collect photons from the edges of the plates. This simple fiber geometry works well for the scintillators because the scintillation photons are generated in random directions. However, the Čerenkov photons are not isotopic [34], but are generated at a fixed angle with respect to the momentum of the charged particle.

Since the photons are scarce we cannot afford to have them propagate to the edges of the plates. Because of this, we investigated the most uniform and efficient fiber embedding geometry to collect the Čerenkov photons.

Various fiber embedding geometries were considered, including: HE-Shape, Bar-Shape, O-Shape, Peace-Shape (a combination of O and Y shapes), Y-Shape, S&O-Shape (a combination of O and S Shapes), S-Shape and S&HE-Shape (a combination of S and HE shapes). These fiber geometries are shown in Figure 2.8.

All of the plates were wrapped with Tyvek, which is a very strong, synthetic material. As stated, bench tests showed that Tyvek is as good of a reflective material as aluminum and Mylar in the UV and visible wavelength region. In all the tests reported below Hamamatsu R7525-HA PMTs were used for signal read-out from the plates.

Light collection efficiencies and uniformities of the quartz plates were compared to those of the original HE scintillators in Fermilab test beams, and the bench tests at the University of Iowa. We also confirmed the results with GEANT4 simulations to be discussed later on.

Test Beam at Cern (July 2004)

The first tests on quartz plates were done at Cern in July 2004, during the HF test beam. Two UV (UVT) transmitting acrylic plates were put into a 100 GeV electron beam. The UVT acrylic has the same refractive index as quartz (1.45) and, other than not being radiation-hard, it behaves the same as quartz in creating Čerenkov photons.

Although the tests showed fewer Čerenkov photons as compared to quartz (due to the fact that UVT absorbs more in the UV region), UVT plates are good test tools because they are inexpensive and easy to machine
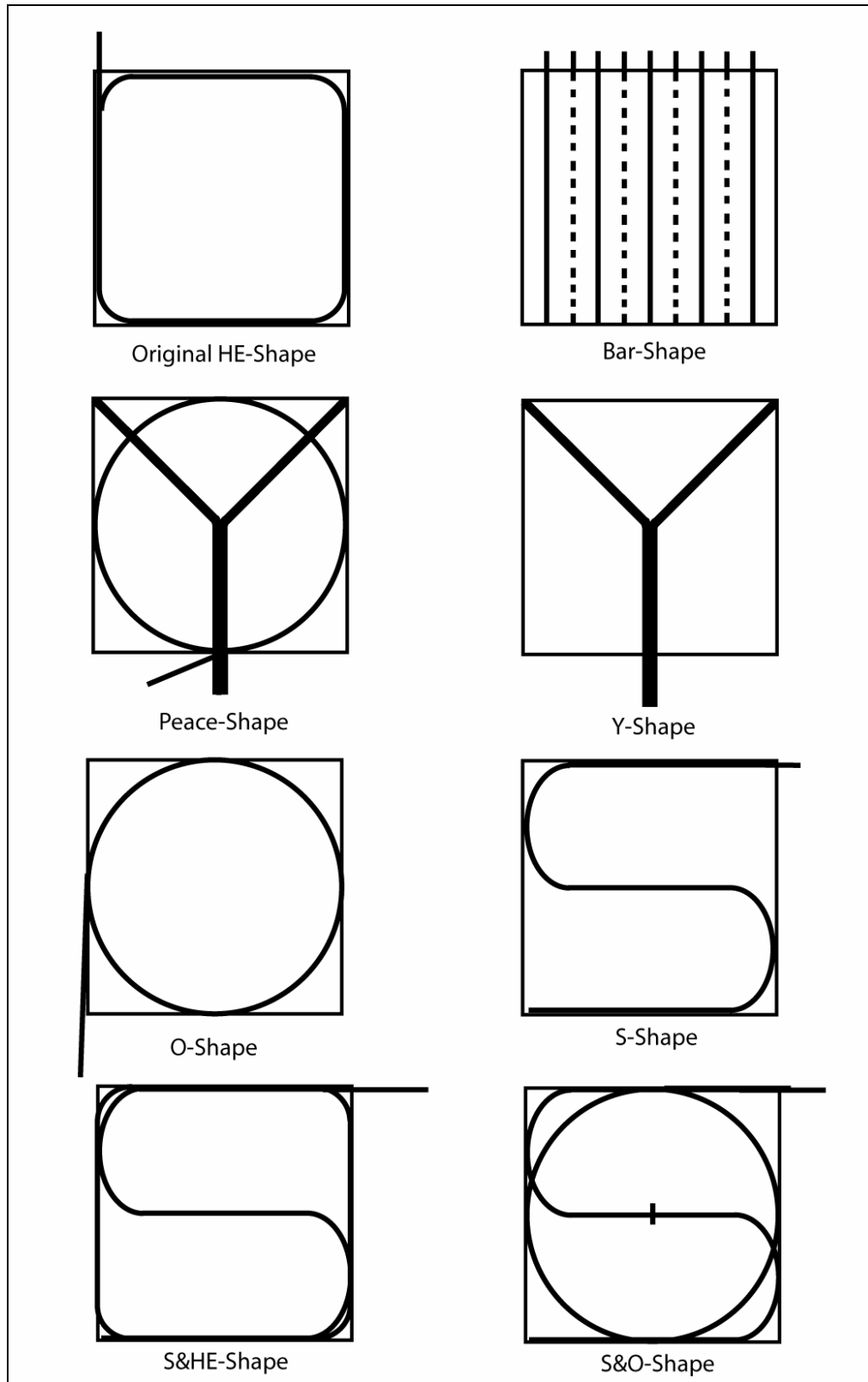
Figure 2.8: Different fiber geometries on plates.

In the Cern tests, one of the plates had a 3 mm thickness and a Y shape fiber configuration. The other one was a 6 mm S&HE-Shape fiber geometry. This test showed that it is possible to obtain the signal with plates (see Figure 2.9).
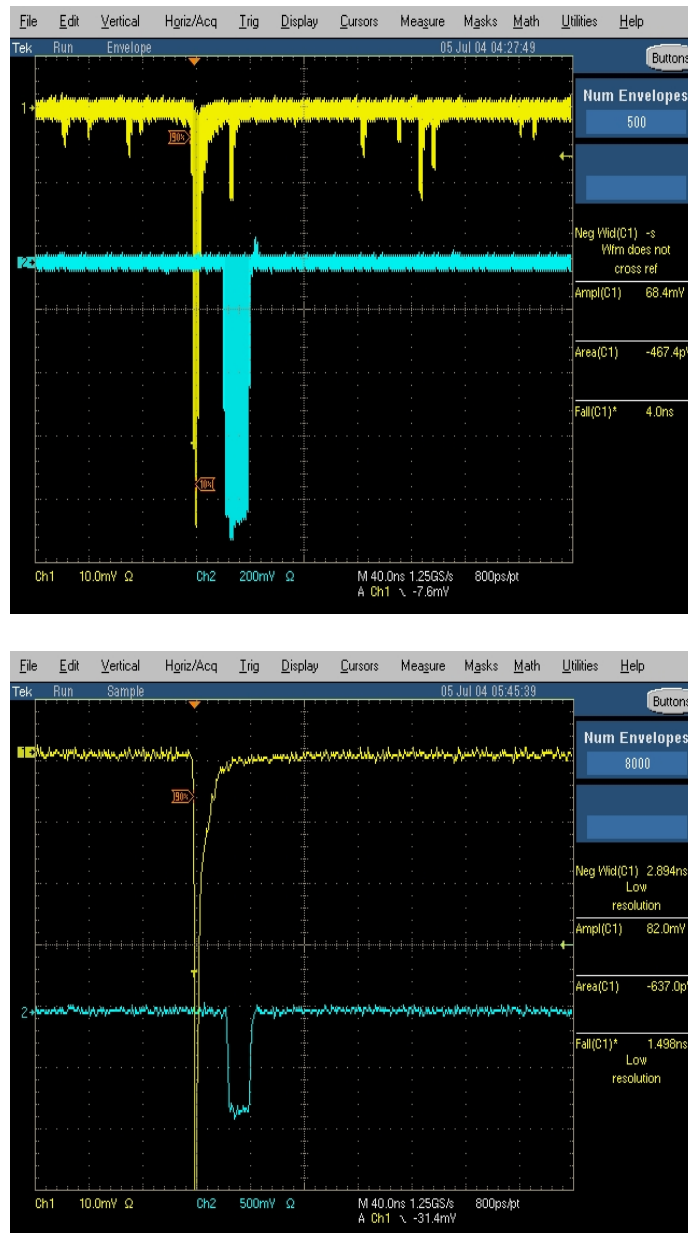
Figure 2.9: Signals obtained during a test beam at CERN.
The top (bottom) figure shows the signal obtained from the
plate with Y-Shape (HE and O Shape) fibers.

Fermilab Test Beams

In the span of 18 months we performed three independent tests with beams at the Fermilab M-Test facility.

The August 2004 run tested (20 cm x 20 cm x 3 mm) UVT plates, with different fiber geometries grooved into them. We used 0.6 mm diameter BCF-12 WLS fibers. The light collection efficiencies of these plates were compared to two (20 cm x 20 cm x 4 mm) original HE scintillators with original HE WLS fibers. The 120 GeV proton beam hit the center of the 20 cm x 20 cm iron block. We sampled the shower at 1 inch increments from 5" to 13" of absorber depths for all the plates.

Six different geometries, two different thicknesses of UVT and a single GE Quartz Plate were placed in the beam path at both 90 and 45 degrees with respect to the beam. The ratio of the charge collected by different plates to the charge collected by the HE scintillator versus absorber thickness is shown in Figure 2.10.
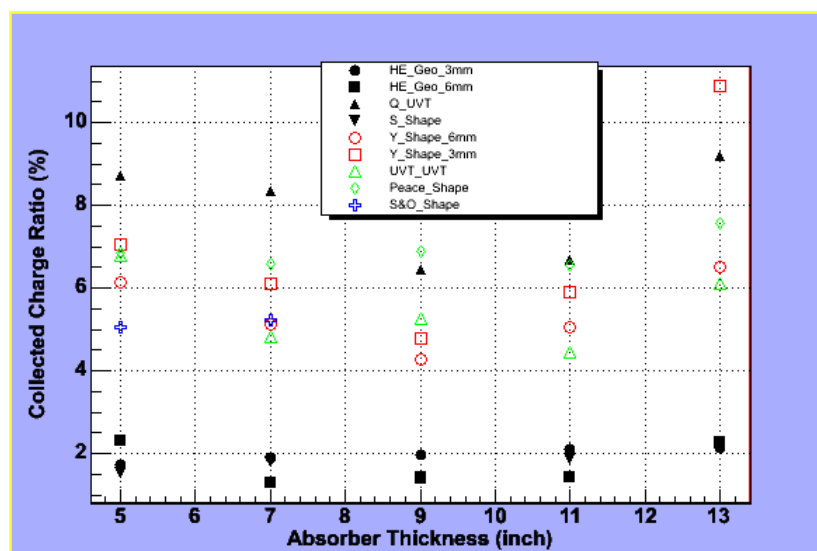
Figure 2.10: The ratio of the collected charge by different plates to the charge collected by the HE scintillator versus absorber thickness.

As seen in this plot, the HE-Shape yields less than 2% of the light that the scintillator plates would collect, whereas, with Y-Shape fiber geometry, it is possible to reach around 8% of charge ratio. This test beam showed that by varying the fiber geometries we can efficiently increase the Čerenkov light collection, but changing the angle does not have a visible effect on the results.

Also, due to the fixed angle nature of the Čerenkov photons, it is not suitable to locate the WLS fibers at the edges of the plates. Instead, the fibers should be placed close to the photons for efficient light collection. The surface uniformity tests that were performed later hint that the correct beam position adds a lot to light collection of the plates. In the HE, the beam will be spread uniformly across the plate.

In January, 2005, we performed tests on two sets of (10 cm x 10 cm x 3 mm) Polymicro solarization resistant quartz plates; 6 plates with high OH and 4 plates with low OH content. The quartz plates from GE quartz were also tested. These quartz plates were grooved with S-Shape, HE-Shape, Y-Shape and Peace-Shape fiber geometries. Again, the BCF-12 WLS fibers with 0.6 mm diameter were embedded into these grooves.

These quartz plates, and two (20 cm x 20 cm x 4 mm) original HE scintillators with original HE WLS fibers embedded in them were exposed to a 120 GeV, 64 GeV and 16 GeV proton beam. During these tests, the performance of liquid wavelength shifters and WLS fibers were also compared.

Showers were created with iron absorbers and sampled at different shower depths.

The amount of charge obtained from each geometry was compared to that of the original HE scintillator.

Figure 2.11 shows the plot of the percentage charge ratio of each plate with respect to the HE plate. On the x-axis there are the numbers assigned for each plate. The numbers and the corresponding plate type are as follows: 1-Low OH Y Shape, 2-Low OH HE Shape, 3-Low OH HE Shape 2 Fiber, 4-Low OH S Shape, 5-High OH Y Shape, 6-High OH S Shape 2 Fiber, 7-High OH S Shape, 8-High OH HE Shape, 9-UVT and Quartz, 10-Quartz-Quartz, 11-Liquid WS, 12 - UVT-GWSF, 13-High OH PEACE Shape, 14-Original HE Plate.
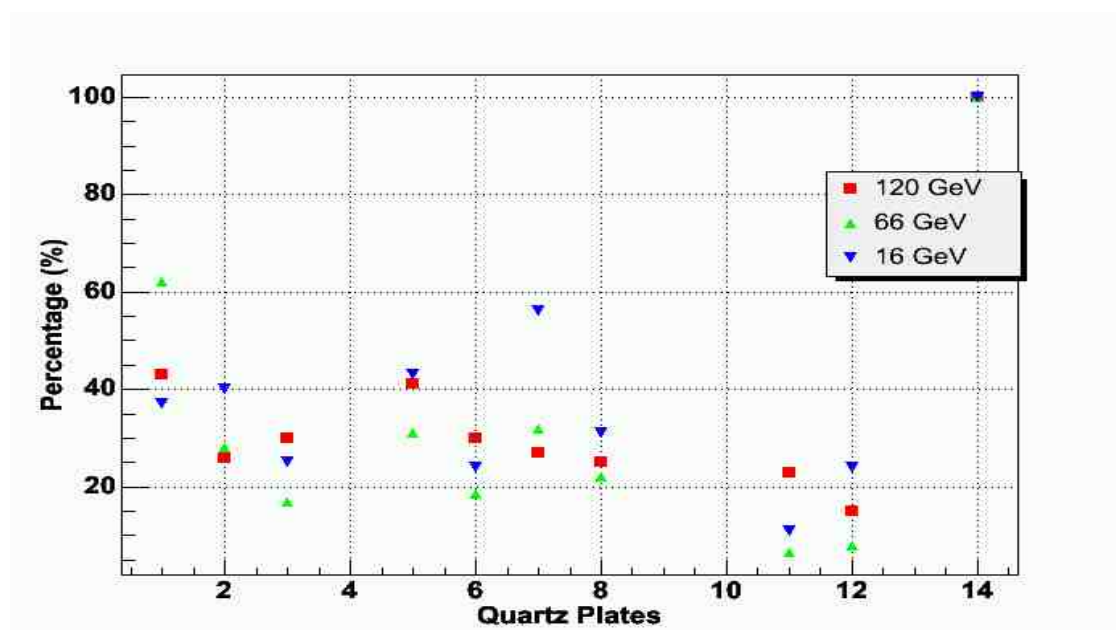
Figure 2.11: Percentage charge ratio of individual plates with respect to the HE plate.

Results of this analysis show that the Polymicro Quartz Plates give a better signal then the GE Quartz plates. Low OH is slightly more efficient than high OH quartz. The amount of light collected with the quartz increased dramatically compared to the UVT plates. Also, with smaller plate sizes, the probability that Čerenkov photons would be

captured by WLS fibers inside the plates was increased. As a result, the signal from the quartz plates was as much as 50% of that of the original HE plate.

Again, the HE-Shape yielded the worst charge collection efficiency as compared to the others. Also, we modified the S-Shape and HE-Shape plates to read the signal from both ends of the WLS fibers, which increased the light collection by almost 25%.

Finally, when the beam was sprayed onto all the plates with the help of a X-Y scanner to smear the geometric differences, it was seen that a signal of around 20% of the HE Plate was reached (see Figure 2.12).
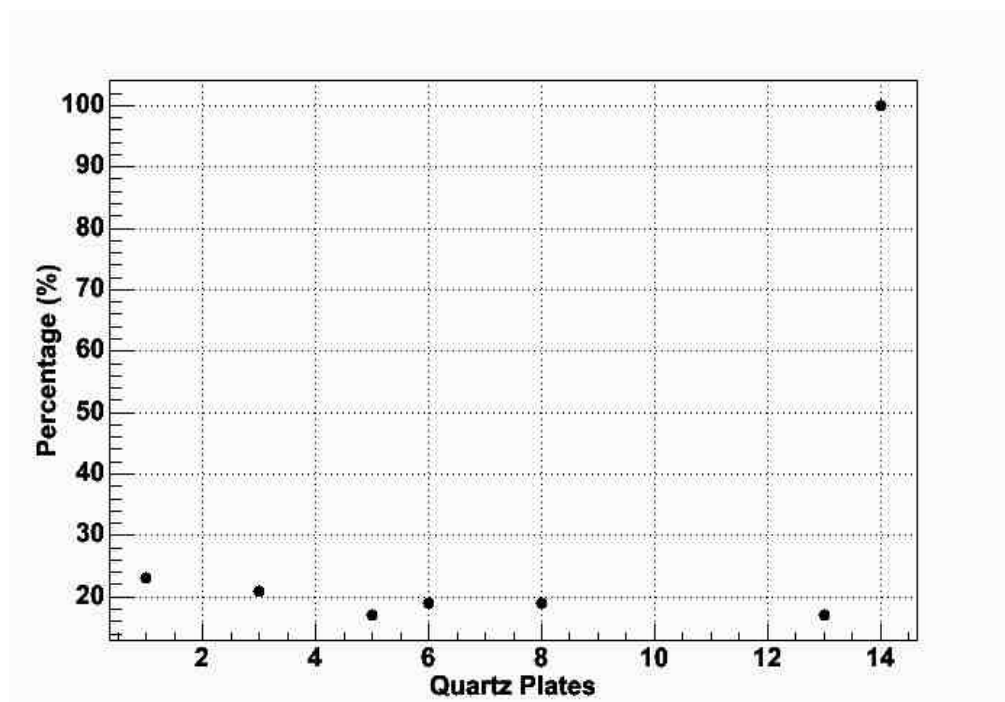
Figure 2.12: Results of the "surface scan".

From the previous test beams and the surface uniformity studies we concluded that:

a) For uniform Čerenkov light collection we need to distribute the fibers uniformly over the quartz plate.

b) Efficient light collection requires an increase in (i) the number of Čerenkov photons created by using thicker quartz plates, (ii) the cross section of Čerenkov photons to be captured by WLS fibers by using larger diameter WLS fibers.

To answer these efficiency and uniformity needs we designed a geometry called the Bar-Shape (see Figure 2.8) in which the fibers are uniformly distributed on both sides of the quartz plate.
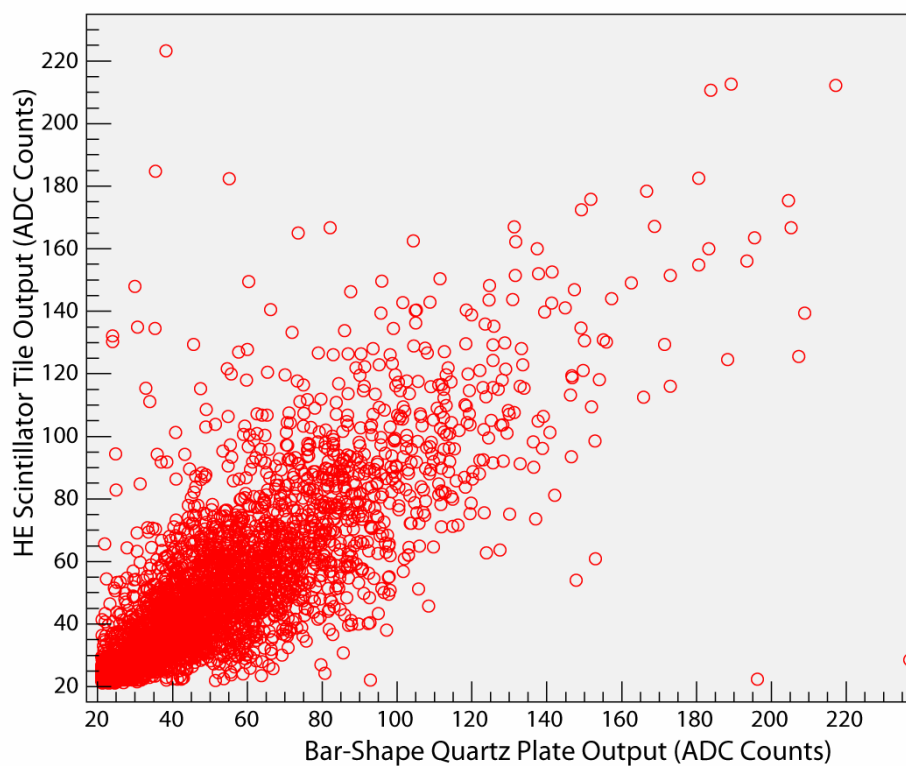
Figure 2.13: Comparison of the Bar-Shape to the HE scintillator: event by event ADC outputs from each plate. A weighted linear fit gives a slope of 1.42.

In January, 2006, we tested six Polymicro quartz plates with (20 cm x 20 cm x 6 mm) dimensions which were grooved in the Bar-Shape to hold 1 mm diameter WLS fibers. Figure 2.13 shows the light collection comparison between the HE scintillator and the quartz plate with the Bar-Shape fiber geometry. Most of the points lie on the diagonal of the plot implying that the light collection abilities of the two plates are similar.

All the test beam results are summarized in Figure 2.14. The light collection percentages of the quartz plates with four different fiber geometries with respect to the original HE scintillator are shown. It should be noted that the percentage increases to 70 percent with the bar shape.
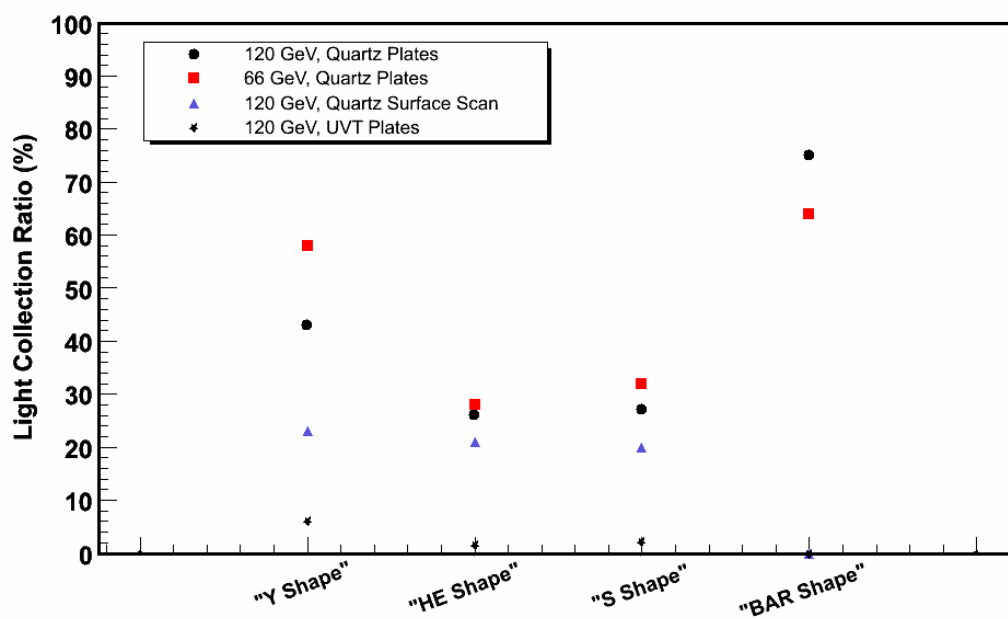
Figure 2.14: The light collection ratios of quartz plates with different fiber geometries as compared to the original HE scintillator.

2.2.4 Surface Uniformity Tests

At the University of Iowa CMS laboratories, bench tests were performed on all quartz fiber geometries for surface light collection non-uniformities.

A UV-LED (380 nm), nitrogen laser (337 nm), and mercury lamp were used as light sources to imitate Čerenkov radiation of various wavelengths in quartz plates. The mercury lamp has three emission wavelengths (253.65 nm, 365 nm, 404.7 nm). However, the absorption spectrum of the BCF-12 WLS fiber is from a wavelength of 280 nm to 435 nm, which eliminates the possibility of detecting the 253.65 nm photons with this setup.

The quartz plates with four different fiber geometries (S-Shape, Y-Shape, HE-Shape, and Bar-Shape) were tested for light collection uniformity.

Two dark boxes were used for these tests (see Figure 2.15). The light was generated in the first box and then carried to the second box by a quartz fiber of 600 μm diameter. Only one surface of the quartz plates was wrapped with Tyvek. The light coming out of the quartz fiber was directed onto the open surface of the plate from a 2 mm distance. The quartz plates were attached to a computer-controlled X-Y scanner that has the capacity to scan the surfaces with a 1/4000 inch step size. The light shining onto the surface was absorbed by the WLS fiber and shifted/carried to the Hamamatsu R7525 PMTs. For pulsing light sources (the UV-LED and Laser), the PMT signal was processed by a data acquisition system that included a CAMAC and a LeCroy 2249A ADC. For the DC light source (the mercury lamp) the PMT current was read by a picoammeter. The pulse frequency was 20 Hz for the nitrogen laser and 10 kHz for the LEDs. Neutral density filters were used to make the light intensities the same for all sources.
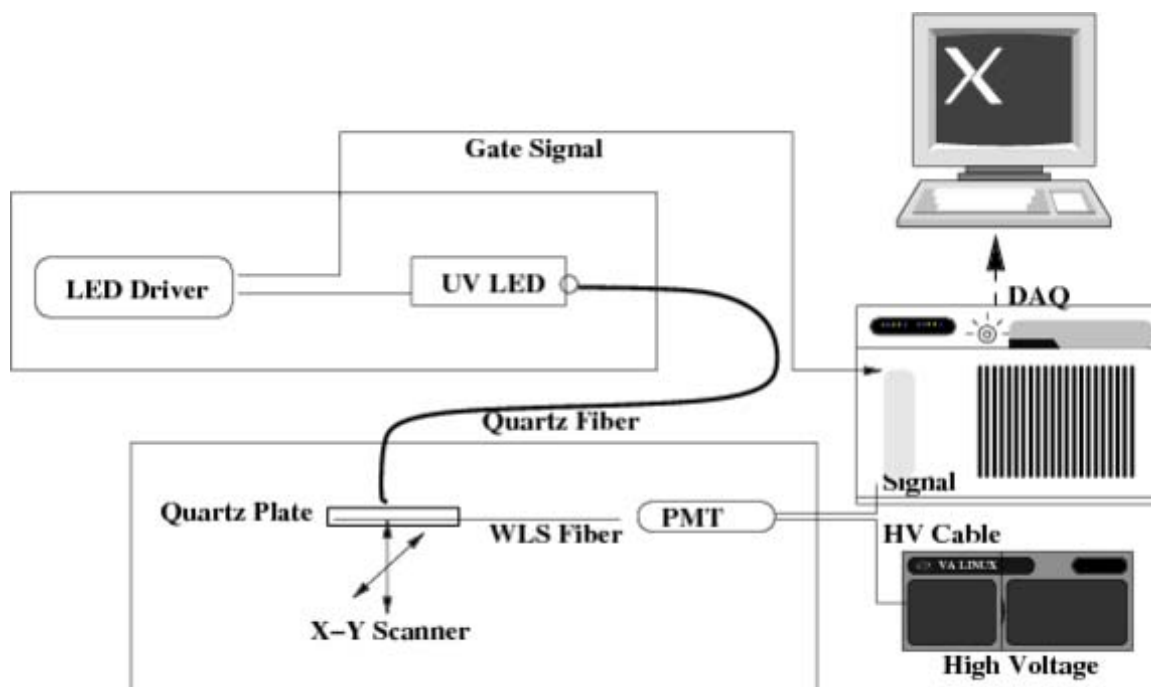
.
Figure 2.15: Surface uniformity tests setup in the University of Iowa CMS laboratories.

The current test design allows the comparison of the light collection uniformities of the different fiber geometries. The tests results are in good agreement with the GEANT4 simulations in which we can get absolute light collection uniformity values.

The bench tests show that the Bar-Shape is the most uniform geometry. The surface uniformity plot for the Bar-Shape fiber geometry is shown in Figure 2.16. This fiber geometry yields an even more uniform light collection than the original HE scintillator. The ratio of the Bar-Shape non-uniformity to that of the HE scintillator is measured to be around 0.75. All the other fiber geometries have a surface non-uniformity around twice the non-uniformity of the Bar-Shape. Figure 2.17 shows the surface scan of Y and HE-Shape.
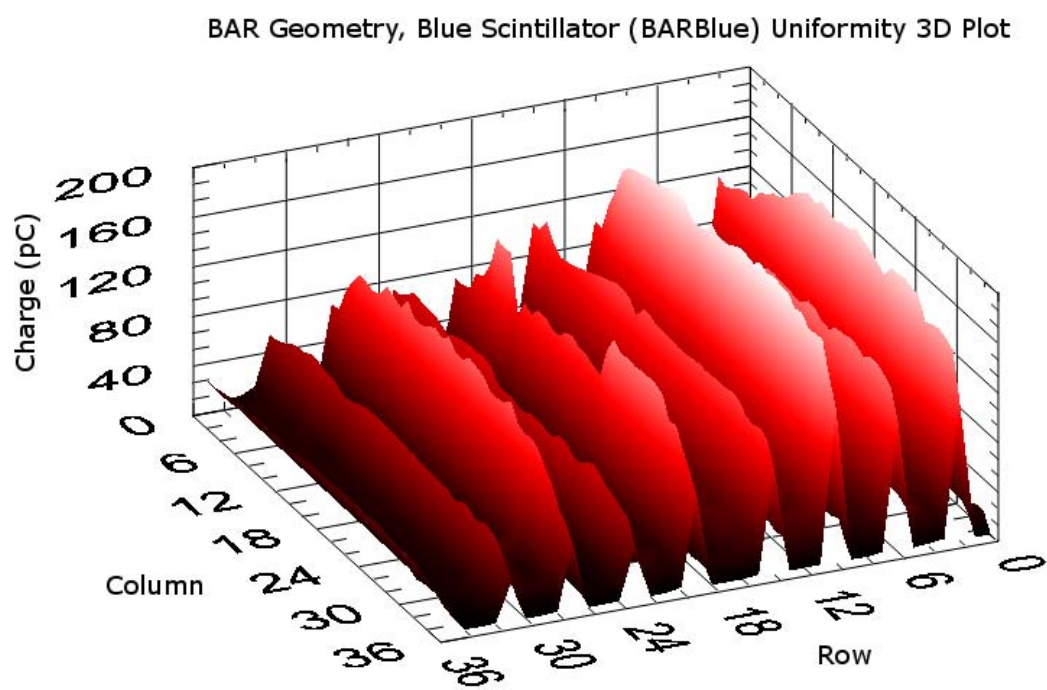
Figure 2.16: The charge collected by the Bar-Shape.
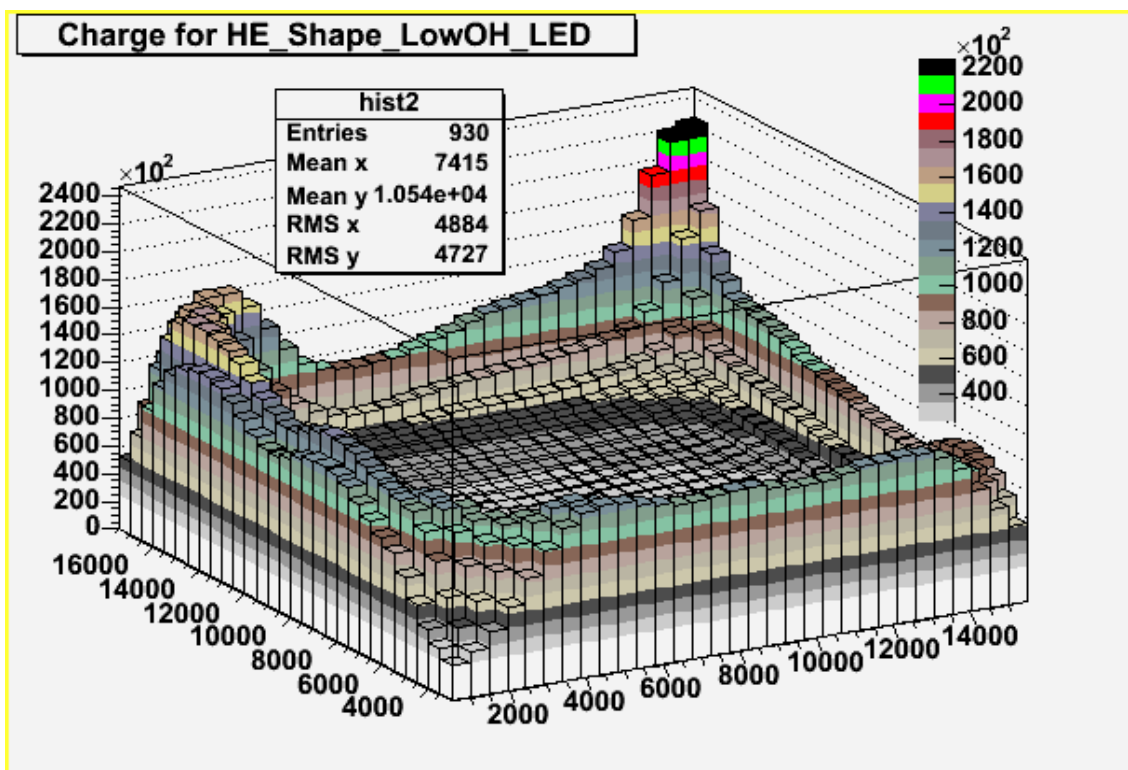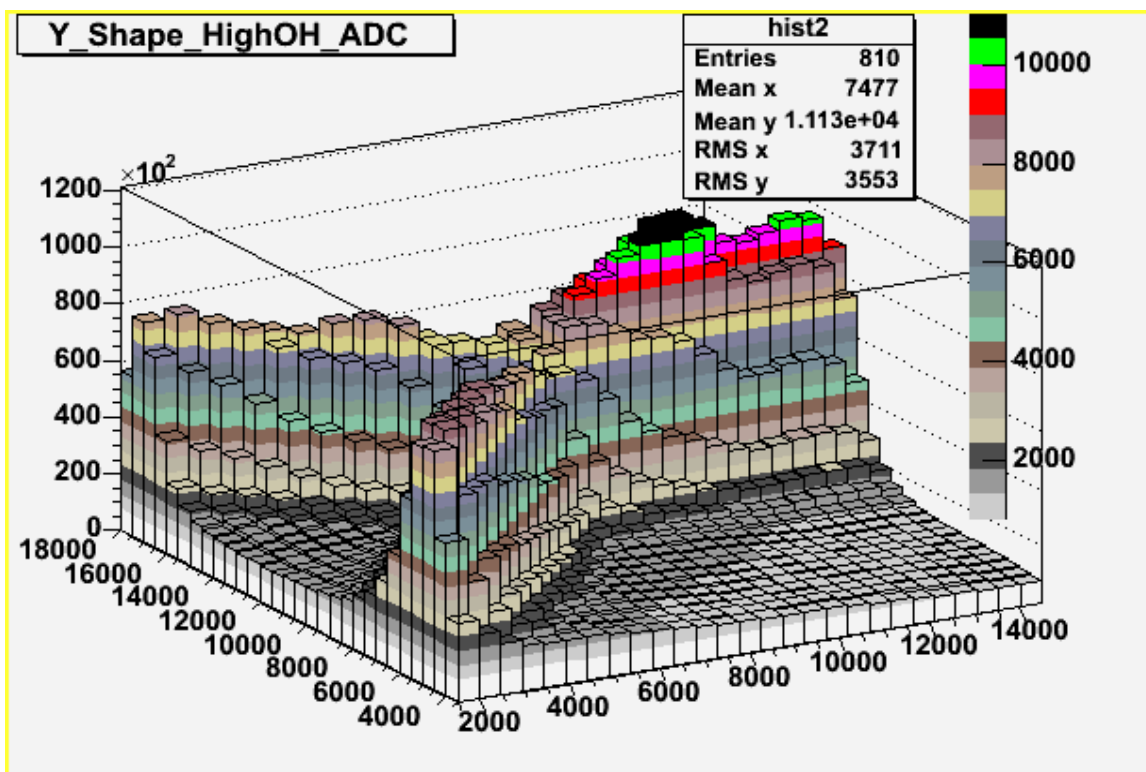
Figure 2.17: Charge collection from the quartz plates with Y-Shape and HE-Shape fiber geometries.

<u>2.3 Simulation Efforts</u>

We performed GEANT4 (C++ based detector simulation program) [38] simulations in order to study photon production, collection efficiencies and surface non-uniformities in a quartz plate and WLS fiber system.

As a first step, in order to understand the performance of quartz plates in a prototype detector model, we simulated a 1 x 1 meter hadron calorimeter with quartz and scintillating plates using the LHEP physics list. Figure 2.18 shows the visualization for one event of the model calorimeter with quartz plates. The current design of the HE has 19 layers of 50 mm brass absorbers with 4 mm scintillator or quartz plates between them.
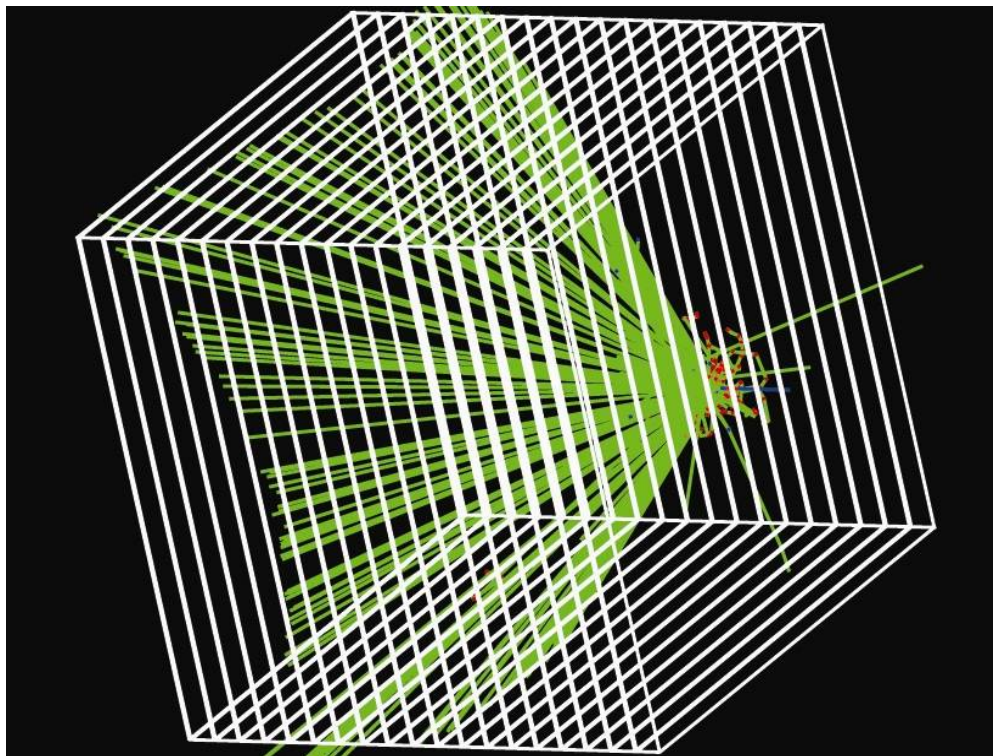
Figure 2.18: 1 x 1 meter box of Čerenkov photons on a fixed angle. The beam is 10 GeV pion.

As stated earlier, the ratio of the light produced by the Čerenkov process with respect to the amount of light produced by scintillation is very small. We started by simulating the number of Čerenkov photons and scintillation photons. Table 2.5 shows the ratio of Čerenkov photons to scintillation photons for different absorber thicknesses. The thicknesses of the quartz plates used were 3 mm and 5 mm and no fibers were used in these initial simulations. When the quartz was compared to a scintillator of 4 mm thickness the percentage was smaller than 3%.

Absorber	5 mm quartz	3 mm quartz
17.8 cm	2.14 %	1.32 %
22.8 cm	2.15 %	1.28 %
28 cm	2.11 %	1.26 %

Table 2.5: The percentage ratio of the Čerenkov photons to the scintillator photons for different absorber thicknesses. The scintillator thickness is 4 mm.

We also simulated the Fermilab test beam. We created 10,000 events for six different iron absorber thicknesses and two quartz plate thicknesses. The beams were 120 GeV proton and pion and, 100 GeV electron. According to the simulations, the thickness of the plates is directly proportional to the light collected (see Figure 2.19).

To see the improvement of the fibers, the WLS fibers were embedded in the quartz plate as in the actual plates. The Čerenkov photons created in the quartz plates were wavelength-shifted in the fiber and detected by the photocathode of the photomultiplier tube. Different fiber geometries were used in these simulations. Figure 2.20 shows four of the simulated fiber geometries.
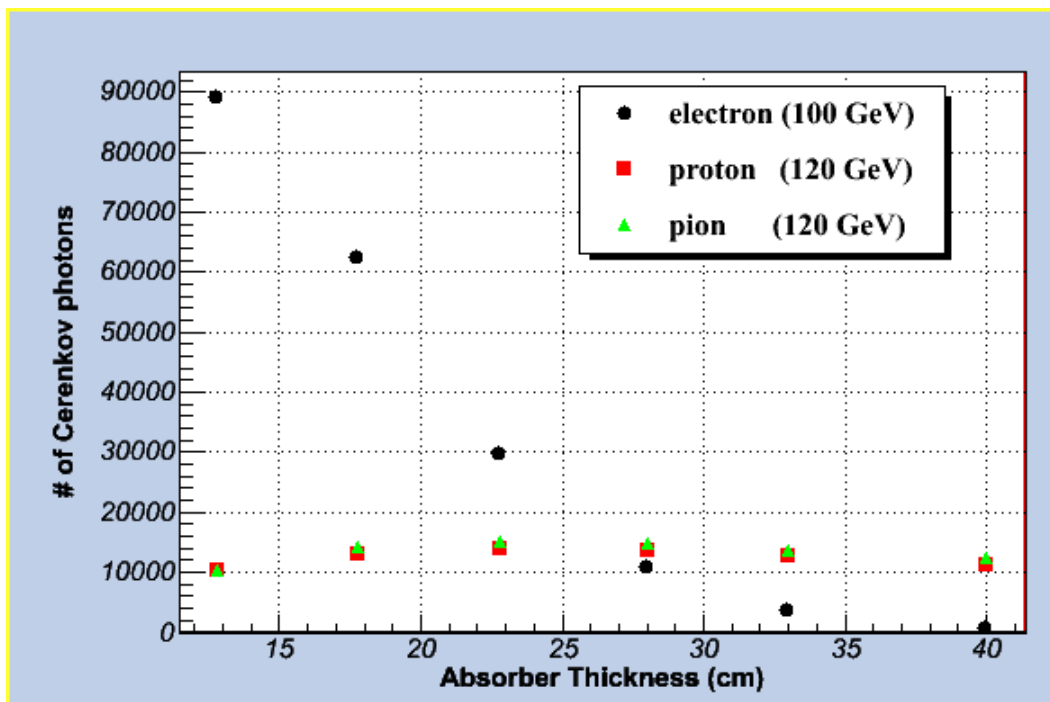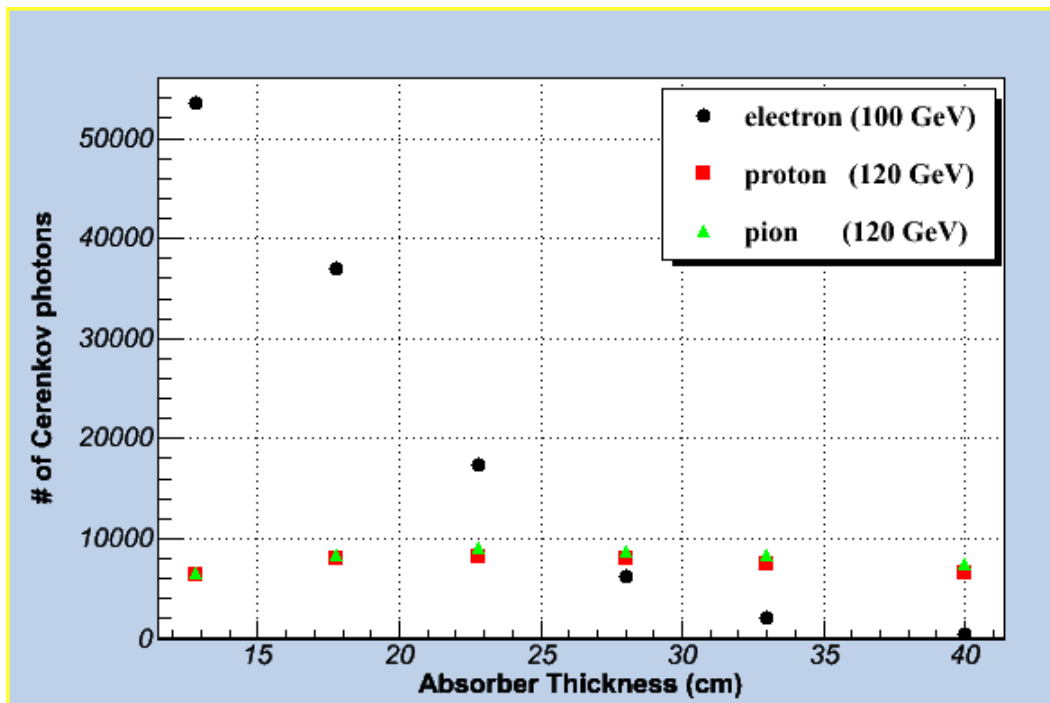
Figure 2.19: The number of generated Cerenkov photons versus absorber thickness. The left and right plots are for 3 mm and 6 mm thick quartz plates respectively.
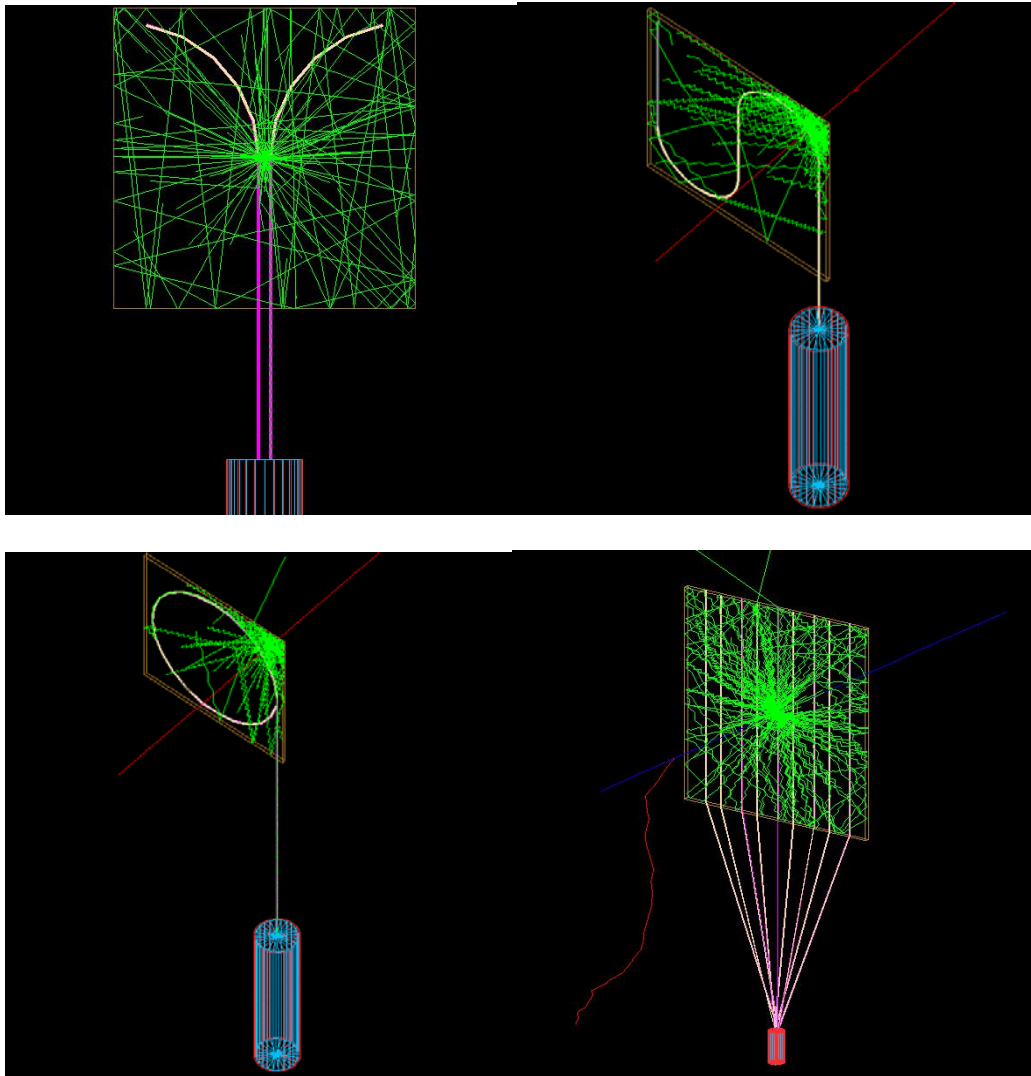
Figure 2.20: The simulated Fiber geometries: Y-Shape, S-Shape, O-Shape and Bar-Shape.

The quartz plates were 2 mm thick and had a cross sectional area of 10 cm x 10 cm. The WLS fibers had a core diameter of 600 μm. The quartz plates were wrapped with a reflecting material that has a 95% reflection efficiency to simulate the effect of the Tyvek. The quartz and WLS fiber attenuations were included in the simulation as well.

The absorption and emission spectra of the Bicron 91 WLS fiber was used in the simulations. As is shown in Figure 2.21, the absorption peaks around 425 nm, and below 390 nm the relative amplitude is less than 50%. The emission spectra maximum is around 495 nm and falls below 50% above 510 nm. The Čerenkov photons reaching the PMT were counted. Both the UVA and UVB regions were included (280nm) to simulate the UV photons.
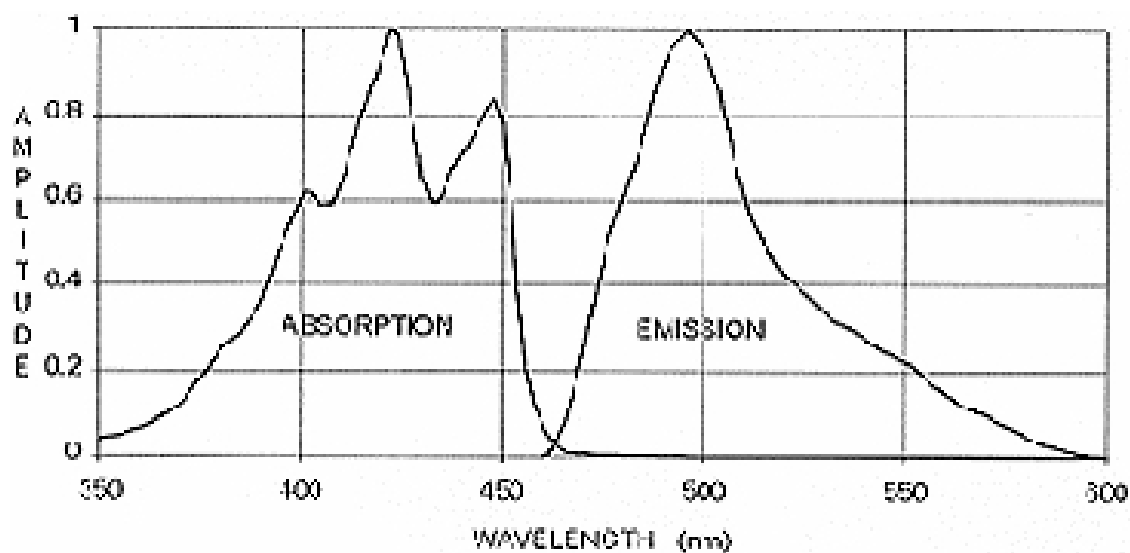
Figure 2.21: Absorption and emission spectrum of the Bicron 91 WLS fiber.

Some of the Čerenkov photons go into the core of the WLS fibers. Among those photons, the ones with energies that fall within the absorption spectrum energies of the WLS fiber are absorbed and then emitted as photons at a shifted energy. The Figure 2.22 shows the wavelength distribution of the Čerenkov photons generated in the quartz plate as a result of 4 GeV electron beam. Similarly the wavelength distribution of photons created in the WLS fiber is shown in Figure 2.23.
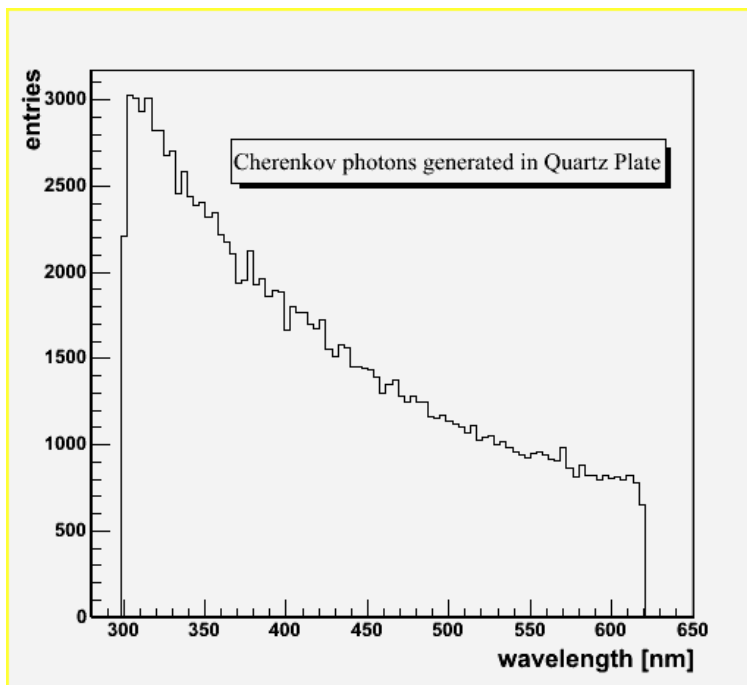
Figure 2.22: The wavelength distribution of the Čerenkov photons generated in the quartz plate.
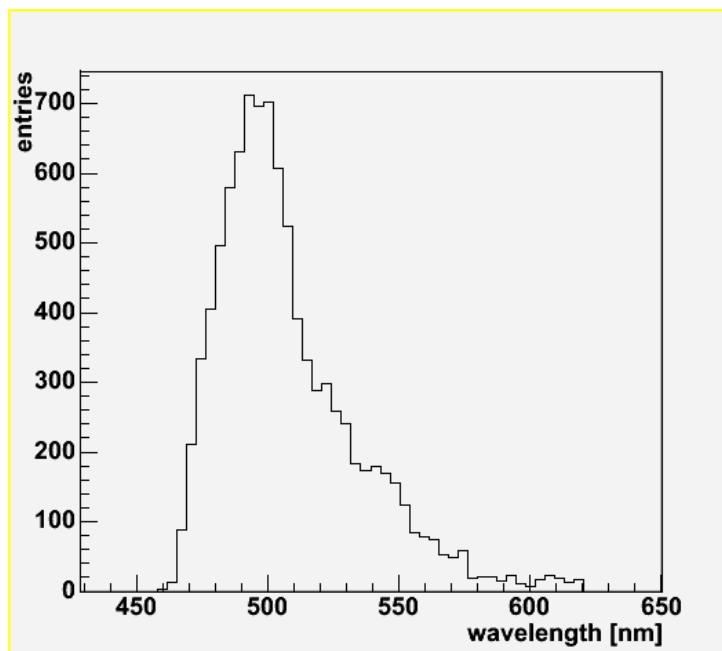
Figure 2.23: The wavelength distribution of the Čerenkov photons generated in the WLS fibers.

In order to compare the light collection efficiencies of different fiber configurations we have simulated a surface scan of the plates with a 4 GeV electron beam. The scan was carried out in a grid of 1 cm increments in the x and y directions. For each (x,y) point, a total of 1000 4 GeV electron events were recorded. For each event the total number of photons reaching to the photomultiplier tube cathode and their arrival time were recorded to be analyzed offline. The photon arrival time is defined as the time interval between the creation of the Čerenkov photons and the detection wavelength shifted photons by the PMT.

Figure 2.24 shows the profile of the number of photons reaching the PMT as a function of the beam position. The figures show that the PMT signals are larger when the beam is closer to the WLS fibers. As can be seen, the bar-shape geometry has a more uniform charge collection since the fibers are more uniformly distributed throughout the plate.

According to the simulations of the surface scan, the light collection non uniformities are 62%, 36%, 52%, and 26% for the HE-Shape, S-Shape, Y-Shape and Bar-Shape, respectively. These results are in excellent agreement with the bench tests. The Bar-shape has the most uniform light collection ability.

The comparison of the light collection efficiencies between different fiber geometries was done by taking the ratios of the mean number of photons collected at each beam position.

The simulated light collection ratios can be normalized with respect to the Bar-Shape. The values are as follows: Bar-Shape: 100%, Y-Shape: 90%, S-Shape: 85%, and HE-Shape: 70%. This same efficiency order is also observed at the test beams.
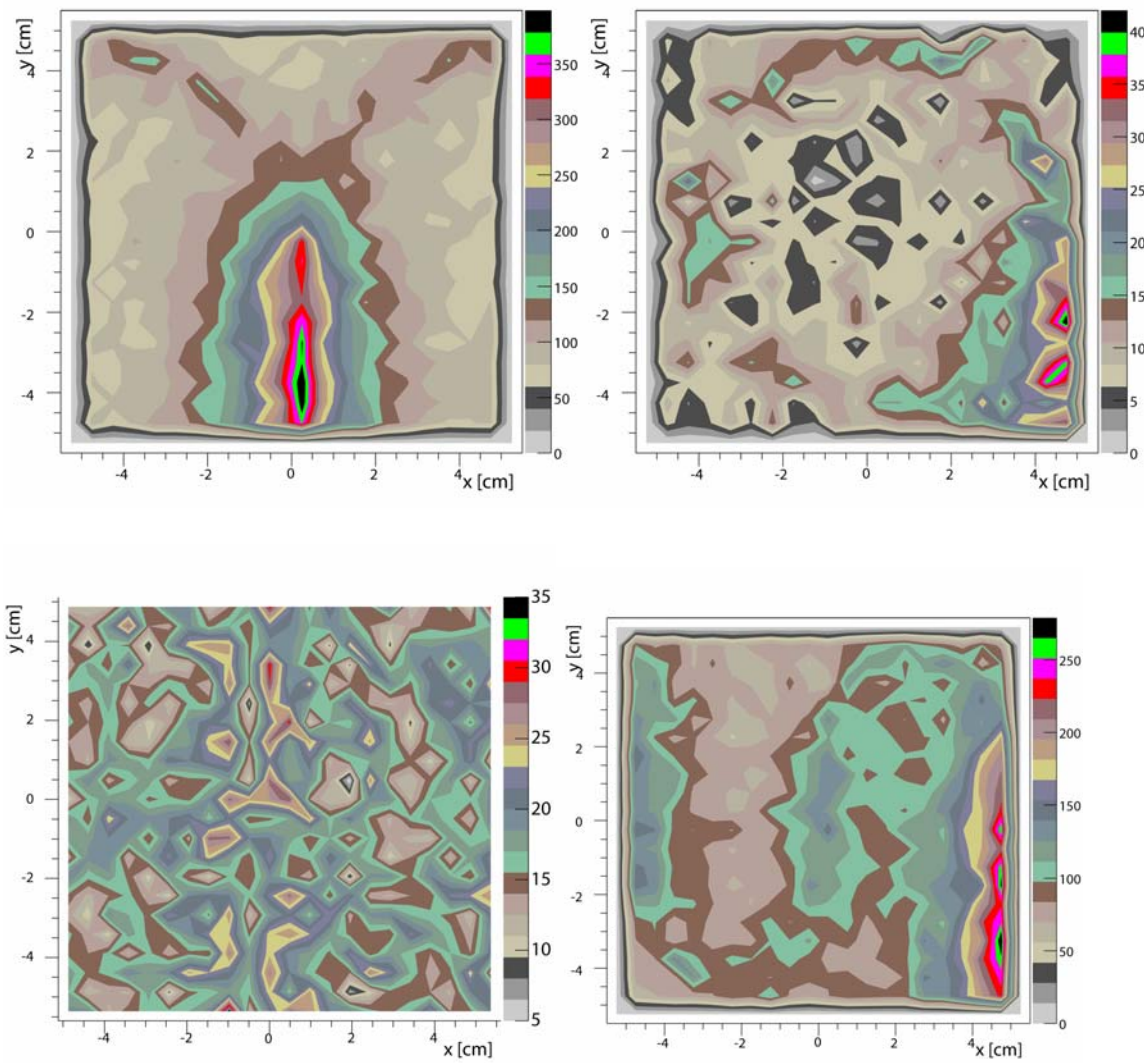
Figure 2.24: The color-coded plots for the light collected by the quartz plates with different fiber geometries (Y-Shape, O-Shape, Bar-Shape and S-Shape respectively).

Another important parameter is the arrival time of the photons to the PMT as there will be a finite amount of time that a gate will be opened to measure the signal. Simulations show that the mean arrival time of photons to the PMT cathode is less than 5 ns for all fiber geometries. Figure 2.25 is an example of a mean arrival time plot for the S-Shape fiber geometry.
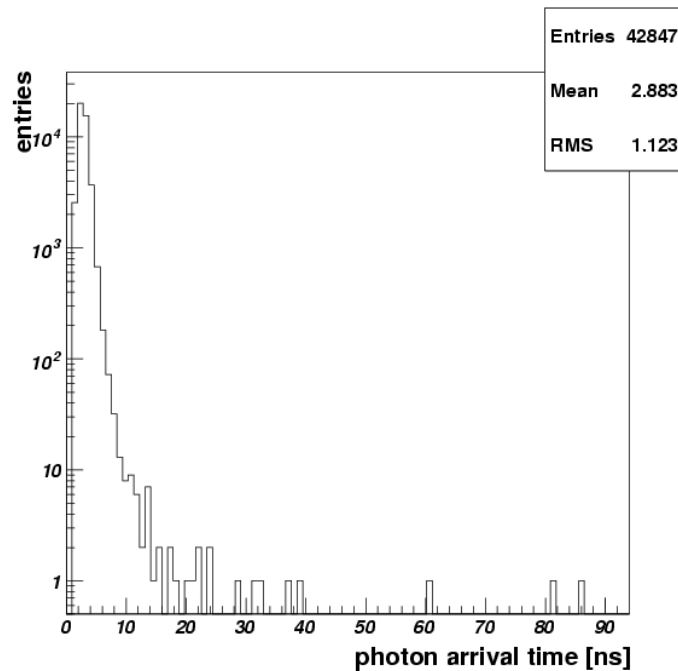
Figure 2.25: The photon arrival time for the S-Shape fiber geometry.

2.4 Conclusion

The current scintillator design of the CMS HE Calorimeter is not adequate for the high radiation environment of the upcoming SLHC era. We propose to replace the scintillator tiles by quartz plates which will collect photons from a Čerenkov process yielding much less light.

The radiation damage tests at Argonne Laboratories showed that the Polymicro FBP 600-660-710 solarization resistant quartz is the most radiation hard of the tested quartz types.

Simulations show that the amount of Čerenkov radiation in quartz plates is around 1 percent of the scintillation from the same size scintillator tiles.

To collect most light possible, we worked on different plates with different sizes and different embedded fiber geometries.

After many test beams and bench tests we came to the conclusion that with a quartz plate embedded with the Bar-Shape fiber geometry, we can collect almost 70 percent of the light that the original HE tile would yield.

The plate with the Bar-Shape fiber geometry is shown to be very uniform in light collection since the fibers are distributed uniformly throughout the surface.

To improve the light collection, thicker quartz plates with smaller size, and more embedded WLS fibers should be used. It should be remembered that the space between the absorber layers of the HE calorimeter (9 mm) limits the thickness of the quartz plates.

Elaborate simulations show that the surface non-uniformity is around 26% for the bar shape, and the ratio of collected light with respect to the HE scintillator is around 70%. The analyses of the mean arrival time showed that the light collection is extremely fast (< 4 ns) which makes quartz a good candidate in the SLHC era. Even if the 10x higher luminosity is obtained by decreasing the bunch crossing to 12.5 ns, the photon arrival time for quartz plates will be well within the gate.

PART B: PHYSICS SIMULATIONS FOR THE MSSM AND SM HIGGS

BOSONS IN THE CMS EXPERIMENT

CHANNEL III

THE MSSM H→TAUTAU LEPTONIC CHANNEL

3.1 Introduction: MSSM and JetMET Algorithms

3.1.1 The Minimal Supersymmetric Standard Model

The Minimal Supersymmetric Standard Model (MSSM) is the supersymmetric extension of the Standard Model (SM) with minimal particle content. It is built on the same gauge group as the SM: $SU(3)_C$ x $SU(2)_L$ x $U(1)_Y$ [39]. For each particle, there is a superpartner with the same internal quantum numbers, but with a spin that differs by half a unit. Since their gauge numbers are different, none of the SM bosons can be the superpartners of a SM fermion and vice versa. Minimal supersymmetry assumes that the interaction between particles conserves R-parity ($R = (-1)^{2j+3B+L}$), where j is angular momentum, B is the baryon number, and L is the lepton number. R = +1 for the conventional gauge bosons, quark, lepton and Higgs states, R = -1 for their supersymmetry partners [40]. As a consequence of R-parity conservation, sparticles are always produced in pairs, the lightest supersymmetric particle (LSP) is stable and heavier sparticles decay to lighter ones. LSP is believed to be a good candidate for the explanation of cold dark matter in the Universe [40]. The introduction of the supersymmetric partners cancels the quadratic divergence in the Higgs boson mass. The fine-tuning problem is solved in this way [41].

All of the SM fermions reside in chiral multiplets. Their scalar superpartners have the same name with the addition of a leading "s" (squarks, sleptons), whereas vector bosons are gauge supermultiplets in the SM. The fermionic superpartners of gauge bosons are named by the addition of "-ino" to the SM particle, such as gluino, wino. The

fermions and their sfermion partners, Higgs bosons and their Higgsino partners, and gauge bosons and their gaugino partners are shown in Table 3.1 [42].

Super - Multiplets	Boson Fields	Fermionic Partners	SU(3)	SU(2)	U(1)
gluon/gluino	g	$\widetilde{g}$	8	0	0
gauge/	$W^{\pm}, W^{0}$	$\widetilde{W}^{\pm}, \widetilde{W}^{0}$	1	3	0
gaugino	B	$\widetilde{B}$	1	1	0
slepton /	$(\widetilde{\upsilon}, \widetilde{e}^{-})_{L}$	$(\upsilon, e^{-})_{L}$	1	2	-1
lepton	$\widetilde{e}_{R}^{-}$	e_{R}^{-}	1	1	-2
squark /	$(\widetilde{u}_{L}, \widetilde{d}_{L})$	$(u, d)_{L}$	3	2	1/3
quark	$\widetilde{u}_{R}$	u_{R}	3	1	4/3
	$\widetilde{d}_{R}$	d_{R}	3	1	-2/3
higgs /	(H_{d}^{0}, H_{d}^{-})	$(\widetilde{H}_{d}^{0}, \widetilde{H}_{d}^{-})$	1	2	-1
higgsino	(H_{u}^{+}, H_{u}^{0})	$(\widetilde{H}_{u}^{+}, \widetilde{H}_{u}^{0})$	1	2	1

Table 3.1: The fields of the MSSM and their SU(3)xSU(2)xU(1) quantum numbers are shown. Only one generation of quarks and leptons are listed here.

The MSSM Lagrangian is composed of the sum of the SUSY generalization of the Standard model, and the SUSY breaking part.

$$L_{MSSM} = L_{SUSY} + L_{Breaking}$$

In the above equation, $L_{SUSY} = L_{chiral} + L_{gauge} + L_{gauge-interaction}$ where L_{chiral} and L_{gauge} stand for the Lagrangians for chiral and gauge supermultiplets respectively, and the last term includes the extra gauge interactions that are allowed [40].

Since the Higgs mechanism is a cornerstone for the SM and its supersymmetric extensions, the search for Higgs bosons is one of the main goals of high-energy experiments. The MSSM requires the introduction of two Higgs doublets in order to preserve symmetry [43]. The scalar potential of Higgs fields in MSSM is given by [40]:

$$
\begin{aligned}
V &= (|\mu|^2 + m_{H_u}^2)(|H_u^0|^2 + |H_u^+|^2) + (|\mu|^2 + m_{H_d}^2)(|H_d^0|^2 + |H_d^-|^2) \\
&+ b(H_u^+ H_d^- - H_u^0 H_d^0) + c.c. \\
&+ \frac{1}{8}(g^2 + g'^2)(|H_u^0|^2 + |H_u^+|^2 - |H_d^0|^2 - |H_d^-|^2)^2 \\
&+ \frac{1}{2}g^2 |H_u^+ H_d^{0*} + H_u^0 H_d^{-*}|^2
\end{aligned}
$$

There are five elementary Higgs particles: Two CP-even bosons (h^o, H^o), one CP-odd boson (A) and two charged bosons ($H^{\pm}$). At the tree level, the Higgs masses can be described by two independent input parameters, commonly chosen to be $\tan\beta = \upsilon_2/\upsilon_1$, the ratio of the vacuum expectation values of the two Higgs doublets, and the pseudoscalar m_A [43]. It is a distinctive feature of the MSSM that the mass of the lightest Higgs particle, h^0, is predicted to be rather low. In many recent calculations that include higher order contributions, it is shown that $m_h < 130$ GeV. It has been shown that at least h_0 should be observed at the LHC. Thanks to the high luminosity, the probability of detection of the other four MSSM Higgs is high [44].

The three regions of the MSSM Higgs sector are given as follows:

1) $m_A > m^{max}_h$, where H, A and H± are very heavy and almost degenerate in mass, and h_0 is similar to the SM Higgs. This region is called the "decoupling regime" and it looks to be the most probable region.

2) $m_A < m^{max}_h$, where H is similar the SM Higgs, but h and A are degenerate in mass. For large tanβ, h and A couple strongly to b-quarks and τ-leptons.

3) $m_A \sim m^{max}_h$ where h, H and A are degenerate in mass. This region is called the "intense coupling" regime [40].

The gluon-gluon fusion gg→H and associated production with b quarks in gg→bb-H are the dominant processes in heavy neutral MSSM Higgs production. At high tanβ values associated production dominates [45].

3.1.2 Jet and Missing Energy Reconstruction Techniques

To be able to understand event signatures for Higgs boson production, SUSY, MSSM and many other physics processes, it is necessary to reconstruct and measure jets coming from high momentum quarks and gluons, and missing transverse energy (MET) [46, 47].

The big QCD cross section shows that jets will dominate the high P_T physics at the LHC. The jet resolution and linearity play an important role in separating the signal from the background. Solving the problem of associating a jet measured in a calorimeter with a scattered parton is an important issue. The calorimeter towers are used as an input to several jet algorithms [48].

Jet and MET reconstruction is a very complicated process. Currently, with the CMS software, multiple algorithms for the jet finder, MET reconstruction and several scenarios of JetMET analysis are implemented in ORCA. Correction and calibration are

important aspects in Jet and MET reconstruction. Jet and MET algorithms are sensitive to the final states accompanied with the pileup, multiple-scattering, underlying-events, and detector (mainly calorimeter) performance [49].

All the Jet reconstruction code is within the ORCA Jets subsystem. There are several jet algorithms such as Simple Cone, Iterative Cone, Successive Combination, Kt, Inverse colour dipole model, JADE, Durham and Cambridge. Midpoint cone, iterative cone and kT algorithms are currently available in the CMS software [50].

In hadron collider experiments, the midpoint and kT cone algorithms are usually used in offline analysis, whereas, the iterative cone algorithm, because it is fast and simple, is used for jet reconstruction in software-based trigger systems [46]. The jet algorithms can be used with either the energy or E_T recombination scheme.

When calculating the axis of a jet, the contributing energy deposits are weighted by their transversal energies E_T ($E_T = E\sin\theta$) which is Lorentz invariant. In this way, a high energy particle contributes more to the calculated jet direction than a low energy particle.

Weakly interacting particles like neutrinos in the SM and the LSP in the MSSM do not deposit energy in the calorimeter. The minimum ionizing particles such as muons deposit little energy. These contribute to a significant vector sum of the transverse energy of all the detected particles, and the imbalance of energies corresponds to the missing transverse energy (MET).

All the MET reconstruction code is contained within the ORCA MET subsystem. The performance of the calorimetry has a huge impact on MET quantities. A JetMET analysis should be prepared to deal with detector issues and to make reconstruction

robust, reliable and less sensitive to those issues. In addition to the existing online Jet Finder algorithm and MET reconstruction, the offline Jet and MET resolution will play a big role in the Higgs, SM and New Physics (SUSY ..) channels, which depend highly on the significance of signal vs. background [50].

Measuring MET at the CMS will be complicated due to pileup collisions, a difference between photon and pion responses in the calorimeters and the bending of the tracks by the high magnetic field [47]. However, the good forward coverage of the CMS, the good cell segmentation and hermeticity simplify the MET measurement [47, 49, 32].

To calculate the MET the individual calorimeter towers with energy E_n, pseudorapidity η_n, and azimuthal angle φ_n are summed together. The formula is given as:

$$MET = -\sum[(\frac{E_n \cos\varphi_n}{\cosh\eta_n})x + (\frac{E_n \sin\varphi_n}{\cosh\eta_n})y] = MET_x + MET_y$$

To take into account the reconstructed muons, the expected calorimeter deposit (~ 4 GeV) is replaced by the reconstructed track P_T [47].

3.2 MSSM Leptonic H/A→ τ τ Channel

One of the goals of the LHC is to cover the entire m_A – tanβ plane for the purpose of discovering or excluding the existence of the MSSM Higgs sector. The low tanβ values are excluded by the LEP [51]. In the MSSM, almost the entire Higgs sector can be covered with 30 fb^{-1} by the LHC experiment [41]. Among several MSSM decay modes, the two channels having tau (τ) lepton final states are of great importance: H/A → τ τ and H$^+$ → τ υ [43].
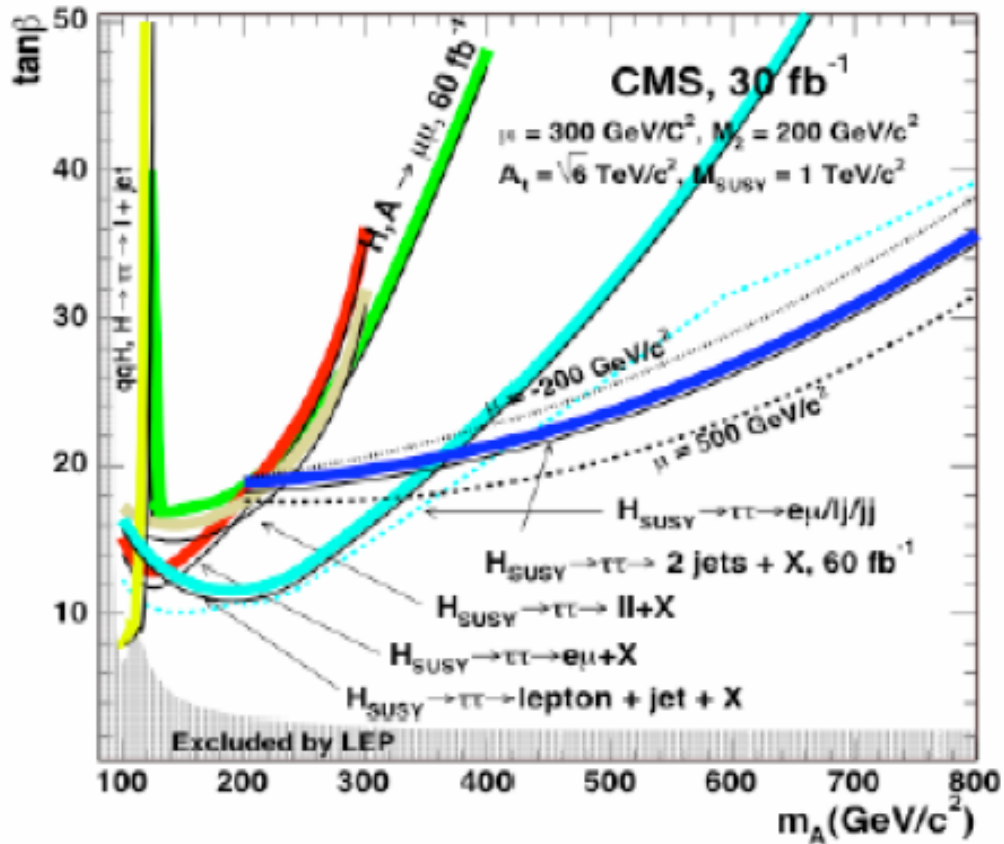
Figure 3.1: Cross sections of several decay channels for different tanβ and m_A values. H/A → $\tau\tau$ is the most promising channel in the search for neutral heavy MSSM Higgs bosons, and it is particularly significant at high tanβ [43]. The H → $\tau\tau$ rate is much more enhanced in the MSSM case than the SM one [52]. For tanβ = 30 and m_A = 300 GeV, the ratio of the MSSM cross section to the SM cross section is around 5000.

In this decay, two b-quarks are created along with the Higgs boson which decays into two τ's. Both τ's decay leptonically resulting in a final state of two leptons (any combination of electrons and muons) and four neutrinos. The Feynman diagram for this channel is shown in Figure 3.2.
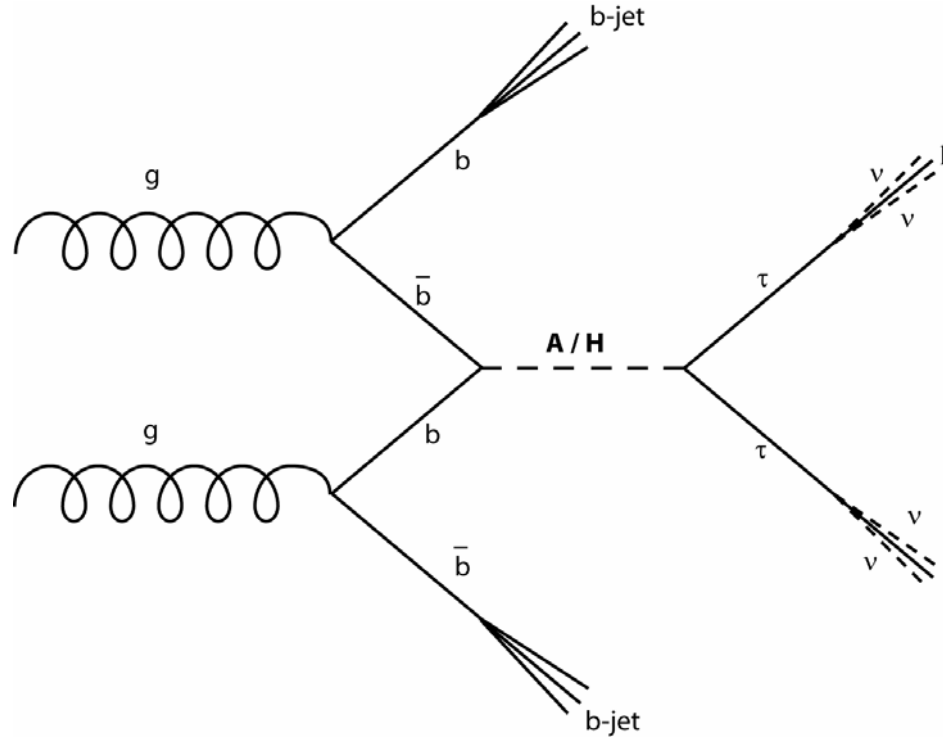
Figure 3.2: Feynman diagram for the signal channel.

The tau decays require the interplay of different detector elements in order to measure missing transverse energy due to the escaping neutrinos, leptons and jets. Some b-tagging could be necessary in order to suppress the background when b-quarks are produced along with Higgs boson.

We studied $gg \to bbH^0 \to \tau^+\tau^- \to l^+l^-\nu\nu\nu\nu$ for three different Higgs' masses and with tanβ = 20, where l represents an electron or muon. The masses and corresponding event numbers are 140 GeV with 38,000, 200 GeV with 20,000 and 250 GeV with 10,000. DC04 data sets are used to obtain the digitized events which are then processed with ORCA 8-7-4 ExRoot.

In order to study the MET and Jet Correction effects, it is necessary to understand the properties of the channel. The kinematic properties of this channel are investigated below.

3.2.1 b-quarks

In this specific decay, we have two b-quarks along with the Higgs boson. Every event has one low E_T and one high E_T b-quark and their corresponding jets. In Figures 3.3 and 3.4, the E_T distributions for the quarks are shown for the 200 GeV sample.
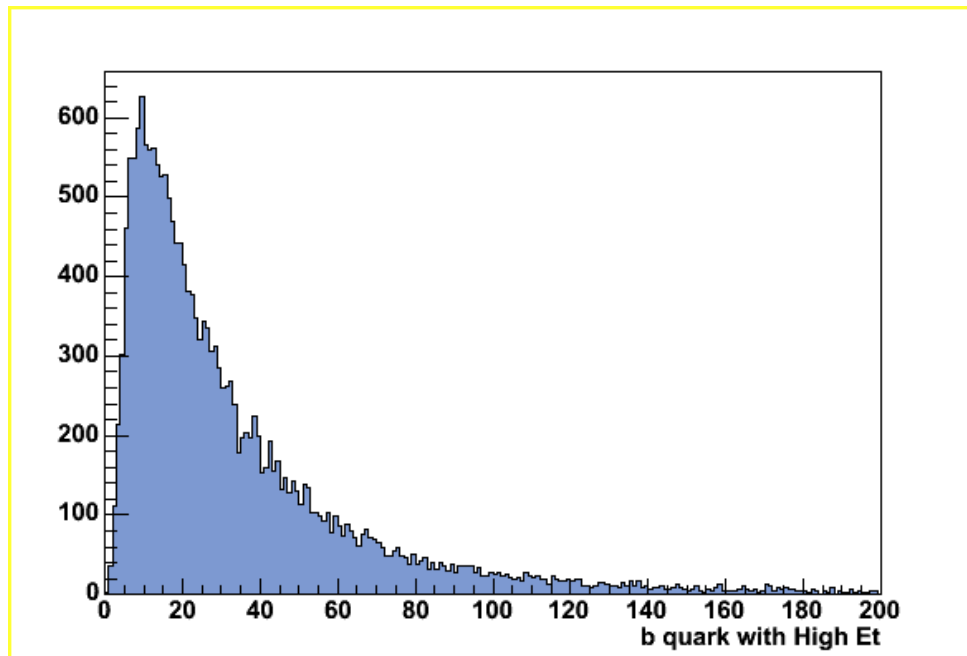
Figure 3.3: E_T distribution of high E_T b-quarks.

High E_T b-quarks have an average energy of 36.7 GeV, whereas low E_T b-quarks have an average energy of 10.9 GeV. The histograms for the other Higgs mass samples have similar shapes with somewhat different values depending on the Higgs mass. The

high and low E_T values are 31.1 GeV and 9.8 GeV for the 140 GeV sample and 39.5 GeV and 11.9 GeV for the 250 GeV sample. It is worth noting that these values are very low compared to the jet E_T values of the other investigated channels, such as the SUSY channels.
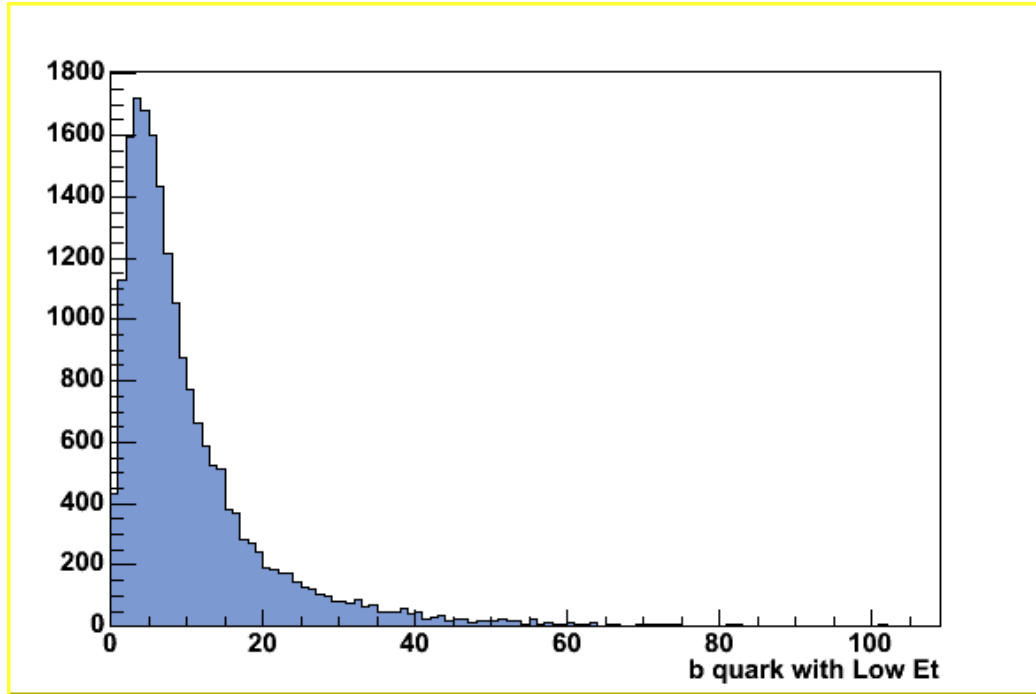
Figure 3.4: E_T distribution of low E_T b-quarks.

As is shown in Figure 3.5 and 3.6, high E_T b-quarks tend to be in the central region ($2 > \eta > -2$), while low E_T b-quarks are mostly located at the forward regions ($2 < |\eta| < 4$). A plot of the high E_T quarks eta (η) versus the low E_T quarks η shows two distinctive localizations are seen (Figure 3.7).
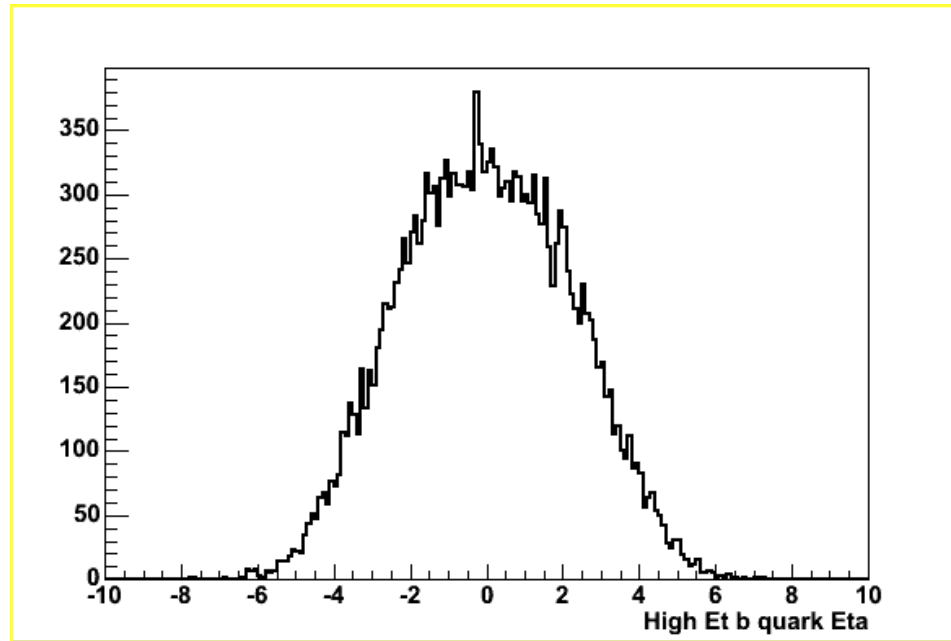
Figure 3.5: η distribution of high E_T b-quarks.
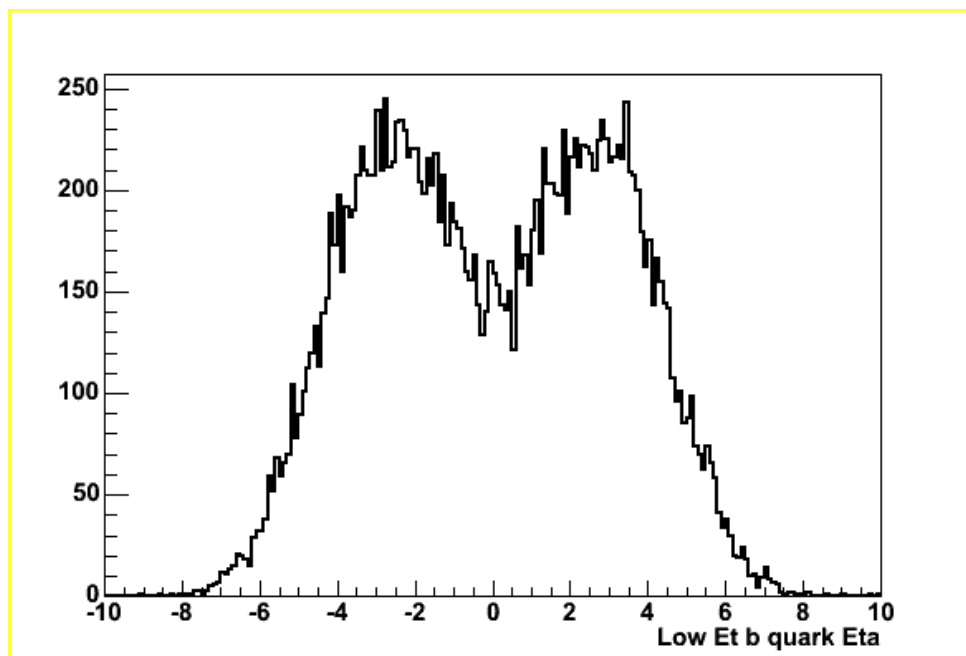
Figure 3.6: η distribution of low E_T b-quarks.
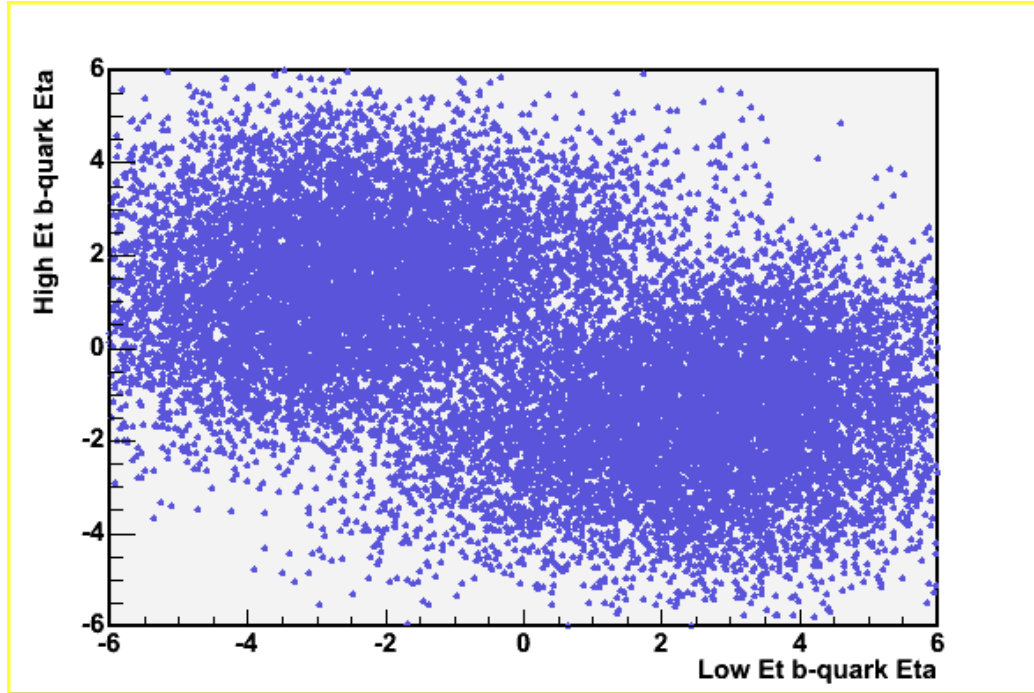
Figure 3.7: High vs low E_T b-quarks η distribution.

3.2.2 b-jets

As stated before, the CMS reconstruction software includes different jet reconstruction algorithms. Among the three principal jet algorithms -the iterative cone, the midpoint cone and the inclusive k_T jet algorithm-, we used cone algorithm jets reconstructed with ΔR $(=[(\Delta\Phi)^2 + (\Delta\eta)^2]^{1/2})) < 0.5$. The simple Cone Algorithm is a trivial cone-based algorithm implemented in the SimpleConeAlgorithm class. The algorithm searches the maximum transverse energy object and constructs a cone around its direction. Any object within this cone will be merged to form a jet. The constituents are then removed from the list of objects, and the procedure is repeated until no objects are left in the list [46]. For a reconstructed jet to be considered a b-jet we required the

separation between the jet and the quark to be less than 0.4 ($\Delta R_{jq} < 0.4$). Splitted ECAL and HCAL towers were taken into account in this process.

When this cut is applied, around 40% of the events have at least one matching jet, but only 12% of the events have two matching jets. The rest do not have any matching b-jet. Figures 3.8 and 3.9 are visualizations of an event obtained using IguanaCMS (a C++ based visualization tool) [53]. The first figure shows the reconstructed jets (as arrows), the beam pipe and the magnet. The second figure displays an event with two matching b-jets that are shown on eta – phi space. High E_T jets can easily be distinguished from low E_T jets.
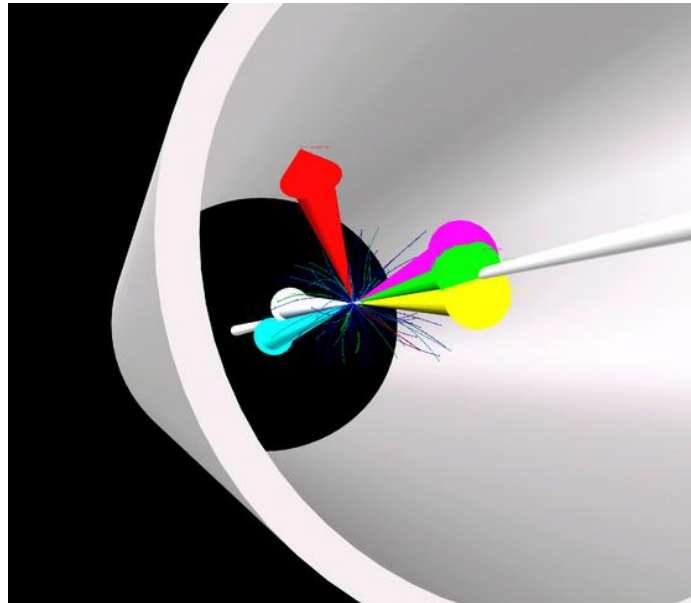
Figure 3.8: An IguanaCMS visualization of the reconstructed jets, beam pipe and the magnet.
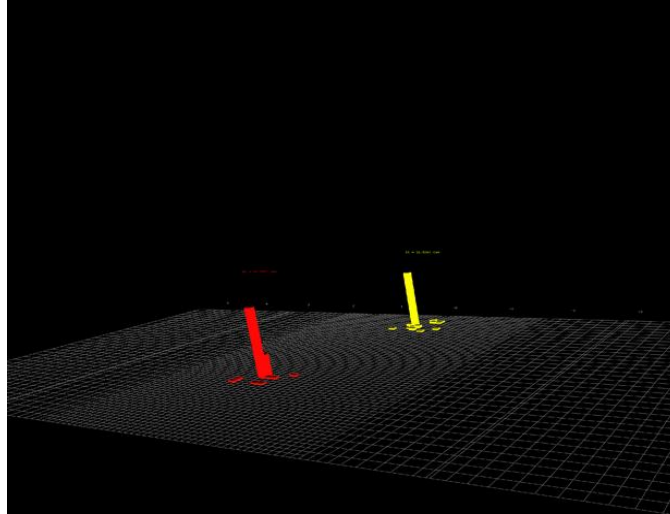
Figure 3.9: An IguanaCMS visualization of two
separate b-jets in the eta-phi plane.

The existence of many non-matching jets can be attributed to the shortcomings of the jet reconstruction algorithms. The jets we are dealing with have low transverse energy and jet reconstruction algorithms are not very efficient in the low E_T region. In Figures 3.10 and 3.11, the E_T distributions are shown for the two matching b-jet cases. The average transverse energy is 49 GeV for the highest E_T jets and 21 GeV for the second highest E_T jets. Again, the plots are for the 200 GeV sample. The other two samples give comparable results. The values are significantly higher than the generated level b-quark information. The possible reason for this is again the lack of sensitivity of the jet algorithms and the calorimeters.
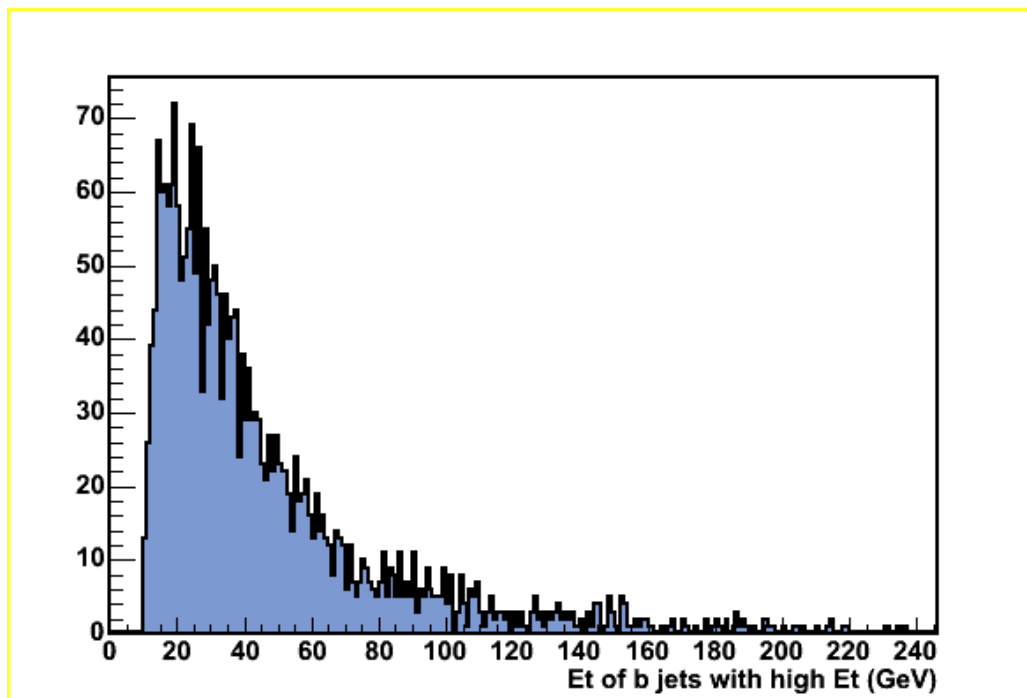
Figure 3.10: E_T distribution of b-jets with high E_T.
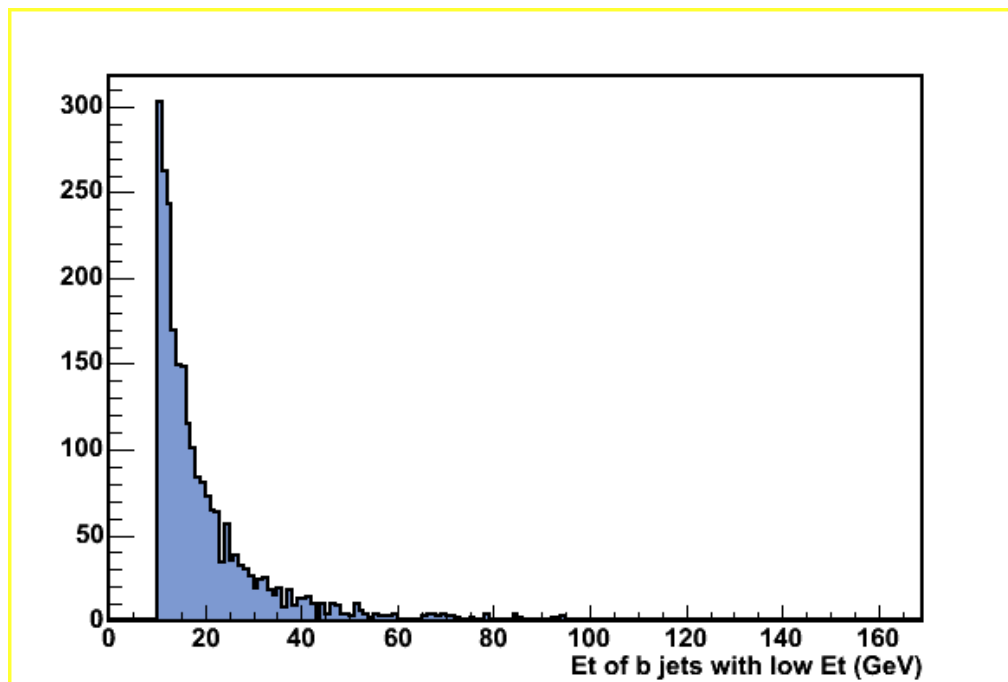
Figure 3.11: E_T distribution of b-jets with low E_T.

Contrary to the η distribution of the generator level jets, the pseudorapidity distributions of the reconstructed jets do not give a very clear picture as it is in generated level information. It is difficult to see the difference between the high and low E_T b-jets (see Figure 3.12). Jets have low transverse momentum and they are mostly central as are the high E_T b-quarks.
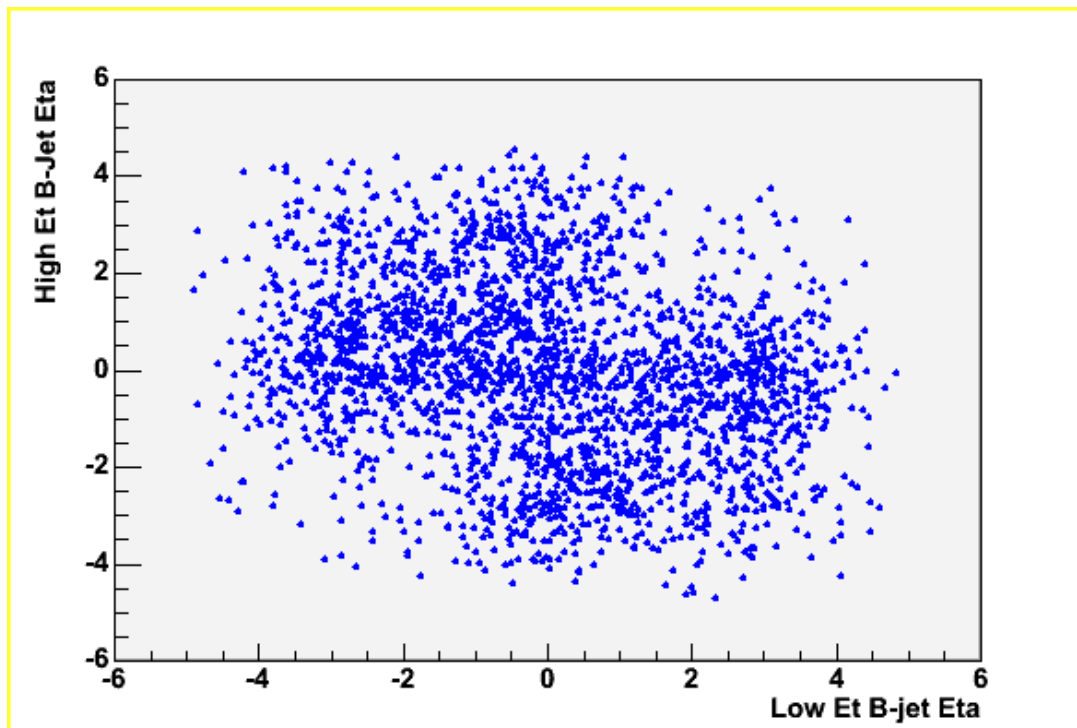
Figure 3.12: High E_T vs low E_T b-jet η distributions.

Comparison of Jet Reconstruction Methods

The three jet reconstruction algorithms, k_T, Recjet5 and Recjet7 are compared using E_T values. The k_T jet algorithm is a cluster based method which successively merges objects which have a distance Rij < R. In the end, Rij is smaller than R for all

final jets [46]. The Recjet5 and Recjet7 algorithms are simple cone algorithms with $\Delta R <$ 5 and $\Delta R < 7$, respectively.

The transverse energy distributions of these three jet algorithms are shown in Figures 3.13, 3.14 and 3.15. The mean E_T values are 17.1 GeV for k_T, 22.2 GeV for Recjet5 and 20.69 GeV for Recjet7. These distributions contain many soft jets due to detector problems. As a result, all these means are smaller than the 32 GeV average of the b-jet E_T distribution obtained from generator level information. The highest mean value is achieved with the Recjet5 algorithm which is widely used by the CMS collaboration.
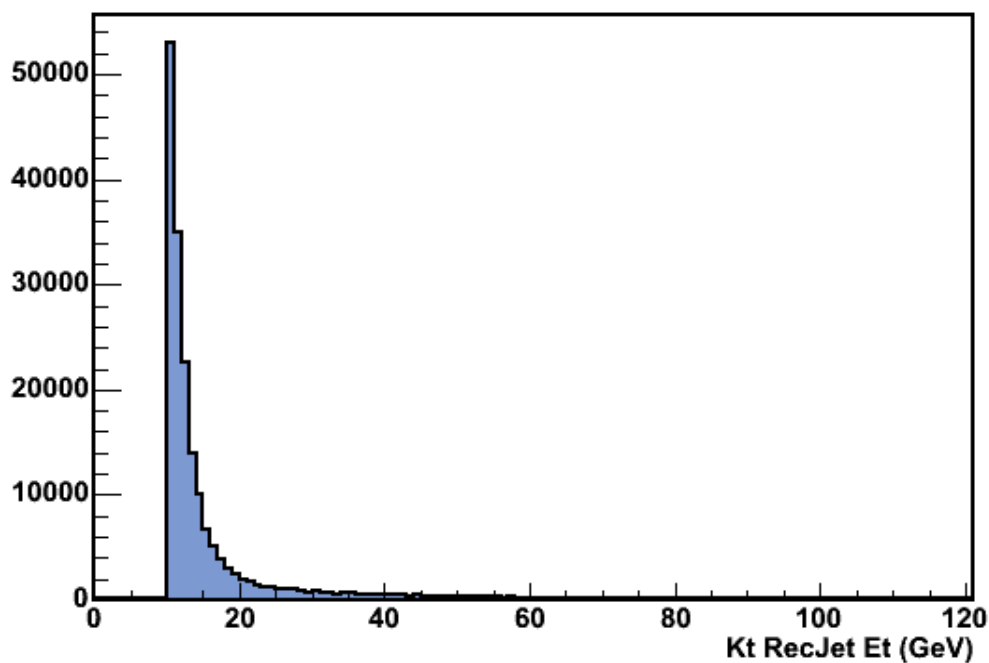
Figure 3.13: E_T distribution for the k_T algorithm.
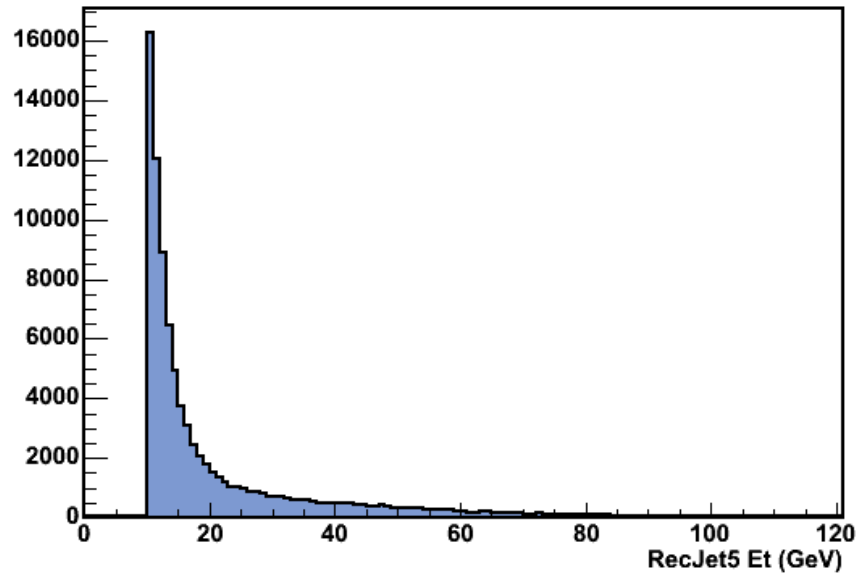
Figure 3.14: E_T distribution for the Recjet5 algorithm.
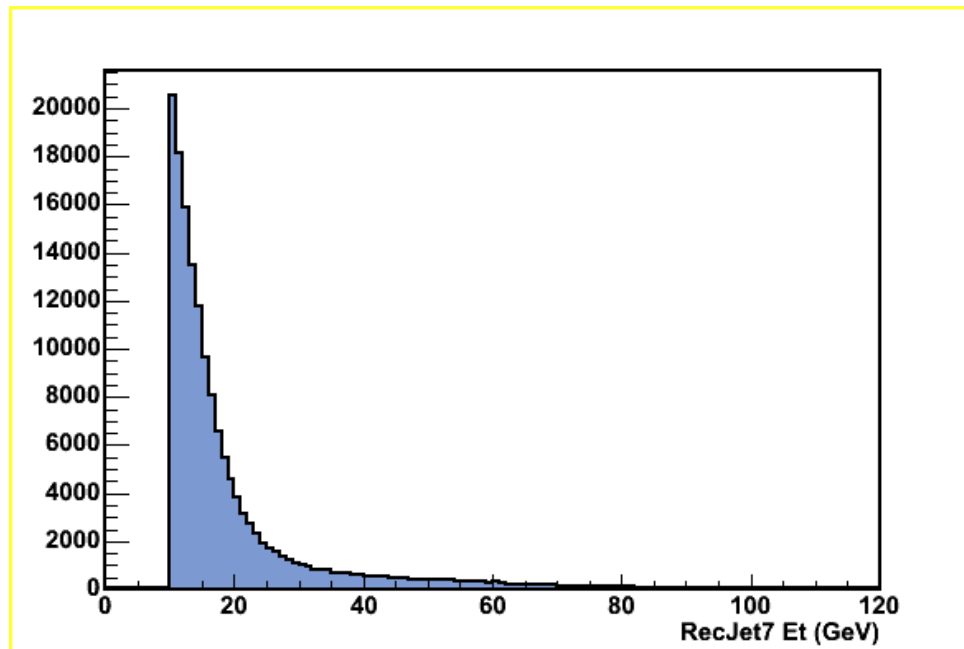
Figure 3.15: E_T distribution for the Recjet7 algorithm.

3.2.3 MET

MET is the crucial element in the determination of the Higgs mass. With the CMS reconstruction software, MET can be obtained using four methods: from Calorimeter Hits (CH), Calorimeter Towers (CT) and from jets, k_T and iterative cone algorithm. The MET distributions obtained by these four methods are shown in Figure 3.16 where the blue area represents the MET from ECAL and HCAL towers, the red lined area the MET from calorimeter hits, the orange area the MET from the IC jets and the green area the MET from the k_T jets.
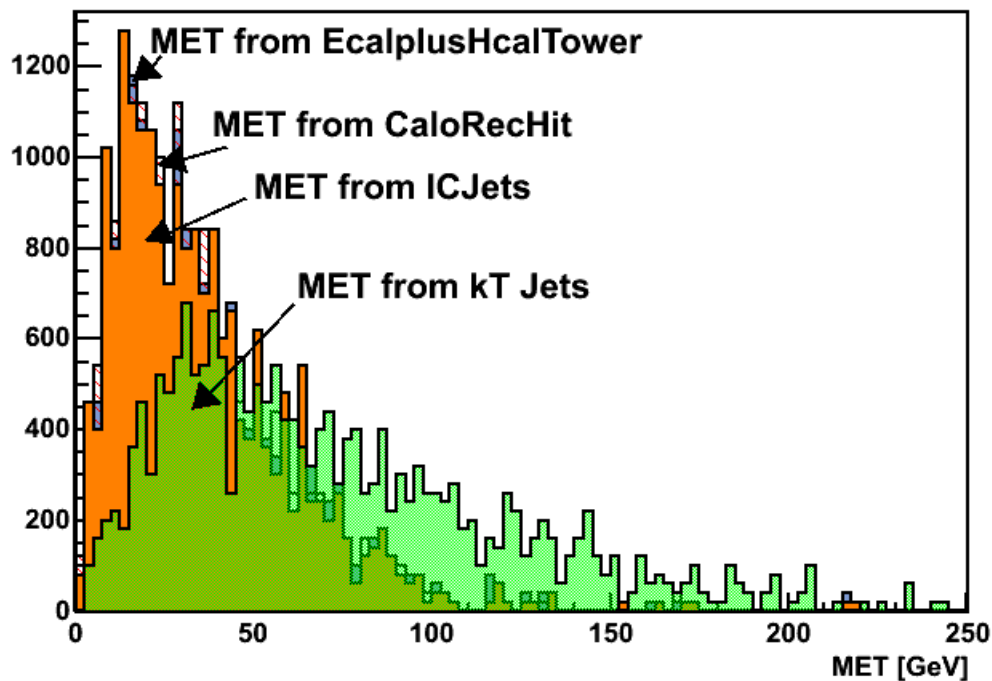
Figure 3.16: MET obtained from the ECAL and HCAL towers (blue), from calorimeter hits (red lined), from IC jets (orange) and from k_T jets (green). The mean values are 35.26 GeV, 35.28 GeV, 35.56 GeV, and 71.71 GeV respectively.

The mean values are very similar to each other (around 35 GeV) except for the 71.71 GeV mean value obtained from the k_T cone algorithm. The first three distributions are localized at mostly small MET values, whereas, the MET from k_T jets has a tail towards high GeV values.

3.2.4 Leptons and Neutrinos in the Final State

To reconstruct the Higgs boson mass, we need to understand the properties of the decay products: leptons and neutrinos. During the event generations τ's are forced to decay into electrons or muons. Since the tracker is not included in simulation, we use generator level information. The fact that the "sister" neutrinos are very close to their "sister" leptons is the most important characteristic of the H b b $\rightarrow$ τ τ $\rightarrow$ l$\nu\nu_\tau$l$\nu\nu_\tau$ channel. The mean of the plot (Figure 3.17) of the angle separation between the lepton and its sister neutrinos at the generator level is 2.2 degrees for the 200 GeV sample. This value is 1.9 degrees for the 140 GeV sample and 1.8 degrees for the 250 GeV sample. The closeness of the leptons and sister neutrinos implies that the direction of the neutrinos, and thus the direction of the MET is known, which allows the reconstruction of the Higgs invariant mass. Figure 3.18 shows the distribution of the cosine of the angle between the two leptons. This important distribution allows the separation of the background channel from the signal.

The E_T distributions of the leptons and neutrinos are shown in Figure 3.19 and 3.20. The mean for the lepton E_T distribution is 44.04 GeV and the mean η value for the leptons is 0.00223. The η distributions show that most of the electrons and muons are in the central region.
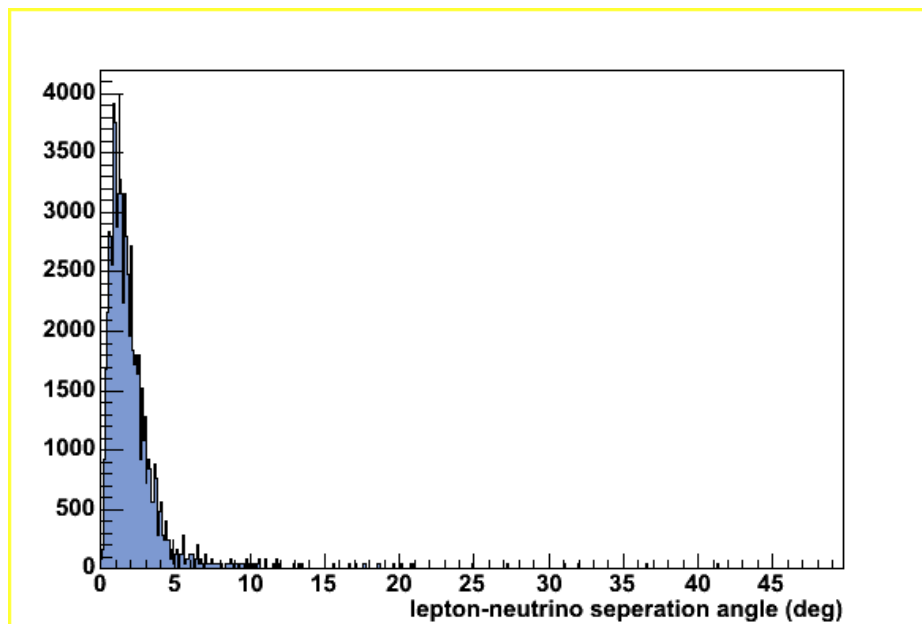
Figure 3.17: The separation angle between the leptons and their sister neutrinos.
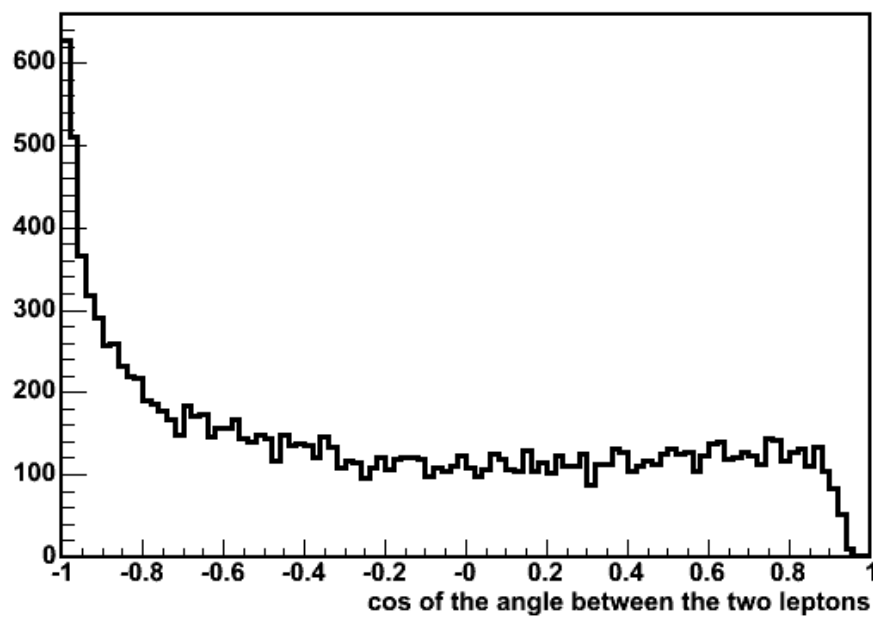
Figure 3.18: The cosine of the angle between the two leptons.
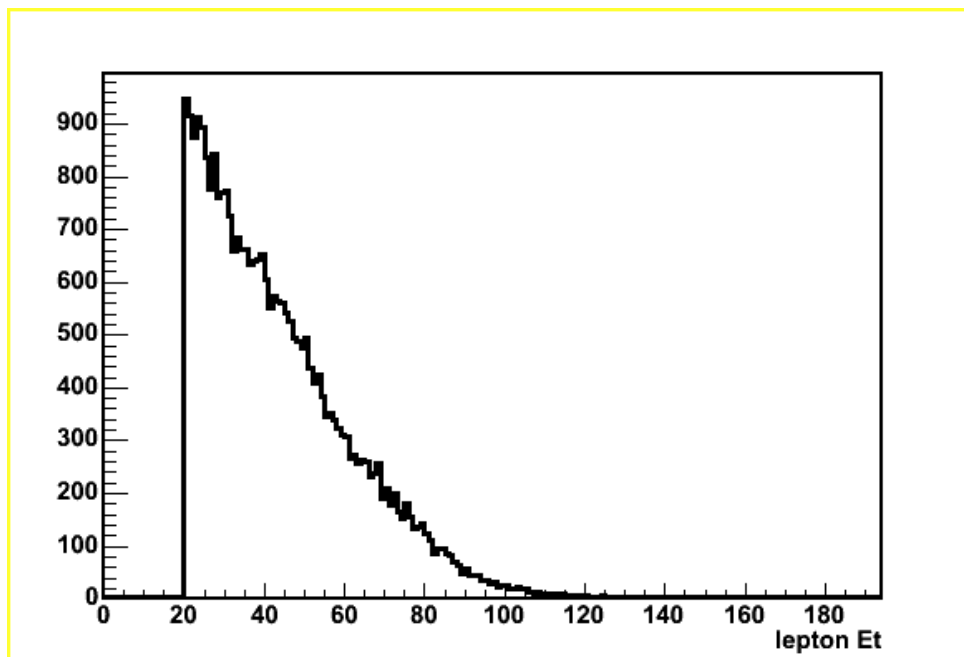
Figure 3.19: E_T distribution of leptons.
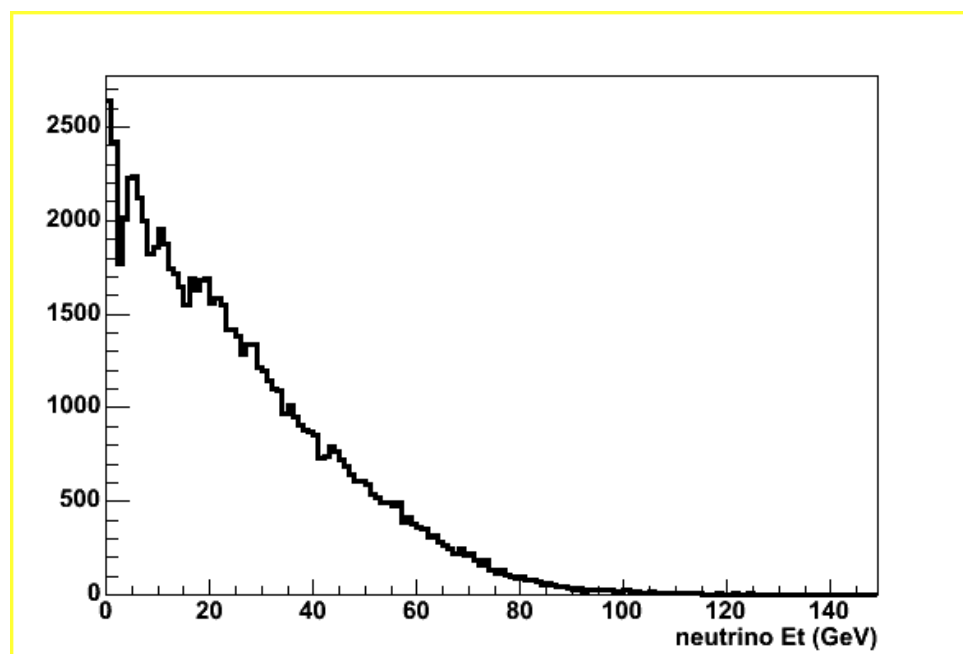
Figure 3.20: E_T distribution of neutrinos.

3.2.5 The Invariant Mass of Tau Pair

The invariant mass of tau pairs, given by $m = \sqrt{(E^2 - p^2)}$, is calculated with generator level lepton and neutrino information. As can be seen in Figure 3.21, the ditau mass gives a sharp peak around 197 GeV which is very close to the m_H value of 200 GeV. However, neutrinos will not be detected directly by the CMS detector. They will escape from the detector where they will be registered as part of the MET. Different methods to obtain MET in the CMS experiment, were explained in section 3.2.3. Figure 3.22 gives the invariant mass distribution when neutrinos are excluded, i.e. the dilepton mass. The mass is much lower than expected.
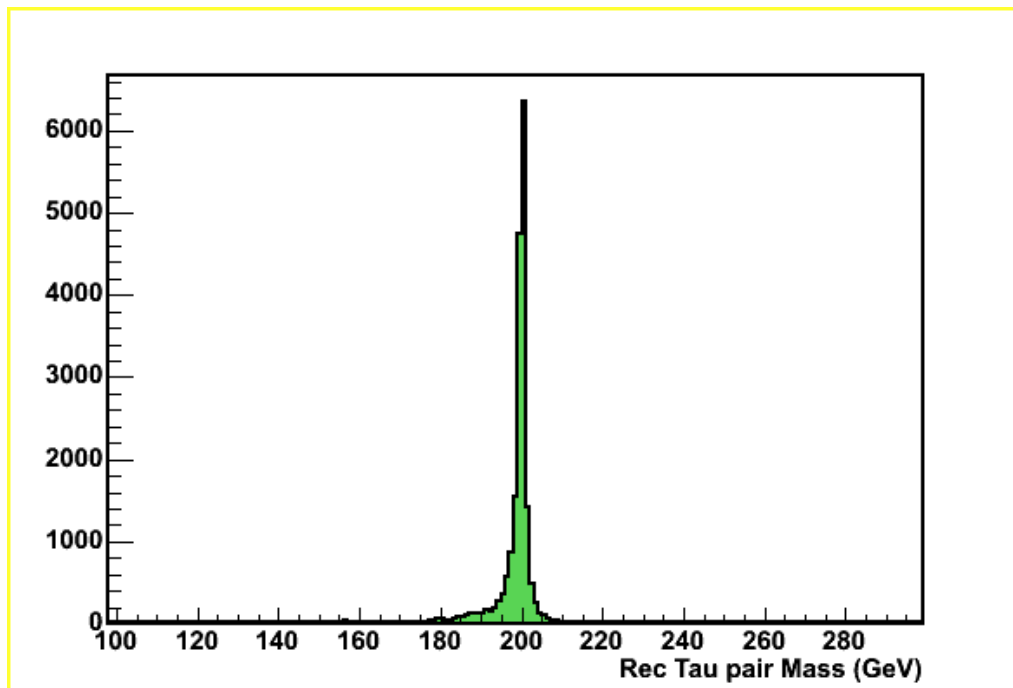
Figure 3.21: Reconstructed dilepton mass obtained using all daughter particles.
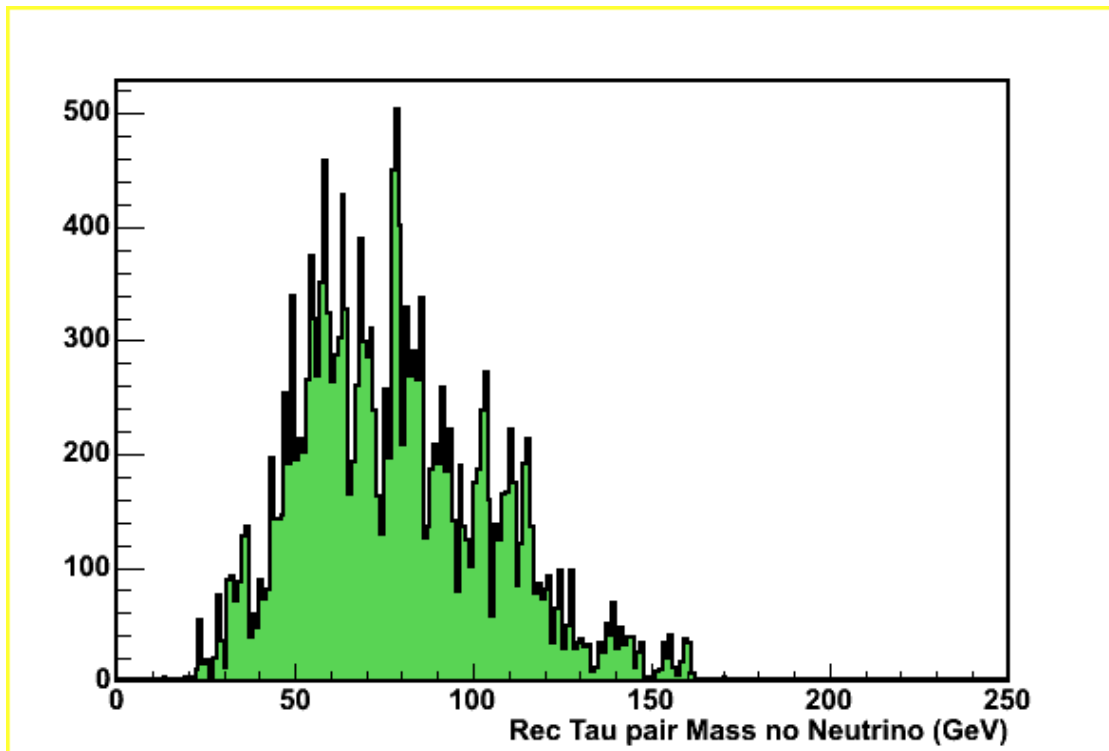
Figure 3.22: Reconstructed dilepton mass obtained using daughter leptons information (no neutrino information).

3.3 Drell-Yan Process as a Background Channel

The main background channels for the H/A → $\tau\,\tau$ decay are the Drell-Yan process (Z, $\gamma^* \to \tau\,\tau$), ttbar production with real and jets faking τ's, and Wt production [43]. For the final state with hadronic τ decay, W + jet events with W→ $\tau\,\upsilon$, QCD multijet production with jets faking τ's are the other backgrounds [40]. For the leptonic and semileptonic modes, Drell-Yan is an important background. For H/A → $\tau\,\tau$ →ll + X there is an additional background of Z, γ^* decaying to electron and muon pairs [43].

We have produced 250,000 Z, $\gamma^* \to \tau\,\tau$ events with mass 80-100 GeV and 25,000 events with mass higher than 100 GeV. The plots for these two data sets have similar

characteristics, so we will discuss the graphs obtained from Z, $\gamma^* \rightarrow \tau \tau$ with $m_Z = 80\text{-}100$. GeV.

The E_T distribution of the reconstructed jets for this background is shown in Figure 3.23. Reconstructed jets are primarily located in the central barrel region of the CMS detector. As in the sample signal, the τ's are allowed to decay to both electrons and muons. The E_T distributions of these daughter leptons and neutrinos can be found in Figures 3.24 and 3.25. According to the η distributions, leptons and neutrinos are mostly in the central region as in the signal case.
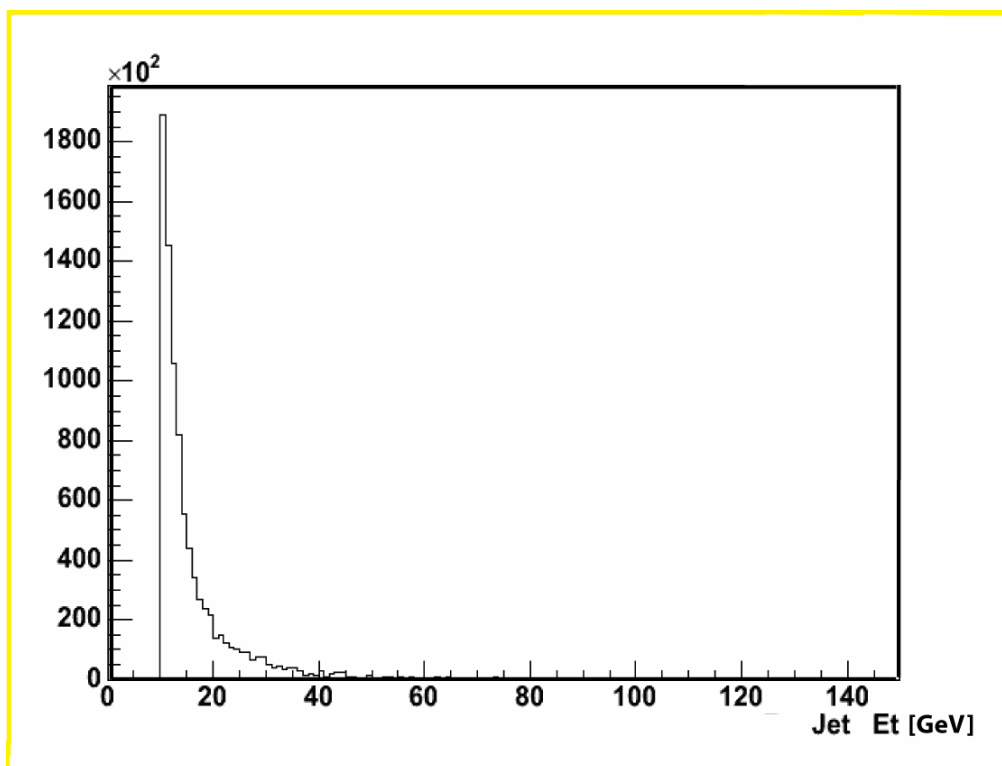
Figure 3.23: E_T distributions for reconstructed jets.
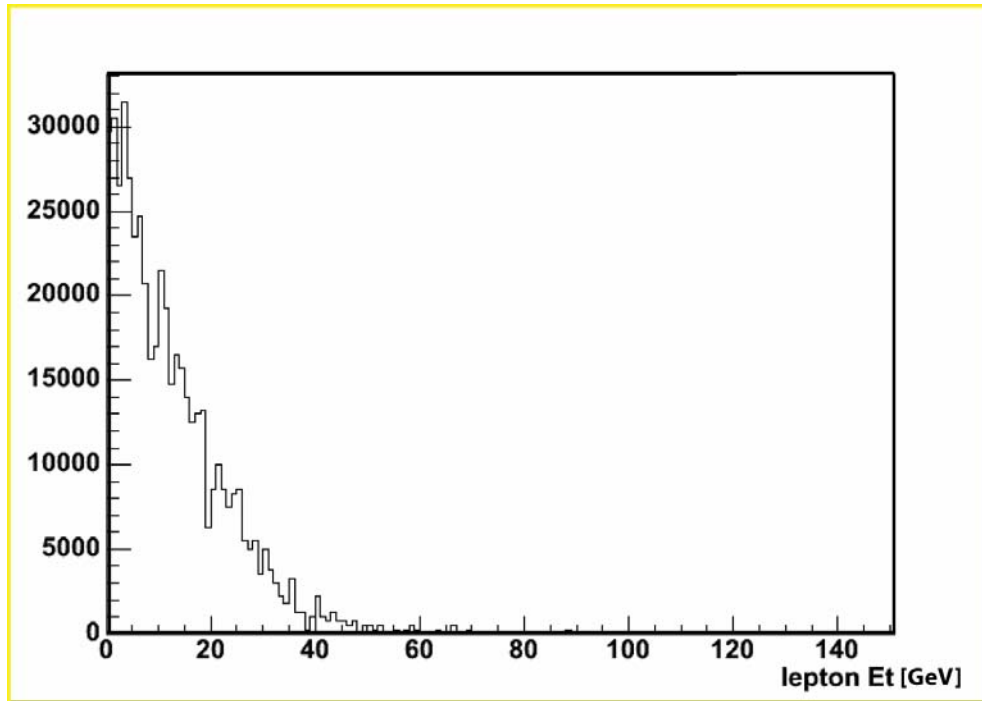
Figure 3.24: E_T distributions for daughter leptons.
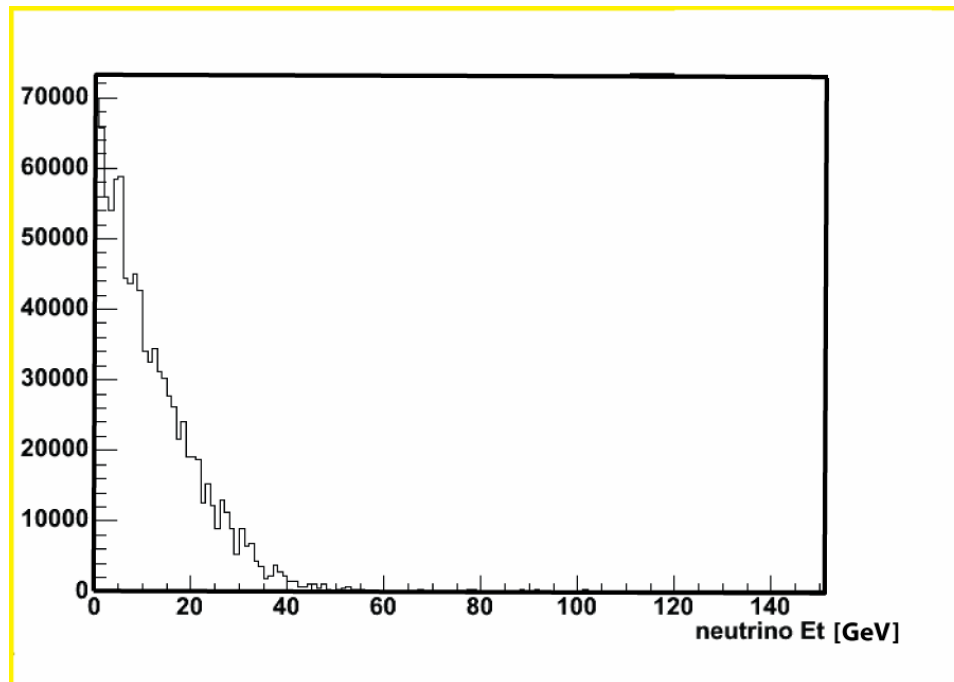
Figure 3.25: E_T distributions for neutrinos.

The ditau invariant mass reconstruction is necessary for a significant reduction of various backgrounds, and can be used as a suppression tool. The τ's are moving relativistically in the laboratory frame due to the large mass and large transverse momentum of the decaying Higgs boson. As a consequence, the τ and observed decay lepton directions are very close to each other. The transverse momentum of the Higgs boson is given by the vector sum of the missing transverse momentum and the transverse momenta of the charged leptons.

The invariant mass is reconstructed both with and without neutrino information. When the neutrinos are included, the invariant mass has a peak around the Z mass (90 GeV) as it is expected. This value is very different than the reconstructed mass for the signal (Figure 3.21) which is equal to Higgs mass. Again, as in the signal case, if the neutrinos are excluded, the invariant mass is reduced dramatically. The distribution becomes very broad and the mean value decreases to 27.28 GeV.

Since we do not have b-jets, unlike in the signal, the Z, $\gamma^* \rightarrow \tau\,\tau$ background can be reduced efficiently with b-tagging. We applied a $P_T > 20$ GeV cut on the daughter leptons which eliminated 94% of the background events. The same cut eliminates only 42% of the signal events. On top of this cut, we applied another cut of $|\eta| < 2.4$, (the tracker coverage region in the CMS). In this way, we increased the eliminated background event percentage to 96.5%, while signal events did not suffer any loss.
Also, the distribution of the cosine of the angle between the two final state leptons plays an important role in distinguishing between the signal and the background. As can be seen in Figure 3.26, the cosine of the angle between the two final leptons has a distribution, which is almost the opposite of the one for the signal (Figure 3.18).
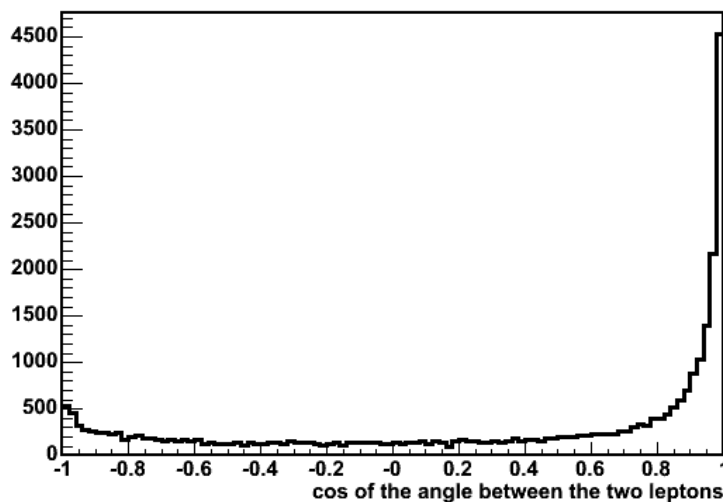
Figure 3.26: Cosine of the angle between the two final state leptons.
As can be seen, this distribution has the opposite shape of the one
for the signal channel.

The number of events remaining for the signal and two backgrounds after the
cuts, is shown in Table 3.2. First the effect of each cuts, then the overall effect of the cuts
is shown.

	Signal (140 GeV)	Back. (100 GeV)	Back. (80-100 GeV)
Initial # of events	5085	68066	1515248
Lepton pt > 20 GeV	2065.8	6854.9	74393
Tau Eta < 2.4	4926	30718.8	638347
Leptons eta < 2.4	4932.2	30760	639821
Cos lep lep > -0.9	4490.9	63158.2	1371979
Cos tau tau > -0.9	4490.1	63087.3	1369450
Final # after all cuts	1780.9	3507.5	37400

Table 3.2: The effect of the cuts on the signal and background. First, the individual
effects of each cut are shown. They are followed by the total result.

3.4 MET and Jet Correction Studies

3.4.1 Muon Correction

The first correction applied to the MET was the subtraction of the muon effect. We know that only a small portion of the muon energy is deposited in the calorimeters, while the remaining part adds to the MET. Thus, the MET has contributions from the muons as well as the neutrinos. In order to extract the energy information of the neutrinos, we subtracted a given amount of energy (3.5 GeV), which is thought to be carried by the muons from the MET every time the muons were in the final state. Then, we applied the jet corrections. The type 1 jet correction is used with different processes which are explained in the next section. In the type 1 correction, only jets, and not towers, are corrected for the reconstruction of the MET [54].

3.4.2 Jet Corrections and Their Effects on MET

Calorimeters are not perfect in reconstructing jets, especially the ones with low energies. Figure 3.27 gives the E_T of reconstructed b-jets versus the E_T of b-quarks. As can be seen in most of the events, matching b-jets have lower energies than their b-quarks. Noise, pile up and deficiencies in reconstruction techniques all contribute to this situation.
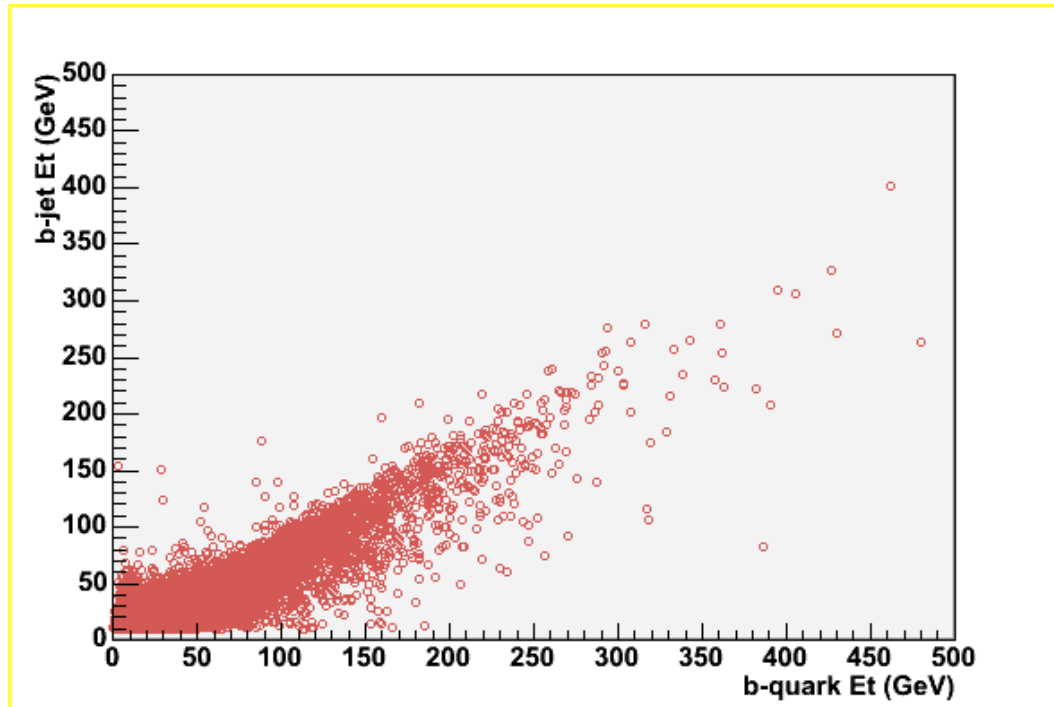
Figure 3.27: The b-jet E_T versus b-quark E_T.

Figure 3.28 shows the ratios of the E_T of b-jets to that of b-quarks as a function of the b-quark η values. It is worth noting that there are two regions –between $\eta = -3$ and $\eta = -1$, and $\eta = 3$ and $\eta = 1$- where the ratios are low. On the other hand, the $\eta = 3$, -3 and 0 regions give high reconstructed jet η values. The two regions at $\eta = 3$ and -3, called horns, correspond to the border of the HE and HF calorimeters. The increases in the ratio are probably due to interface problems of two separate readout systems. Similarly, the HO and HB coexists in the $\eta = 0$ region.
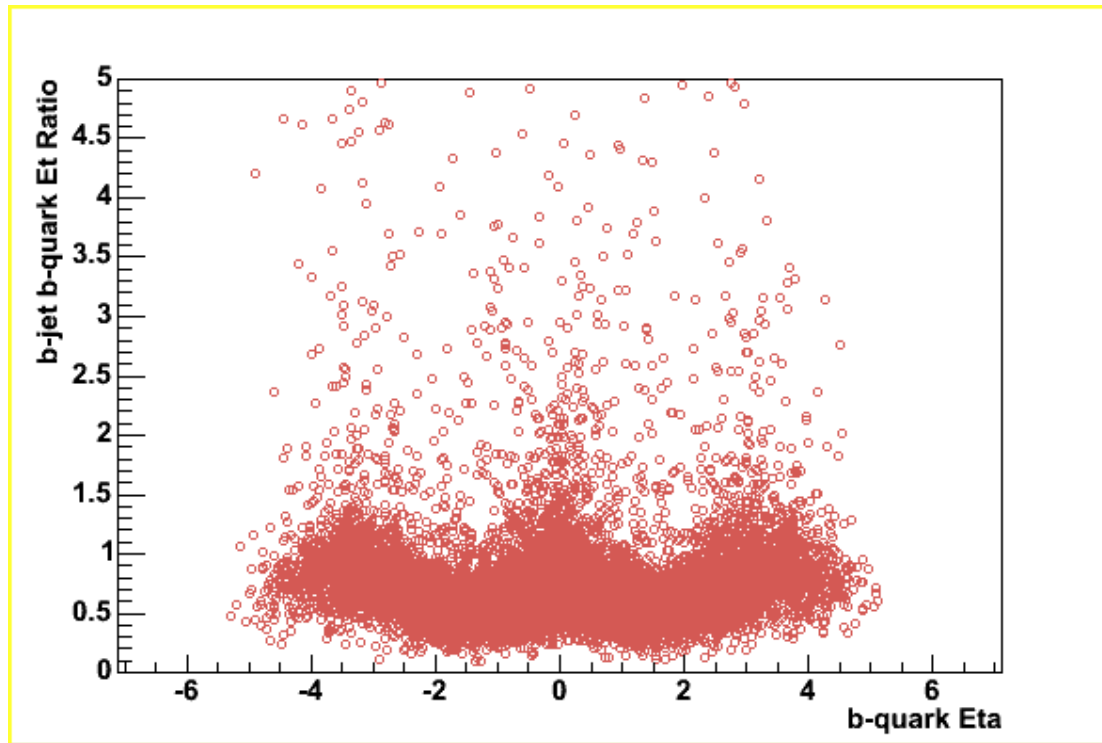
Figure 3.28: The ratio of the b-jet E_T to the b-quark E_T versus the b-quark η. There are some η regions where the ratio is lower than unity, and some others where it is much higher.

In order to obtain the best MET values, we have to work on jet reconstruction and correction methods [54]. Several standard and some "homemade" jet correction techniques are investigated in order to achieve the best MET result. Gamma Jet Correction (GJ), Monte Carlo Jet Correction (MC) and V1 Jet Correction are the three standard procedures used. In the Gamma Jet correction, the jet response is corrected with respect to the ECAL γ response. In the MC Jet corrections, a collection of calorimeter jets (CaloJet) is taken as input and a collection of corrected calorimeter jets is written as output. The correction was derived from measurements of the jet response, CaloJet E_T/GenJet E_T, from all the jets in a QCD sample without pileup. Finally, the V1 jet

correction is an η-dependent E_T correction based on a QCD sample. Figures 3.29, 3.30 and 3.31 show the outcomes of the V1, MC and GJ corrections respectively. In all three of these plots, the red line shows the MET distribution obtained using generator level information, the black line shows for the plain MET value obtained from calorimeter hits, the blue line gives the MET distribution obtained after muon corrections and, finally, the green line shows the MET obtained after jet corrections.
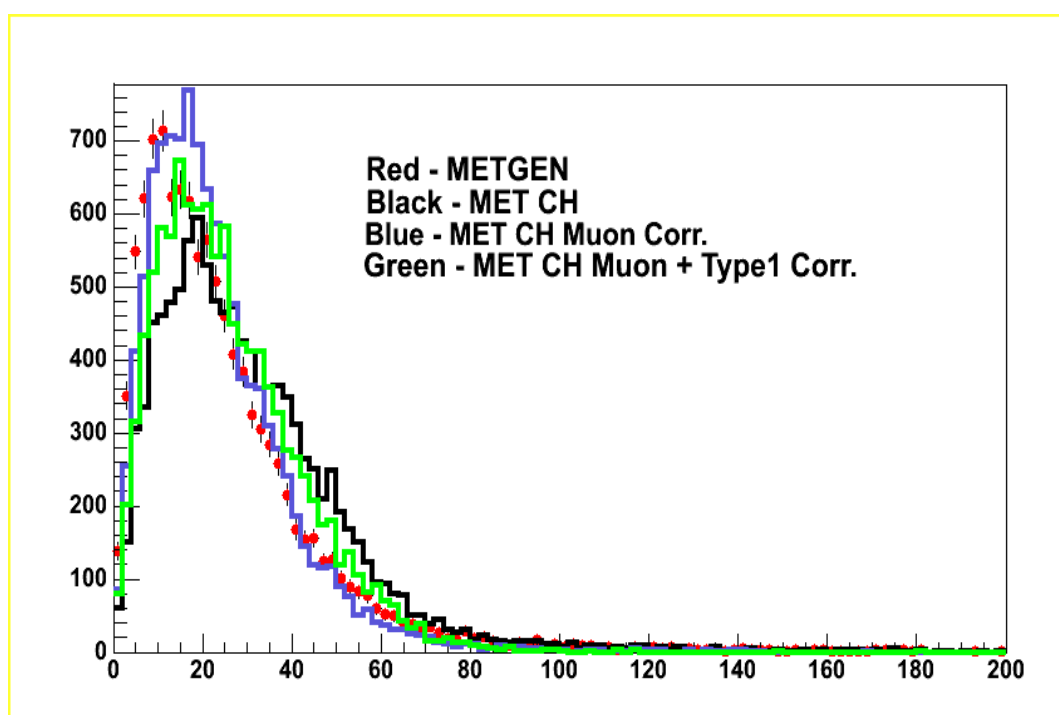
Figure 3.29: The effect of Gamma jet correction on the MET.
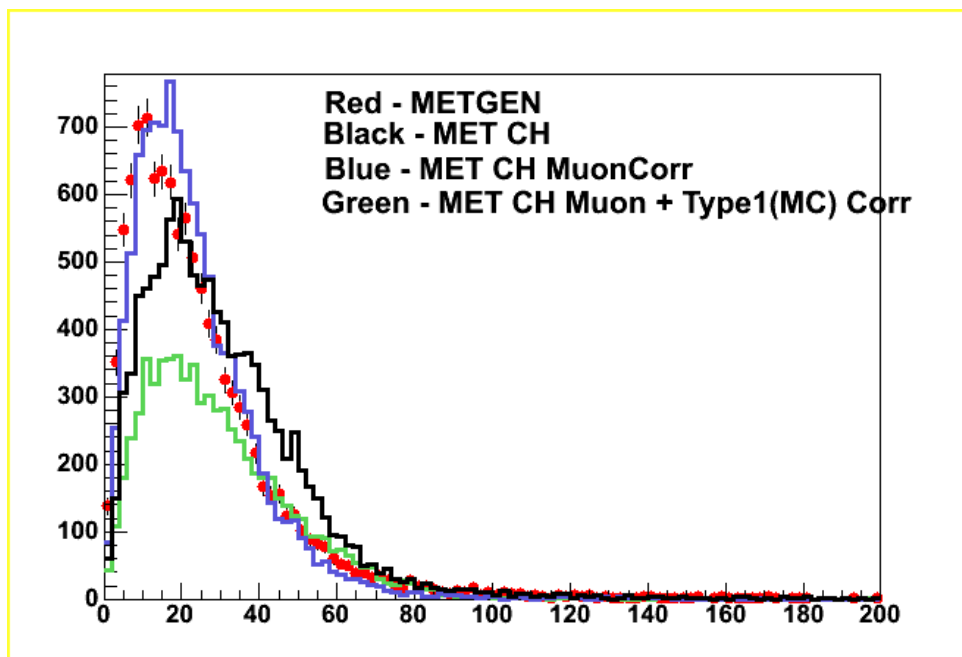
Figure 3.30: The effect of MC correction on the MET.
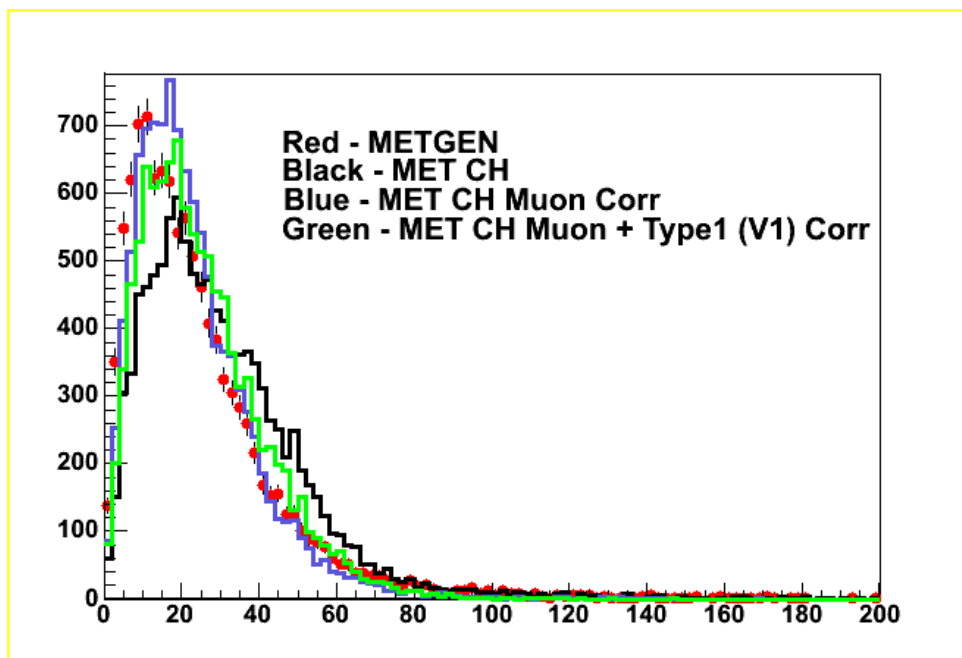
Figure 3.31: The effect of V1 correction on the MET.

<u>3.5 Higgs Boson Invariant Mass Reconstruction</u>

The mass of the Higgs boson can be obtained from the visible τ momenta and the MET using a collinear approximation for the neutrinos from τ decays. The mass resolution depends on the accuracy of the MET measurements and on the angle between the MET and τ leptons [45].

3.5.1 Higgs Mass Reconstruction Methods

Our final goal is to reconstruct the mass of the Higgs using the MET. The formal collinear approximation method [55] reconstructs the mass by using the mass of the final state leptons and the fraction of τ's momentum carried by the neutrinos. The Higgs boson invariant mass can be calculated as:

$$M_H \cong \frac{M_{ll}}{\sqrt{X_1 X_2}},$$

where M_H is the Higgs' mass, M_{ll} is the mass of the final stage dilepton, and X_1 and X_2 are the fractions of the τ's momenta carried by the first and second neutrino pairs, respectively.
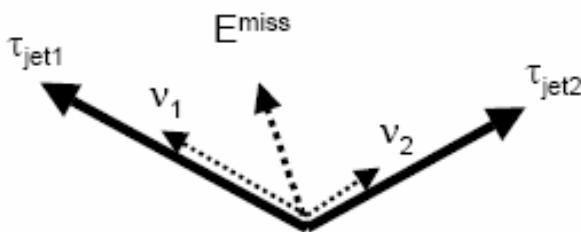
Figure 3.32: Vectors representing the MET, two neutrinos and two τ's.

To use this formula, it is necessary to know X_1 and X_2. The fractions of the two τ momenta which are carried by the neutrinos can be deduced from the momentum parallelogram in the transverse plane.

First, the validity of the collinear approximation is checked with generator level events. When generator level leptons and neutrinos are used the mass can be reconstructed with high precision. Figure 3.33 which shows the result obtained for the 140 GeV sample, has a mean value of 140.1 GeV. This is expected since generator level corresponds to the "ideal" case.
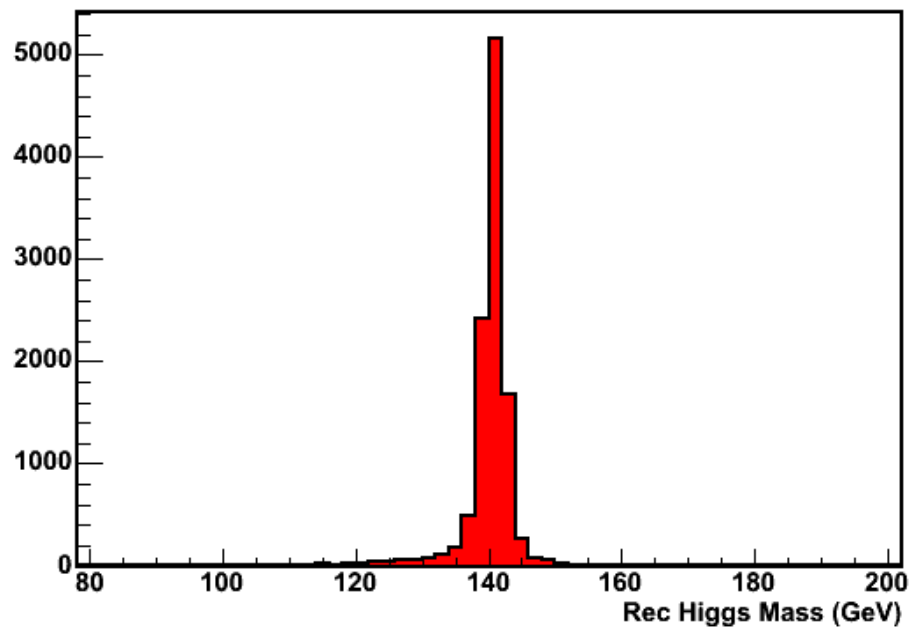
Figure 3.33: The reconstructed Higgs mass obtained by the collinear approximation on generator level particles.

As stated above, the formal collinear approximation requires information of the neutrino momenta, whereas, in real life, the detectors do not yield any neutrino information. However, the MET information can be used to reconstruct the Higgs mass. We applied three different approaches to reconstruct the Higgs mass using the MET information.

Higgs Mass Reconstruction Method 0

In this method, two separate planes are defined: the lepton plane which includes the leptons and missing energy (ME), and the transverse plane where the transverse components of lepton momenta and of MET are located. The cross product of the lepton momenta results in a vector which is perpendicular to lepton plane. The angle between the resultant vector and the transverse plane is defined to be α, which makes the angle between the ME and MET $(90 - \alpha)$. Therefore, the magnitude of ME is given as:

$$| ME | = \frac{| MET |}{\sin \alpha}, \text{ then } (ME)^2 = (MET)^2 + P_{z\,ME}^2$$

ME is a four vector given by:

$$ME = MET_x, MET_y, MET_z = [\sqrt{(ME^2 - MET^2)}], ME$$

The mass of Higgs boson is given by $m^2 = E^2 - P^2$:

$$M_H^2 = (ME + E_{lepton1} + E_{lepton2})^2 - (P_{x\,lepton1} + P_{x\,lepton2} + ME_x)^2$$
$$- (P_{y\,lepton1} + P_{y\,lepton2} + ME_y)^2 - (P_{z\,lepton1} + P_{z\,lepton2} + ME_z)^2$$

Figure 3.34 shows the distribution of the Higgs mass reconstructed with Method 0, using the E_T from calorimeter hits for the 140 GeV sample. Although the distribution is narrow enough, the peak value is around 100 GeV, which is much less than the actual

Higgs mass. The reconstructed mass obtained from the MET from the calorimeter towers yields an even smaller mean value.
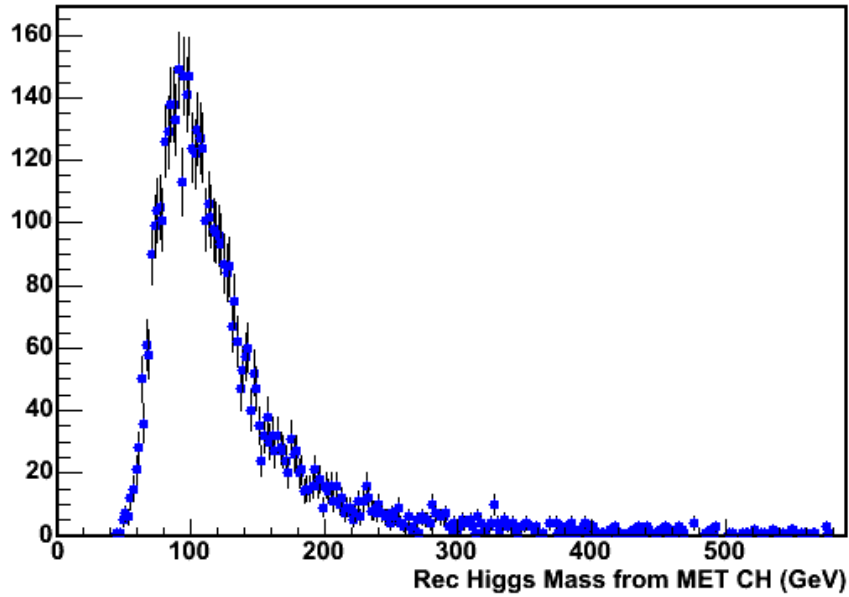
Figure 3.34: The reconstructed Higgs mass obtained using
Method 0 after the cuts have been applied.

Higgs Mass Reconstruction Method 1

After obtaining a poor efficiency with Method 0, we focused on different approaches. In the "Method 1" approach, the components of the MET in the direction of the leptons are calculated in the transverse plane. Then, it is assumed that the same ratio will be valid for the z-components. We start by finding the angle between the transverse components of the leptons and the MET. We require the MET to be between two leptons.

The components of the MET along the direction of the two leptons are given by:

$$MET_{l1} = MET \times \frac{\sin(\Theta_{(P_{T\,lepton1}-MET)})}{\sin(\Theta_{(P_{T\,lepton1}-P_{T\,lepton2})})}$$

$$MET_{l2} = MET \times \frac{\sin(\Theta_{(P_{T lepton2} - MET)})}{\sin(\Theta_{(P_{T lepton1} - P_{T lepton2})})}$$

The two neutrinos (υ_{12}) are assumed to be one single particle. The x, y and z components are calculated from:

$$P_{x \upsilon_{12}} = (\frac{P_{x lepton1}}{P_{T lepton1}}) \times MET_{l1}$$

$$P_{y \upsilon_{12}} = (\frac{P_{y lepton1}}{P_{T lepton1}}) \times MET_{l1}$$

$$P_{z \upsilon_{12}} = (\frac{P_{z lepton1}}{P_{T lepton1}}) \times MET_{l1}$$

The same procedure is applied for the other two neutrinos, υ_{34}.

Next the mass is reconstructed by using the energy and momentum information of two leptons and two neutrinos.

$$M_H = M_{\upsilon_{12}} + M_{\upsilon_{34}} + M_{lepton1} + M_{lepton2}$$

Figure 3.35 shows the reconstructed Higgs mass with Method 1 by using the MET from calorimeter hits. It yields a mean value close to the generated Higgs mass, but the tail in the high mass region shows imperfections in this technique.

Higgs Mass Reconstruction Method 2

Although Method 1 gives better mean values, the shape of the resultant mass distribution is of concern. To reduce the tail, we used Method 2.

In the Method 2 approach, all the MET is added to one of the leptons in the transverse plane. Then, the cross product with the other lepton is taken. It is assumed that

the ratio of the cross products before and after the MET addition is equivalent to X_1 and X_2.

X_1 and X_2 can be found as:

$$X_1 = \frac{P_{x\,lepton1} \times P_{y\,lepton2} - P_{y\,lepton1} \times P_{x\,lepton2}}{P_{y\,lepton2} \times (P_{x\,lepton1} + MET_x) - P_{x\,lepton2} \times (P_{y\,lepton1} + MET_y)}$$

$$X_2 = \frac{P_{x\,lepton1} \times P_{y\,lepton2} - P_{y\,lepton1} \times P_{x\,lepton2}}{P_{x\,lepton1} \times (P_{y\,lepton2} + MET_y) - P_{y\,lepton1} \times (P_{x\,lepton2} + MET_x)}$$

The result obtained by Method 2 is shown in Figure 3.36.
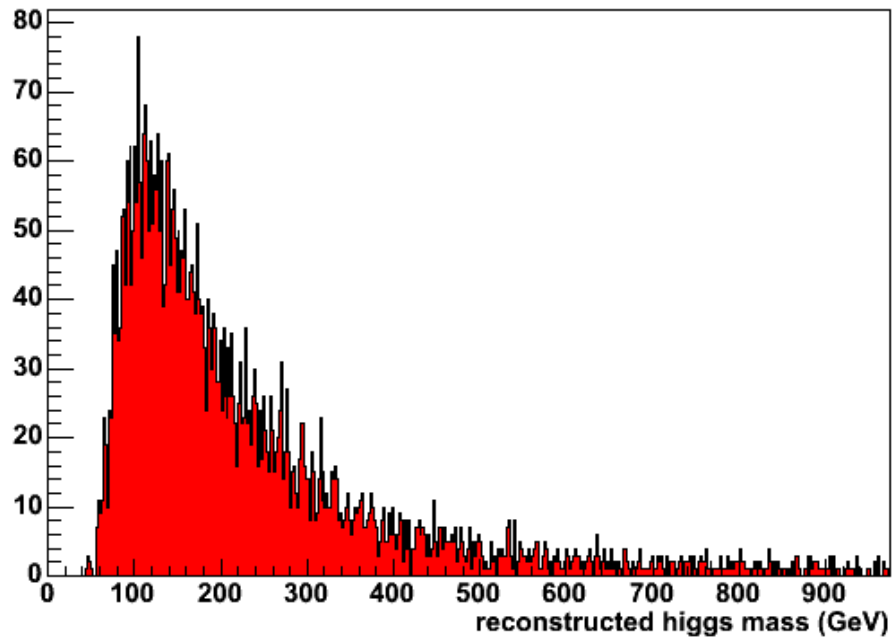
Figure 3.35: The reconstructed Higgs mass obtained using Method 1.
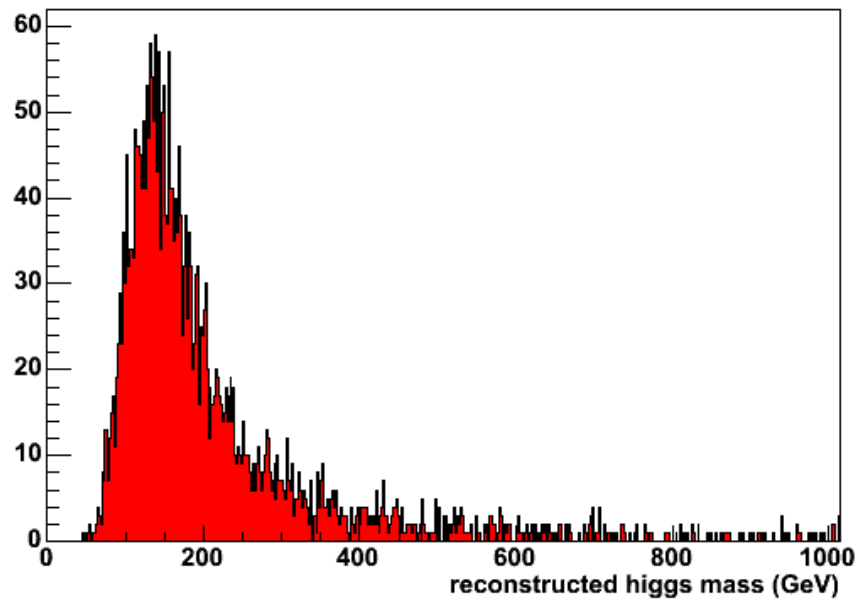
Figure 3.36: The reconstructed Higgs mass obtained using Method 2.

It is worth noting that, these kinds of reconstructions are possible if and only if the τ's are not emitted back to back in the transverse plane. Therefore, it is necessary to impose the cut cosΦ>0.9 [56].

Figure 3.37 was created to compare the Method 1 and 2 approaches. Since Method 1 and 2 give much better results than Method 0, only these two methods are considered here on out. Here, the generator level lepton masses and MET are used to reconstruct the Higgs mass. The yellow area represents Method 1 and the blue thick line represents Method 2. The Method 1 collinear approximation has a tail in the mass distribution, but yields almost two times more events than Method 2 for both the signal and the background. The Method 2 collinear approximation yields a slightly sharper mass signal. Both of the methods give results close to the desired mass.

The two distributions are similar since the generator level information is used for this plot. However, after the cuts, Method 2 gives a sharper profile, because it has extra cuts.
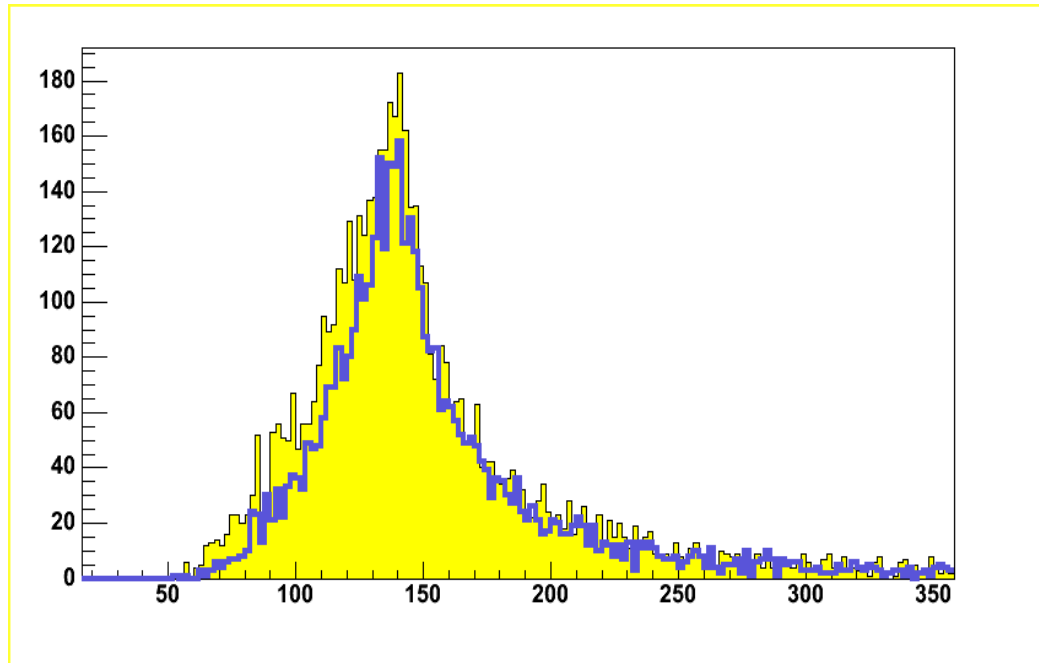
Figure 3.37: The Higgs mass reconstructed using the collinear approximation using the generated MET and generated lepton information. The yellow area is obtained from Method 1, and the blue line shows the result of Method 2.

3.5.2 Effect of JetMET Corrections on Higgs Mass Reconstruction

As the next step, we tried to improve the mass reconstruction by adding jet corrections to Methods 1 and 2. The results of the Method 1 mass reconstruction are shown in Figures 3.38 (for V1), 3.39 (for MC) and 3.40 (for GJ). In all of these plots, the yellow area shows the distribution obtained by the generator level information. The black, blue and green lines are for the MET obtained from calorimeter hits (CH), the

MET obtained after muon corrections, and the MET obtained after muon plus jet corrections respectively.
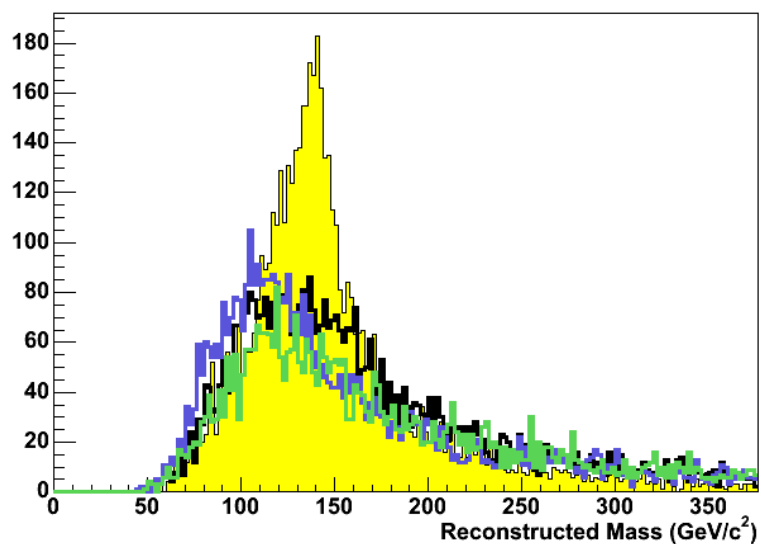
Figure 3.38: Reconstructed Higgs mass with Method 1 and the V1 jet correction.
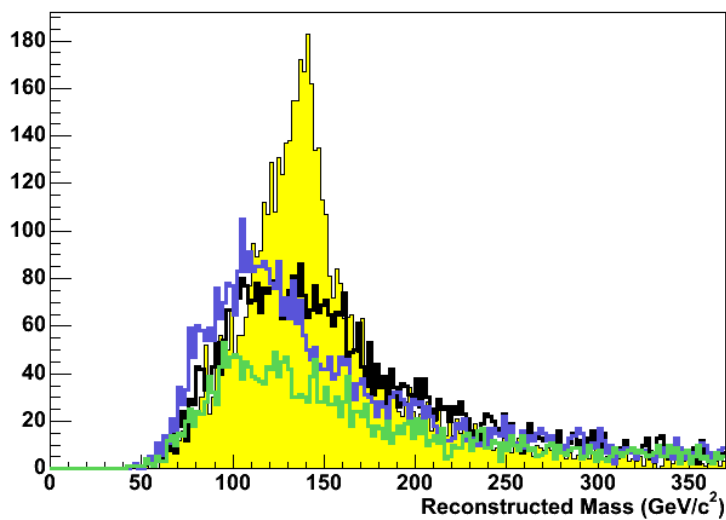
Figure 3.39: Reconstructed Higgs mass with Method 1 and the MC jet correction.
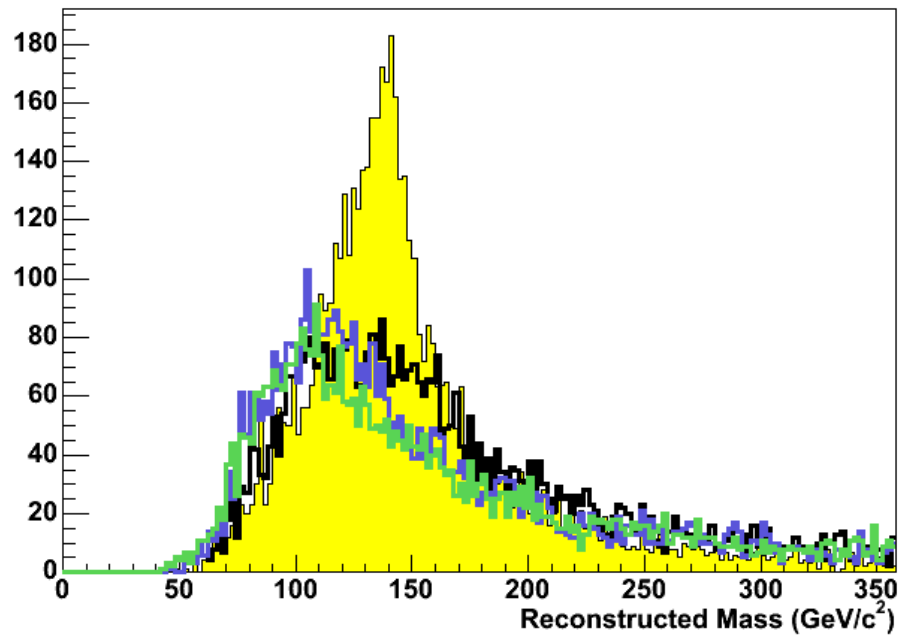
Figure 3.40: Reconstructed Higgs mass with Method 1 and the
Gamma jet Correction.

Finally, Figures 3.41, 3.42 and 3.43 display the Method 2 mass reconstruction results. The colors on these plots represent the same MET types as the ones in the previous three plots. As can be seen, the V1 corrections give slightly better results. However, none of the corrections yield close results to the generator level missing transverse energy. In the case of the Method 1 mass reconstruction, the jet correction methods lead to a shift in the peak in the wrong direction.
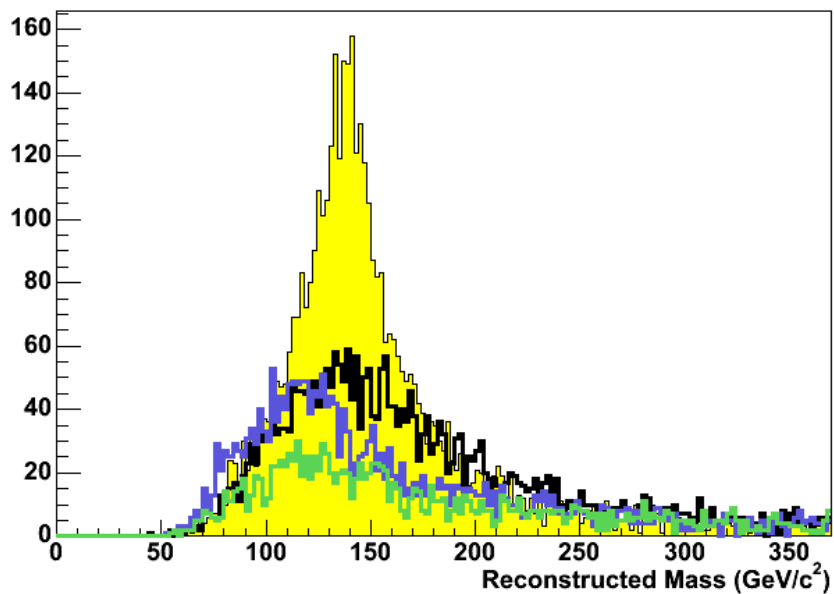
Figure 3.41 Reconstructed Higgs mass with Method 2 and the V1 jet Correction.
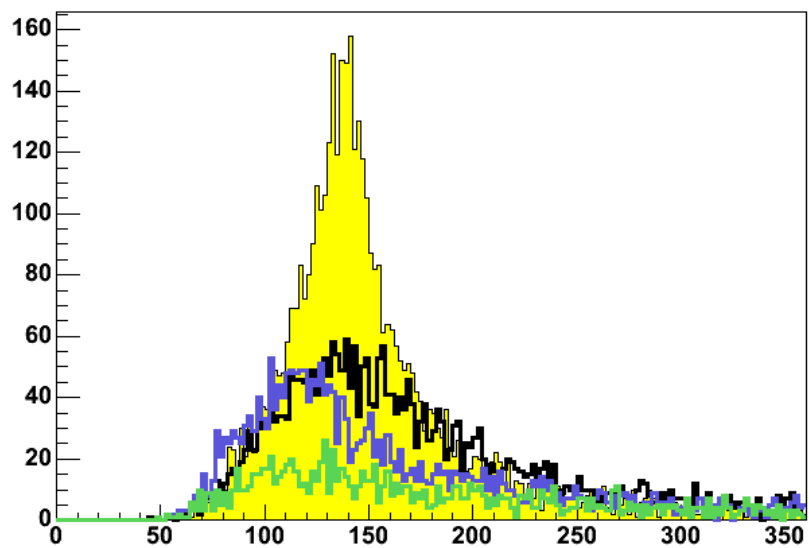
Figure 3.42: Reconstructed Higgs mass with Method 2 and the MC jet correction.
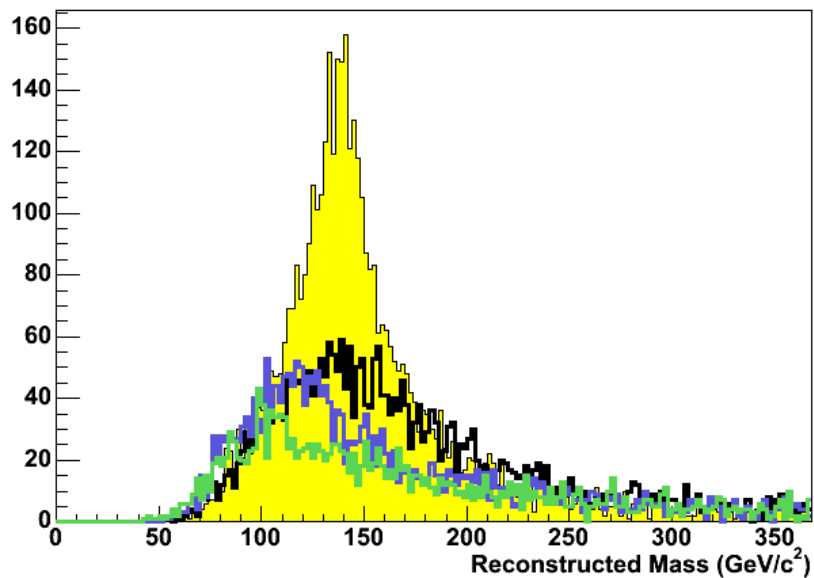
Figure 3.43: Reconstructed Higgs mass with Method 2 and the Gamma jet correction.

We deduce that standard CMS jet correction methods do not improve the mass resolution. We created jet corrections specific to the signal channel by comparing the generated jet E_T's to the reconstructed jet E_T's in small η regions. Plots of the ratio of the recjet E_T to genjet E_T versus P_T of the genjets show that for low P_T jets the reconstruction efficiency is very low. The ratio tends towards unity for high E_T jets. However, with the low statistics from DC04 sample it is not possible to obtain significant improvement on the MET distributions. To overcome the low statistics limitation, we used the jet correction values deduced from the same approach by using qqH $\rightarrow$ W^+W^- leptonic decay which has higher statistics. However, neither of these decays yielded a drastic improvement on the mass reconstruction (see Figure 3.44).
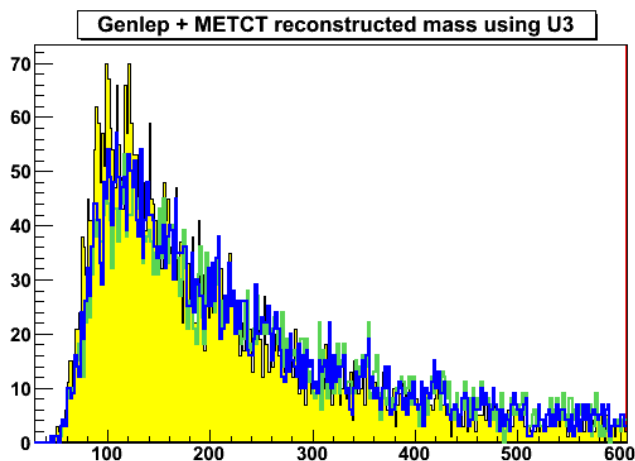
Figure 3.44: The reconstructed Higgs mass. Yellow – before,
blue - WW jet correction, green - τ+τ- jet correction.

Finally, the Higgs boson mass distributions obtained from the background and the signal are displayed in Figure 3.45. Method 1 approach is used to reconstruct the mass. As it is expected, the reconstructed Higgs mass of the signal peaks at around 140 GeV and the mass of the background at around 90 GeV.
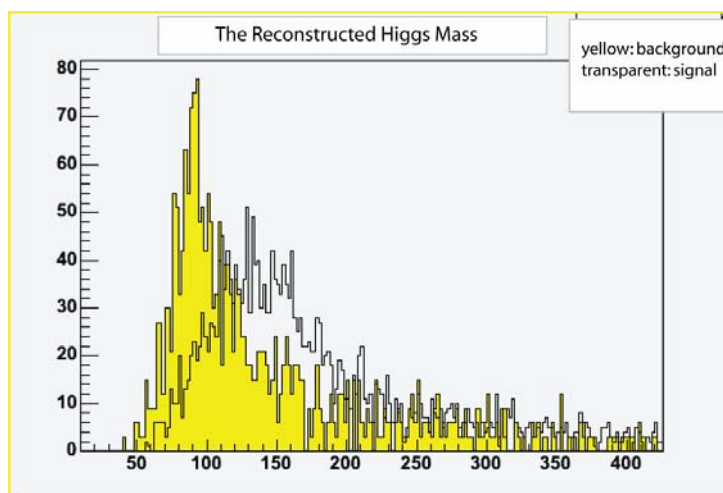
Figure 3.45: The reconstructed Higgs mass for the signal (transparent)
and the Drell-Yan background (yellow). The peak for the background
is at around 90 GeV and for the signal is at around 140 GeV, as expected.

3.6 Conclusion

The b b H → ττ channel is a very important towards understanding the MSSM. The main characteristics of the channel are the known neutrino directions. With these distinct kinematics it serves as a benchmark for tuning our reconstruction tools, as well.

We demonstrated two different approaches of invariant mass reconstruction using the collinear approximation. The missing transverse energy for this channel is very low, and in order to reconstruct the Higgs mass efficiently, it is important to improve the MET using adequate jet reconstruction algorithms. The methods known and used thus far do not work efficiently, and standard CMS jet correction methods do not give satisfying answers, though some of them go a short way towards improving the mass reconstruction. With the V1 jet correction method, it is possible to achieve slightly better distributions. However, some of the algorithms shift the mass peak in the wrong direction. It is important to realize the "error" in the reconstruction and find methods which work better. This study has been performed on 140 GeV, 200 GeV and 250 GeV samples from the DC04 using ExRoot. All of the samples yielded similar results.

Finally, when the reconstructed Higgs mass obtained from Method 1 approach for the signal and Zγ* 80-100 GeV background channel are compared, it is seen that the peak for the background is much smaller since it corresponds to the Z mass rather than 2 τ masses.

CHAPTER IV

INVESTIGATION OF THE SM HIGGS PAIR PRODUCTION AT THE

LHC

4.1 Standard Model

The Standard model (SM) of particle physics is a fundamental theory of particles and their interactions based on symmetry principles, in particular local gauge symmetries [40, 57]. It contains only a limited set of elementary particles. According to the SM, the spin ½ particles, called fermions, are the constituents of the matter in the Universe. Fermions consist of six types of leptons and six types of quarks. These elementary particles interact through fields. The four fundamental forces are the electromagnetic, weak, strong and gravitational force. The spin 1 (with the exception of the graviton which has spin 2) particles associated with these forces are called gauge bosons. Table 4.1 provides a summary of the elementary particles. The only other boson not included in this table is the Higgs boson, yet to be observed experimentally.

Table 4.1: Elementary particles: Leptons, quarks and force carriers.

The SM is a Lagrangian field theory [58] where the fermions can be described by the Dirac Lagrangian:

$$L = \bar{\Psi} i \gamma_\mu \partial^\mu \Psi - m \bar{\Psi} \Psi,$$

where Ψ is a 4-component complex field, which represents a free fermion field with mass m.

The Higgs boson Lagrangian is based on the Klein-Gordon Lagrangian:

$$L = \partial_\mu \phi^* \partial^\mu \phi - m^2 \phi^+ \phi,$$

where Φ is a complex scalar field with mass m [59].

The gauge boson Lagrangian, for example for the physical photon field A^μ is given by:

$$L = \bar{\Psi}(i\gamma^\mu \partial_\mu - m)\Psi + e \bar{\Psi} \gamma^\mu A_\mu \Psi - \frac{1}{4} F_{\mu\nu} F^{\mu\nu},$$

where $F_{\mu\nu} = \partial_\mu A_\nu - \partial_\nu A_\mu$ is the antisymmetric tensor of the gauge boson field [60].

Interaction between charged particles is mediated by the gauge bosons which appear in the Lagrangian through "interaction terms" like:

$$L_{int} = -e \bar{\Psi} \gamma^\mu Q \Psi A_\mu,$$

where Q is the charge operator (with eigenvalue -1 for the electron) [60].

In the SM, local gauge symmetries control the particle interactions. The SM combines the electroweak theory [61, 62] with the standard model of the fundamental strong force. The complete gauge group of the SM is given by $SU(3)_c$ x $SU(2)_L$ x $U(1)_Y$ [40].

The SM is a very successful theory. Predictions of the SM are consistent with numerous measurements performed thus far, and all the predicted particles, except for the Higgs boson, have been discovered in experiments [63, 64]. The mass ratio of W and Z

bosons (M_W/M_Z) as measured by the CERN experiments is in very good agreement with the predictions of the minimal Electroweak Model which introduces a single Higgs doublet corresponding to four scalar fields. Three of these four scalar fields are incorporated in W and Z boson masses. After the discovery of the $W^{\pm}$ and Z^0 bosons, the only missing element of the Standard Electroweak Model is the Higgs boson [58].

4.1.1 Electroweak Symmetry Breaking

One feature of the Standard Model is that the W and Z bosons have large masses, whereas the photon is massless. In order to allow the massive bosons and fermions observed in nature, the electroweak symmetry must be broken so that all successful symmetry predictions are still valid. This is done by spontaneous symmetry breaking [65, 66, 67] in which the Lagrangian is invariant under the gauge transformations, but the ground state (vacuum) no longer possesses the gauge symmetry. To be able to break the symmetry in this way, an external agent is necessary in the Standard Model. The Higgs field is this agent [40]. Without the Higgs boson the Standard Model is neither consistent nor complete, since the masses of the gauge bosons and fermions are generated through the interaction with the Higgs field [11]. Higgs boson couplings of fermions are proportional to the fermion masses [68]. Without the symmetry breaking the universe would be a 'boring' place with massless and indistinguishable fermions [58].

This is because of the special form of the Higgs potential (see section 4.1.2), which depends on two parameters, μ^2 and a dimensionless Higgs boson coupling λ; or alternatively υ^2 and λ.

The CERN Large Hadron Collider (LHC) is considered to be capable of directly observing the agent responsible for electroweak symmetry breaking and fermion mass

generation. This agent is believed to be a light Higgs boson with mass $M_H < 200$ GeV. The discovery of the Higgs boson will be possible by using the information about the decay products of the Higgs deposited in the calorimeter. From final state information, properties of the Higgs boson will be reconstructed and its mass and width will be measured.
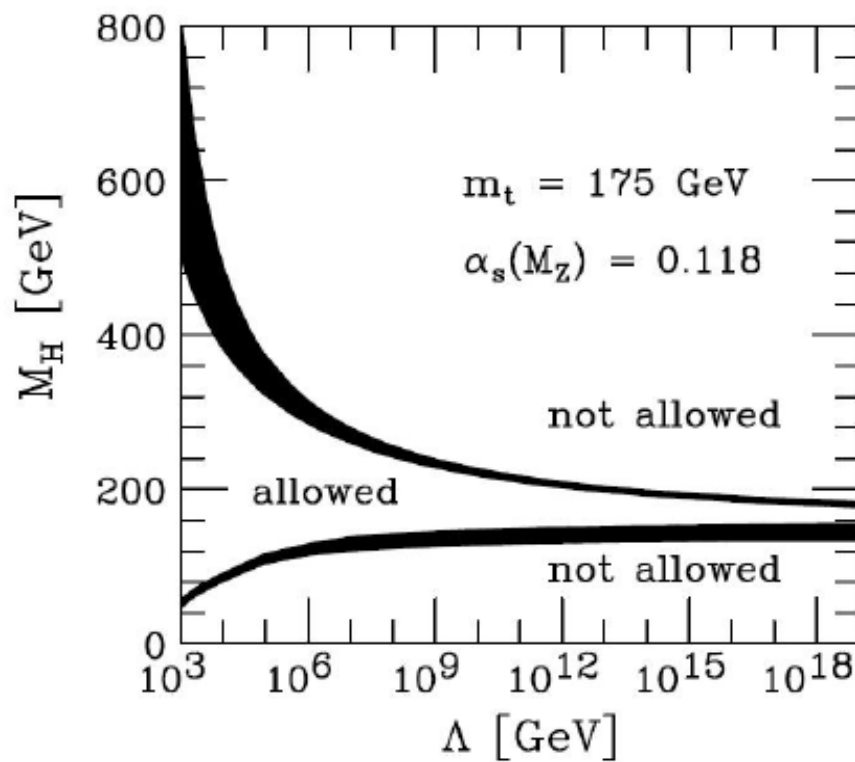
Figure 4.1: Theoretical upper and lower bounds on the Higgs mass as a function of the energy scale Λ up to which the SM is valid [69].

4.1.2 Higgs Boson Self-Coupling Constant

Once a Higgs boson candidate has been observed, emphasis will shift to a precise determination of its properties. In order to understand the shape of the Higgs potential, it is necessary to measure the SM Higgs self-coupling λ.

The Higgs potential can be expressed in terms of a Higgs doublet field as:

$$V_H = \mu^2(\Phi^\dagger\Phi) + \lambda(\Phi^\dagger\Phi)^2,$$

where Φ is the Higgs field, $\mu^2 = -\upsilon^2/\lambda$ and $\upsilon = (2G_F)^{-1/2}$ is the vacuum expectation value, G_F is the Fermi constant and λ is the Higgs boson self-coupling. Vacuum expectation value is what determines the scale of the symmetry breaking [58]. In the Standard Model, $\lambda = \lambda_{SM} = m_H^2/2\upsilon^2$ [70].

For $\mu^2 > 0$, the potential V has a global minimum at $\Phi = 0$. However, for $\mu^2 < 0$, the scalar potential has a circle of non-zero degenerate minima at $|\Phi|^2 = \upsilon^2/2$ (see Figure 4.2).
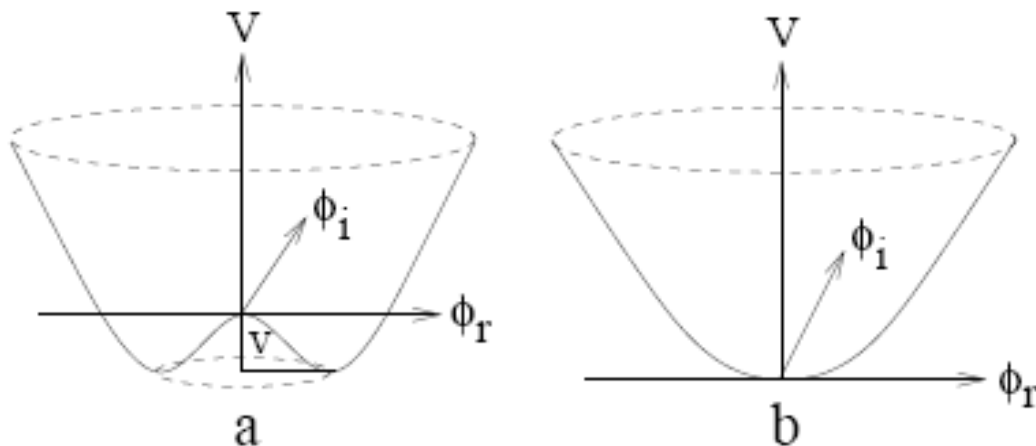
Figure 4.2: The scalar potential with (a) $\mu^2 < 0$ and (b) $\mu^2 > 0$. Φ_i and Φ_r are the imaginary and real parts of Φ.

The Higgs self coupling λ is a free parameter [71]. S-matrix unitarity constrains λ to $\lambda \leq 8\pi/3$. To measure λ and determine the Higgs potential, the Higgs boson pair production must be observed [70].

To fully determine the Higgs potential, we should measure the trilinear (g_{HHH}) and quartic (g_{HHHH}) Higgs boson couplings. The former coupling can be measured in Higgs pair production. To get g_{HHHH}, triple Higgs boson production is necessary. However, the cross section for HHH production is more than a factor of 10^3 smaller than those for Higgs pair production at linear colliders and about an order of magnitude smaller at hadron colliders. So, it is necessary to focus on g_{HHH}.
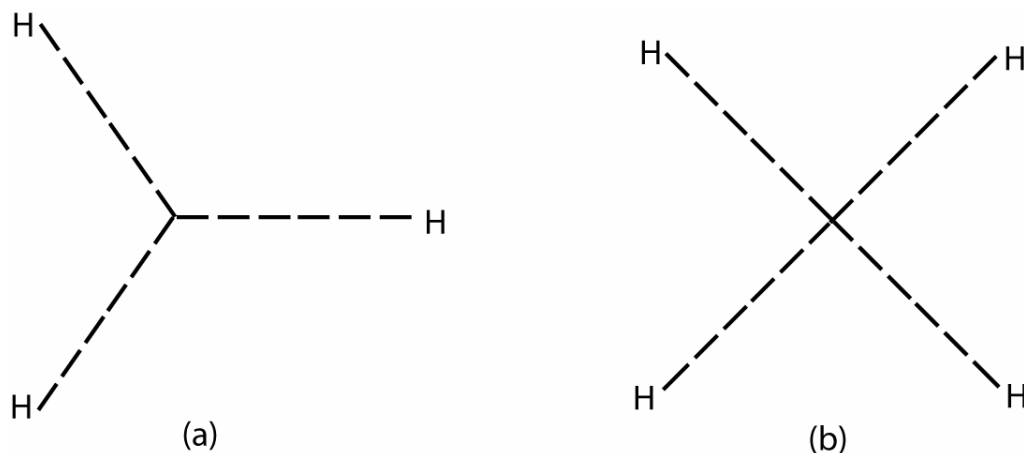
Figure 4.3: Feynman diagrams for the interactions of Higgs bosons. The trilinear Higgs coupling constant (from (a)) is given by $3m_H^2/\upsilon$. The quartic Higgs coupling constant (from (b)) is given by $3m_H^2/\upsilon^2$ [72, 73].

Since, the strength of the trilinear coupling influences the production rate of Higgs pairs in the SM, the Higgs potential can be found experimentally by measuring the cross section for Higgs pair production.

4.1.3 Higgs Pair Production in the LHC and Final State of Interest

In the LHC, there are different ways of producing Higgs pairs, such as gluon fusion (gg→HH), WW or ZZ fusion (WW, ZZ → HH), W or Z-strahlung (WHH and ZHH) (see Figure 4.4).
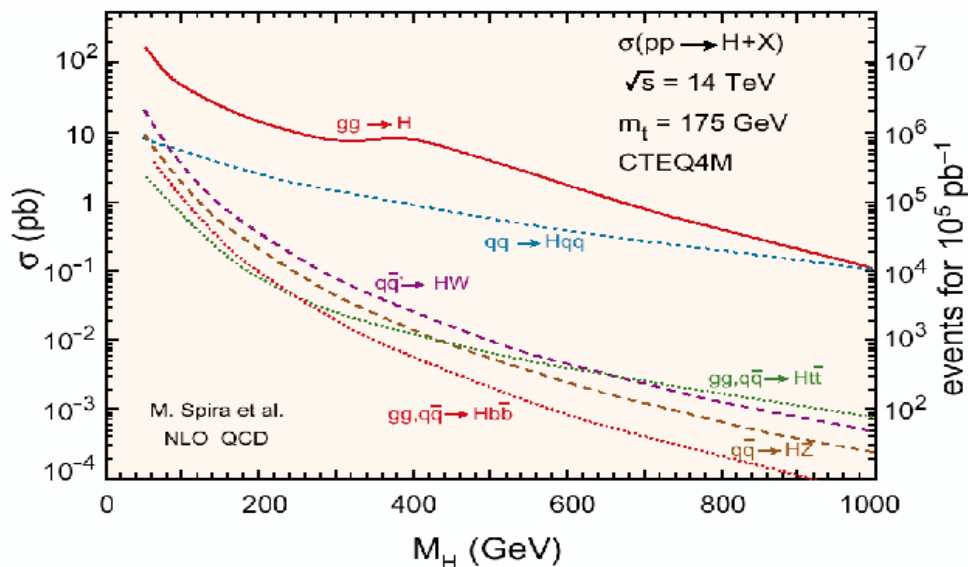
Figure 4.4: The cross sections for several Higgs production mechanisms at the LHC from M. Spira et al. [74].

This study involves the gluon-gluon fusion which has the highest cross section. At the LHC, inclusive Higgs pair production is dominated by gluon-gluon fusion, shown as the red curve in Figure 4.4. The Feynman diagrams contributing to gg→HH in the SM, consist of fermion triangle and box diagrams (Figure 4.5). Only the triangle diagram is sensitive to the Higgs self-coupling strength while the box diagram is not [73, 75, 76].

However, both of the diagrams are needed since they both contribute to the gg → HH production.
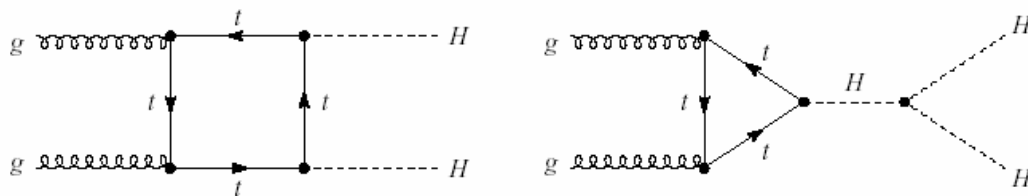
Figure 4.5: Feynman diagrams contributing to Higgs pair production via gluon-gluon fusion. Only the triangle diagram is sensitive to λ strength.

This process has been studied theoretically by U. Baur et al. [70, 75]. In this study, some of the U. Baur's analysis is enhanced by using the CMS fast simulation software to include the effects of the detector. The results at each stage of the production process are compared to the theoretical studies. The investigation of Higgs pair production channels is important towards opening the way for the determination of the Higgs coupling constant.

The work in this chapter is a step in the direction of a full simulation of signal and background. What would be involved in a simulation can be summarized as: parton level, initial and finals state showers, minimum bias events, detector effects.

For m_H < 140 GeV, H→ $b\bar{b}$ is the dominant decay mode of the SM Higgs boson. For m_H > 140 GeV, H→W$^+$ W$^-$ is the dominant channel, and W$^+$W$^-$W$^+$W$^-$ has the largest individual branching ratio. In the particular signal process we study, Higgs bosons decay to W boson pairs, which subsequently decay into two same-sign leptons and four jets. The W's do not need to be on-shell.

The process is:

$$gg \rightarrow HH \rightarrow (W^+ W^-)(W^+ W^-) \rightarrow (j \, j \, l^\pm \, \upsilon) \, (j \, j \, l'^\pm \, \upsilon),$$

where l and l' are any combination of electrons and muons.

There are also the background channels, which give the same final state (two same sign leptons and four separate jets) as the signal of interest. The background channel that has the biggest contribution is $pp \rightarrow W^\pm W^+ W^- jj$, where one W decays to two jets and other two W's leptonically. The next most important background is $pp \rightarrow t\bar{t}W^\pm$, where one top quark decays leptonically, the other hadronically, and neither b quark jet is tagged. Other background processes are continuum $pp \rightarrow WWjjj$ production, $pp \rightarrow t\bar{t}t\bar{t}$ production where none of the b quark jets are tagged, and additional jets or leptons are not observed, $pp \rightarrow WZjjj$, $pp \rightarrow t\bar{t}Z$, $pp \rightarrow WWZjj$ with leptonic Z decay where one lepton is not observed, and $pp \rightarrow t\bar{t}j$ events where one b quark decays semileptonically with good hadronic isolation and the other is not tagged [70, 75]. The largest background will be analyzed more in detail in Section 5.5.

<u>4.2 Signal Channel</u>

The CMS is a powerful muon detector, so, we produced events with only muons and jets in the final state. The signal is therefore:

$$gg \rightarrow HH \rightarrow (W^+ W^-)(W^+ W^-) \rightarrow (j \, j \, \mu \, \upsilon) \, (j \, j \, \mu \, \upsilon),$$

The intermediate Higgs and W bosons are treated off-shell using finite widths in the double pole approximation [70].

U. Baur's code is used to generate the events. This code, which is a combination of Fortran 90 and Fortran 77, was not made to produce events suitable to CMS software. Unlike many signal channels, of which the already simulated events are provided for

analysis by the CMS collaboration, the signal channel we worked on did not have pre-produced events. We had to convert the output of Baur's code into a format which can be understood by the CMS software. After a great deal of trials, we decided to modify the code output so that it mimics the output of the generators ALPGEN [77], which has an interface with the CMS software. More information about ALPGEN will be provided in the next section. The production of the events was difficult. Part of the issue is the loop graphs (Figure 4.5). Some integral contributions from the two tree level loops have to cancel each other. It is not possible to make the calculations numerically. They have to be done analytically.

The original code uses Cteq4 parton distribution functions (PDFs) [78]. As a first step, we replaced the Cteq4 PDFs with Cteq6 PDFs [79], since they are more up to date. The Cteq6 contains 4 standard sets of PDF's: CTEQ6M, CTEQ6D, CTEQ6L, and CTEQ6L1. We are using the leading order PDF (CTEQ6L). All fits for Cteq6, with the exception of Cteq6L1, are obtained by using the same coupling strength $\alpha_s = 0.118$ and the NLO (next to leading order) running α_s formula. Table grids used in the Cteq6 Fortran program are generated for $10^{-6} < x < 1$ and $1.3 < Q < 10000$ (GeV), where x is the Bjorken_X and Q is the energy scale. The lambda QCD value in MeV for 5 flavors (Lam5) is 226 and Lam4 is 326 [80, 81].

We ran the code for six different Higgs mass values. The Higgs masses and corresponding cross sections and event production for a luminosity of 300 fb^{-1} are given in Table 4.2. A luminosity of 300 fb^{-1} corresponds to three years of operation of the LHC. The differential cross section values are multiplied by a factor K=1.65 (K-factor) to take into account the next to leading order QCD corrections [70].

Higgs' Mass (GeV)	Cross Section (fb)	# of events for 300 fb^{-1}
150	0.98541 x 10^{-2}	2.96
160	2.57037 x 10^{-2}	7.71
170	2.70798 x10^{-2}	8.12
180	2.34399 x 10^{-2}	7.03
190	1.41608 x 10^{-2}	4.25
200	1.08885 x 10^{-2}	3.27

Table 4.2: The Higgs boson masses and corresponding cross section values and number of events for 300 fb^{-1}.

As can be seen, the number of events produced at a luminosity of 300 fb^{-1} is very low. Therefore, the SLHC conditions will be necessary to obtain a substantial number of events with this signal channel.

4.3 Comparison of Smearing and No-smearing of the Signal

U. Baur et al. used the generator level events with leptons, quarks and gluons to analyze the channel and understand the Higgs coupling constant. They added smearing to the code to give a shower-like effect to the momenta. As a first step, we compared the output of Baur's with and without smearing. All the plots referenced in this section are for 180 GeV Higgs mass. It is seen that the results are close to each other. As is anticipated, the masses of the W and Higgs bosons and of leptons are not affected by smearing. The Higgs momenta are slightly higher for the smearing case. The difference in mean values is 0.02 GeV. Lepton-jet and jet-jet separations are almost the same too.

There are some small differences in momenta of the particles. Figure 4.6 and 4.7 show the distributions of the sum of the momenta of the four jets and two muons in the

final state for the no-smearing and smearing case, respectively. The profiles are almost the same. The mean values are 310.0 GeV for the no-smearing case and 310.6 GeV for the smearing case.

The invariant mass of all the final state particles is an important feature of this channel. All the backgrounds are multi-body production processes, and thus the distribution of the invariant mass, $s^{1/2}$, of the system peaks at values significantly above the threshold, whereas, the signal is a two-body production process. Therefore, for the signal, the $s^{1/2}$ distribution will have a sharper threshold behavior [70, 75].
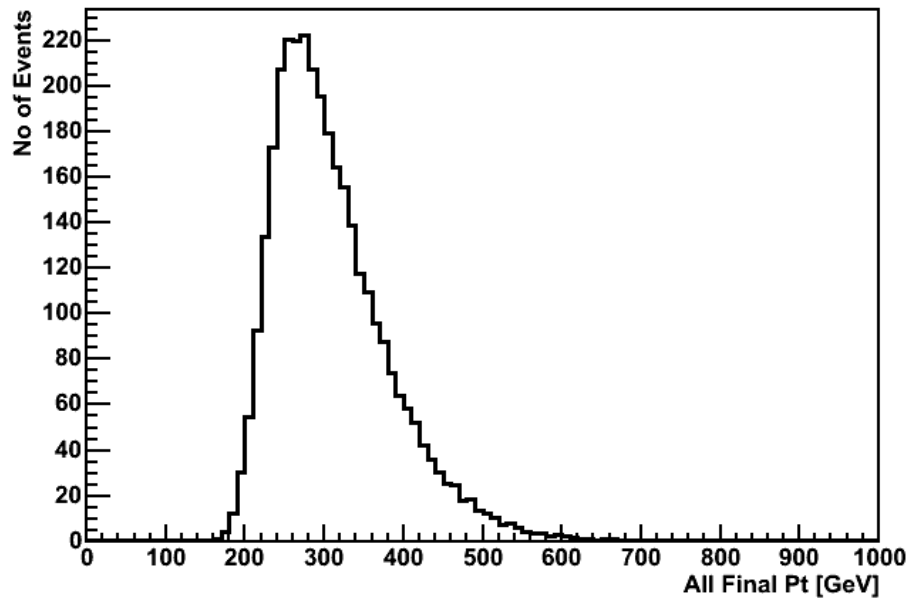
Figure 4.6: The sum of the P_T of four jets and two muons in the final state for the no-smearing case for the 180 GeV sample.
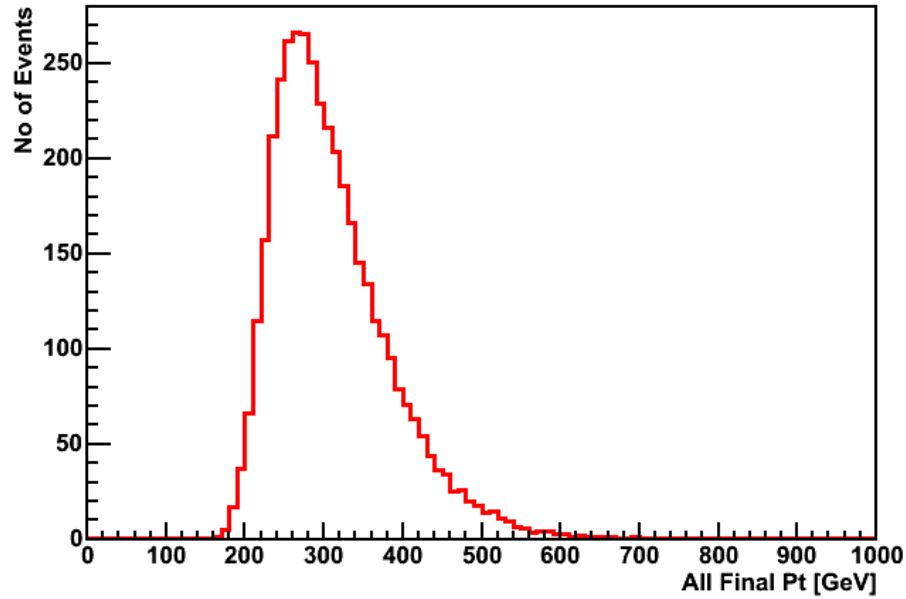
Figure 4.7: The sum of the P_T of four jets and two muons in the final state for the smearing case for the 180 GeV sample.

It is anticipated that the invariant mass of all observed final state leptons and jets will have most of the expected behavior of the different production processes. Due to the two neutrinos in the final state, it is not possible to obtain the total invariant mass. However, the visible mass, which is given by the equation below, is supposed to retain the same behavior as the invariant mass for different production processes [70, 75]. In this equation, E is the energy and P is the momentum of the particles. They are summed over all four final state jets and two final state leptons.

$$m_{vis}^2 = \left[\sum_{i=\ell,\ell',\text{jets}} E_i \right]^2 - \left[\sum_{i=\ell,\ell',\text{jets}} \text{P}_i \right]^2$$

The visible mass distributions for the no-smearing and smearing cases for the signal are shown in Figures 4.8 and 4.9 respectively. The mean values are 380.9 GeV and

381.8 GeV. Again, the profiles are very similar to each other with some minor differences.

4.4 CMKIN

CMKIN [82, 83] is a computer program used as an interface between the user and an event generator that is written in Fortran. The input of a CMKIN job is a data card with parameters passed to the generator. The data cards include information such as the total CMS energy, the kinematic limits for individual particles, and so on [82]. The output is an hbook ntuple containing the generator (RawParticle) information. The output can be analyzed with PAW or transformed into a ROOT tree format.
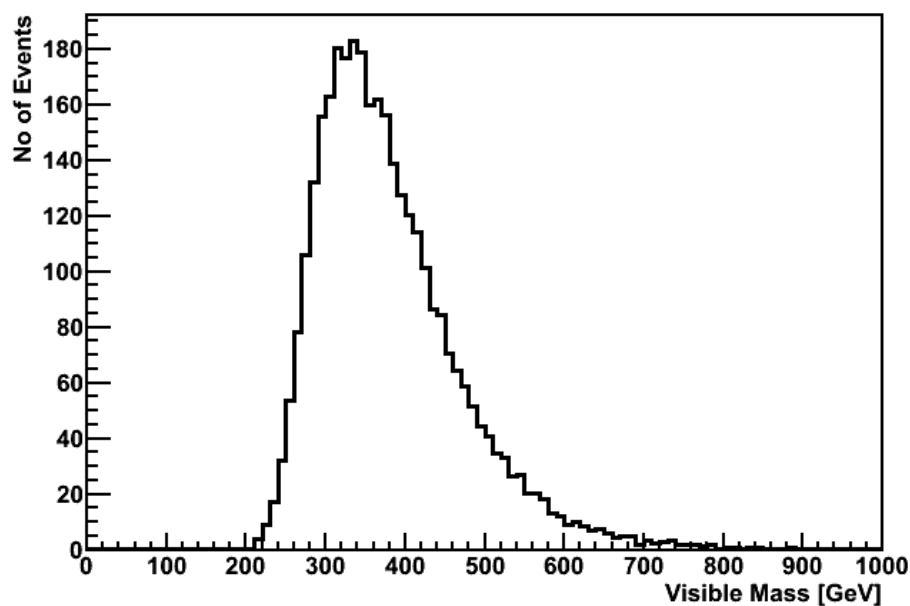
Figure 4.8: Visible mass distribution for the no-smearing case for the 180 GeV sample.
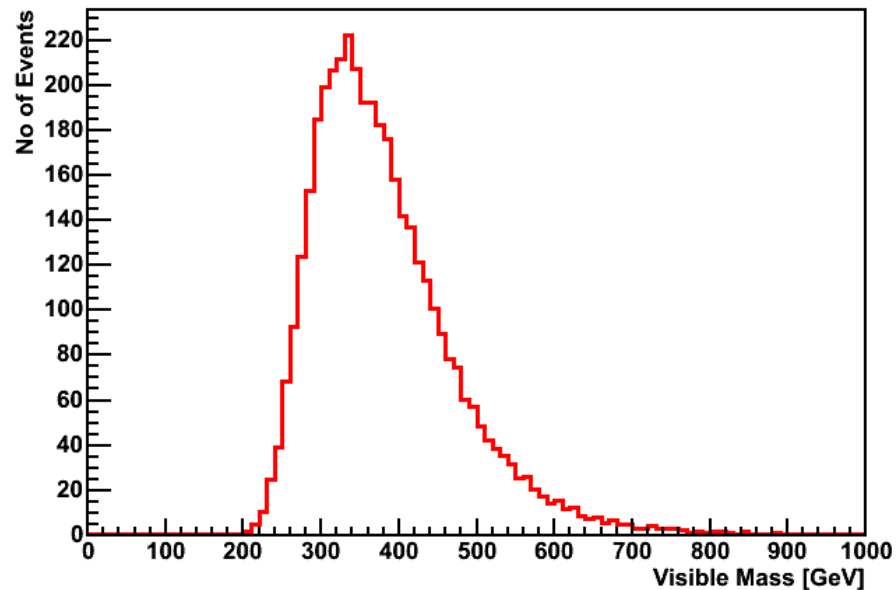
Figure 4.9: Visible mass distribution for the smearing case for the
180 GeV sample.

CMKIN includes PYTHIA [84] which is a Fortran 77 program frequently used for the generation of high energy collisions. It is made to generate complete events containing as much information as possible based on the current physics understanding. PYTHIA provides a wide range of reactions including parton showers. The multiparticle production with the collision of elementary particles is emphasized in PYTHIA.

The output of the CMKIN is kept in the output of the detector simulation program as Generator Level Information. These are the objects (jets, muons, missing transverse energy (MET)) after the shower but before the detector effects. Since the investigation of this situation is possible by studying the output of the detector simulation, we will leave this to the next section.

<u>4.5 FAMOS</u>

The detailed simulation and computer reconstruction of particle tracks in the CMS experiment is time and CPU consuming. To provide the possibility of studying a large Monte-Carlo sample in small amount of time, the computer program FAMOS [85] has been developed.

FAMOS is a dynamically configurable system for fast simulation and reconstruction for the CMS. In FAMOS, the detailed modeling of energy losses, material effects, and reconstruction algorithms are replaced by simpler algorithms. FAMOS is much faster than the elaborate detector simulation and reconstruction package, but it has the disadvantage of low precision [86]. In this study, the signal and background channels are simulated using FAMOS. The pile-up, which will be investigated in detail in section 4.5.4, is added to all the samples and the kinematic cuts are applied.

The same sets of cuts are applied to both the signal and background. These are as follows: P_T of jets > 20 GeV, $|$ Jet $\eta| < 3$, minimum # of jets ≥ 4, maximum P_T jet > 30 GeV, minimum number of $\mu \geq 2$, P_T of μ's > 15 GeV, $|\mu\eta| < 2.5$. These are the same cuts applied by U. Baur et al. in their theory study.

4.5.1 The Generator Level Information

The detector simulation contains a jet algorithm to find the jet. The input to this algorithm is the collection of calorimeter towers or collection of generator level particles where all particles are stable. The algorithm we chose to used in FAMOS is the iterative cone algorithm with cone size ΔR ($=[(\Delta\Phi)^2 + (\Delta\eta)^2]^{1/2}$) $= 0.5$ [87]. The FAMOS output contains the information about generated level particles, jets and MET along with reconstructed objects such as reconstructed jets, MET, muons etc.

However, U. Baur's code creates particles only on the parton level. It decays W bosons to the user selected final state particles (four jets, two muons and two neutrinos in our case). These are the particles used as an input for PYTHIA for parton showering. Since W bosons are already decayed in our case, what PYTHIA does is to shower the quarks in order to provide stable particles for jet reconstruction for detector simulation. Baur's code adds a correction to the momenta of the partons, so that the output looks as similar as possible to the detector output.

Therefore, the smearing plots obtained from the original code and the generator level plots are very different from each other. Not only are the mean values different, but so are the shapes of the distributions, as is expected. As explained, the reason for this is the addition of the showers. The fact that jet algorithms have their deficiencies adds some error to the generator level particles (GenPart) information. Figure 4.10 and 4.11 display the maximum P_T distributions of the jets for the GenPart and the theory smearing case respectively. The big difference in mean should be noted. The minimum P_T distributions for these two cases can be seen in Figure 4.12 and 4.13. Although the mean values are closer to each other, they are still different.
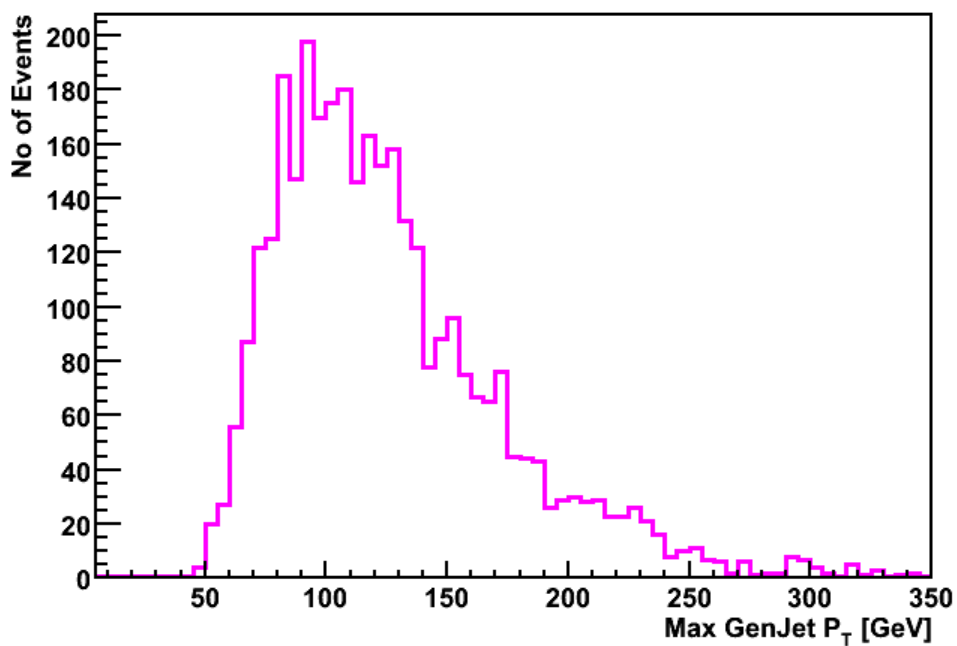
Figure 4.10: Maximum GenJet P_T distribution for the 180 GeV sample. The mean is 126.1 GeV.
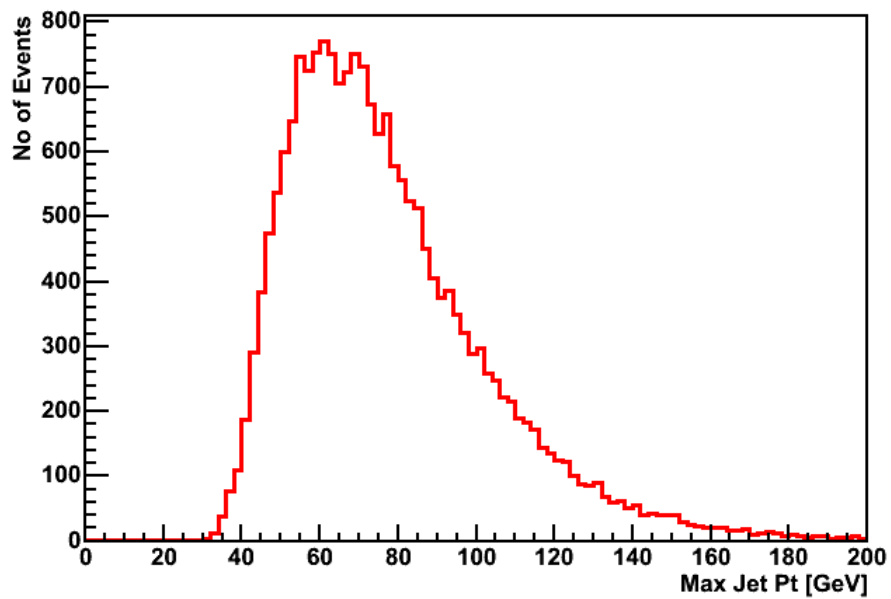
Figure 4.11: Maximum jet P_T for the smearing case for the 180 GeV sample. The mean is 77.5 GeV.
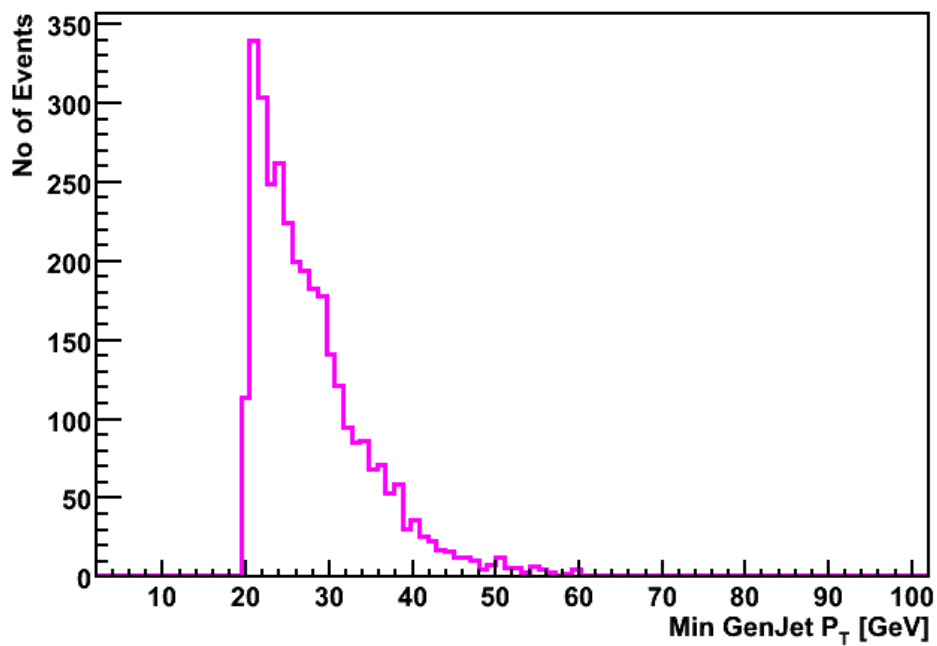
Figure 4.12: The minimum P_T distribution of GenJets for the 180 GeV sample. The mean is 26.92 GeV.
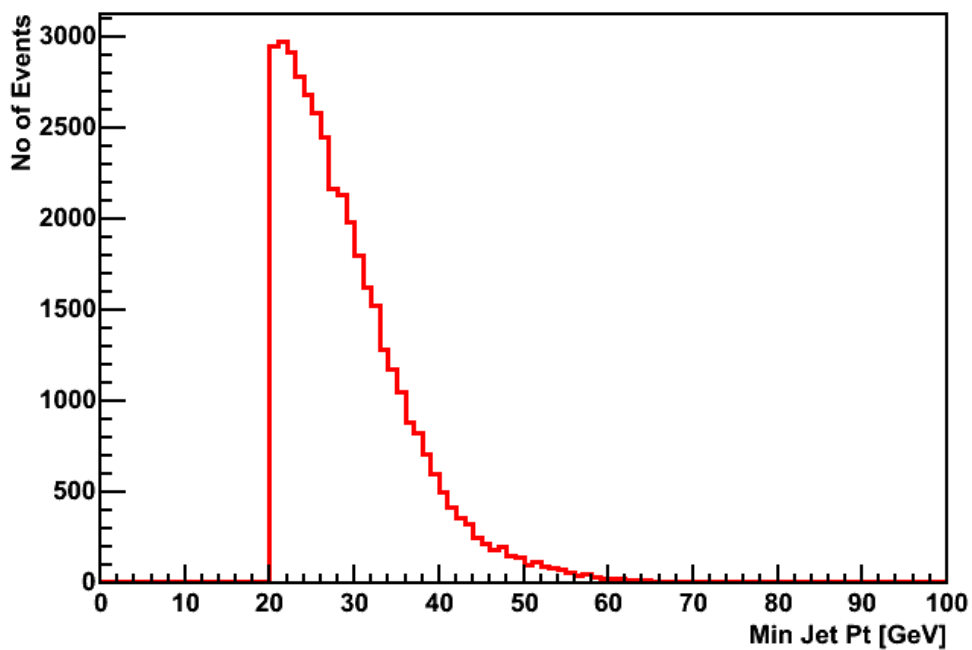
Figure 4.13: Minimum P_T distribution of jets for the smearing case for the 180 GeV sample. The mean is 29.14 GeV.

4.5.2 Comparison between the Generator Level Information

and the Detector Output

In order to see the detector effects, we compared the information of the objects obtained after the detector effect (reconstructed objects) with the generator level objects. Figures 4.14 and 4.15 display the distribution of the sum of the P_T of four jets and two muons in the final state (named 'all P_T') for the reconstructed and generator level cases, respectively. The mean is 291.4 GeV for the first case and 512.1 GeV for the second one. There is a big difference between these two numbers. The transverse momentum values for any object in the generator level are much higher than those of the reconstructed ones. This is an expected feature. The resolution and the efficiency of the calorimeter is not ideal. Therefore, the jets should be corrected. The detector will be calibrated using well-known decays when the real data arrives. Previous studies have shown that the ratio between the P_T 's of the generator level jets (genjets) and the reconstructed jets (recjets) is anticipated to be between 1.5 and 2. This ratio is not constant and it deviates at higher P_T values. The ratio of the mean of the two plots below is equal to 512.1/291.4 = 1.76. Similarly, the ratio of the mean of the maximum P_T distributions of the genjets and recjets is 62.51/44.11 = 1.76, again.
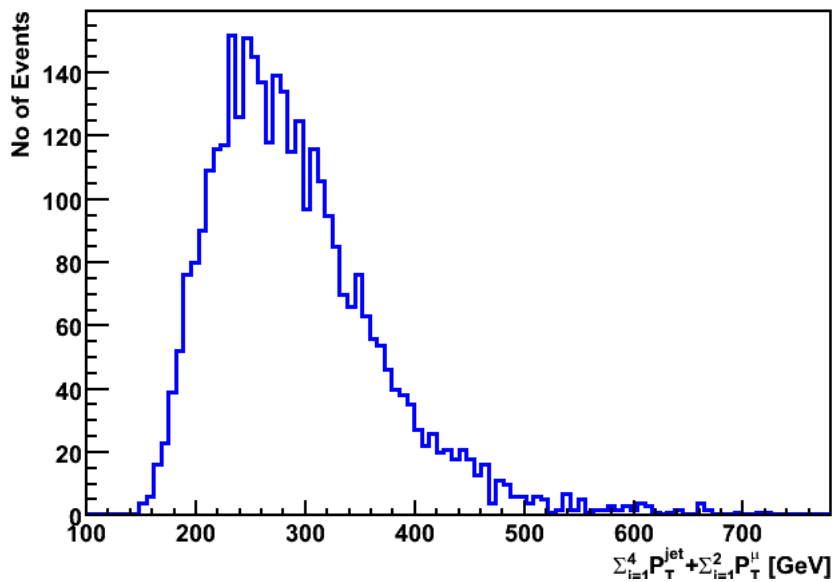
Figure 4.14: Distribution of the sum of the momenta of four jets and two muons in the final state from the reconstructed objects for the 180 GeV sample. The mean is 291.4 GeV.
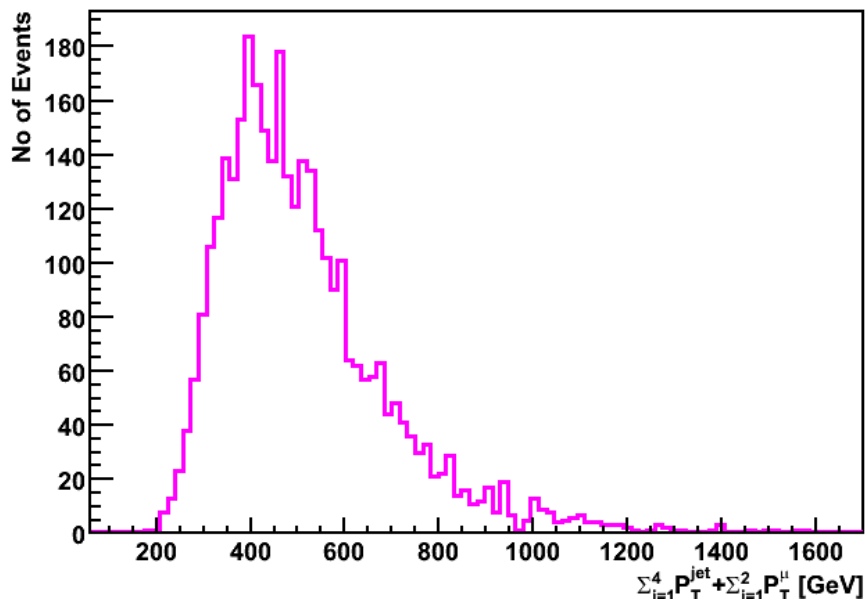
Figure 4.15: Distribution of the sum of the momenta of four jets and two muons in the final state from the generator level objects for the 180 GeV sample. The mean is 512.1 GeV.

4.5.3 Comparison between the Detector Output and the

Theory

When the smearing is included, the generator code is to generate the events so that they are as close as possible to the reconstructed objects. These are the objects present in the output of FAMOS. They include both parton shower and detector effects. In this section we compare the output from the reconstructed particles to the output of the original code. Table 4.3 shows the mean values of some of the distributions obtained from the output of the code and the output of the detector. It should be noted that the minimum and maximum jet and lepton distribution and MET means are close to each other.

	Theory with smearing	Detector output
Jet P_T min / max	29.14 GeV / 77.5 GeV	25.49 GeV / 71.65 GeV
Lepton P_T min / max	37.24 GeV /67.35 GeV	38.3 GeV / 68.14 GeV
All P_T / All Hadron P_T	310.6 GeV / 203.8 GeV	291.4 GeV / 185.0 GeV
Visible mass / MET	381.8 GeV / 55.77 GeV	402.2 GeV / 60.54 GeV
Jet dR min / max	1.6 / 2.8	1.14 / 3.5

Table 4.3: The mean values of some of the distributions from the theory case with smearing and detector output.

The lepton P_T distribution for the smearing case (red) and detector output (blue) are shown in Figures 4.16, 4.17, 4.18, and 4.19. Not only are the mean values are similar to each other, but so are the profiles.
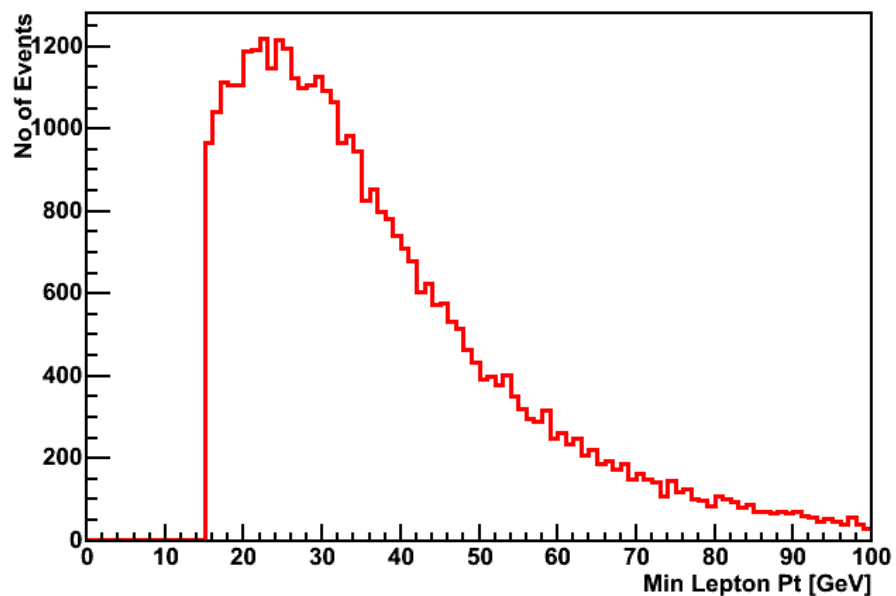
Figure 4.16: Mimimum P_T distribution of the leptons obtained from the theory case with smearing for the 180 GeV sample.
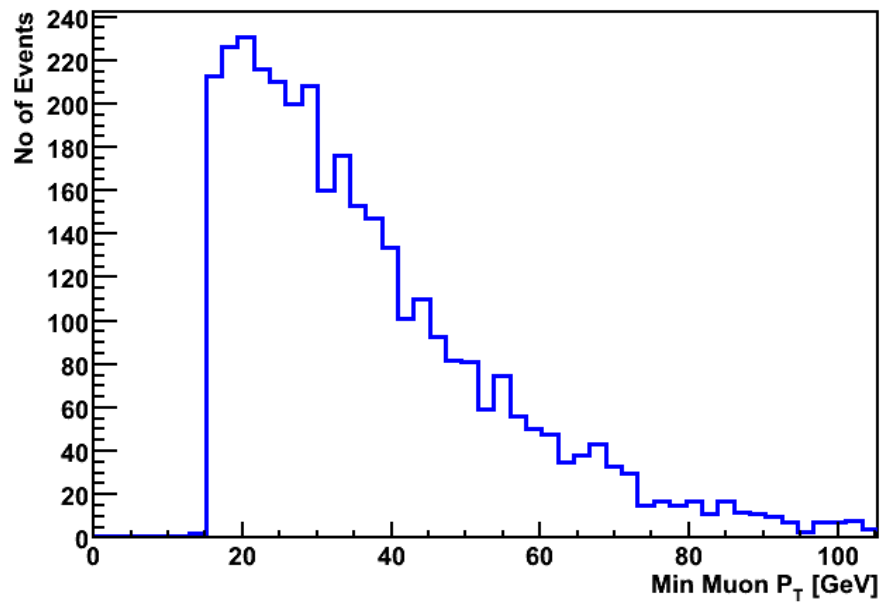
Figure 4.17: Minimum P_T distribution of the leptons obtained from the detector output for the 180 GeV sample.
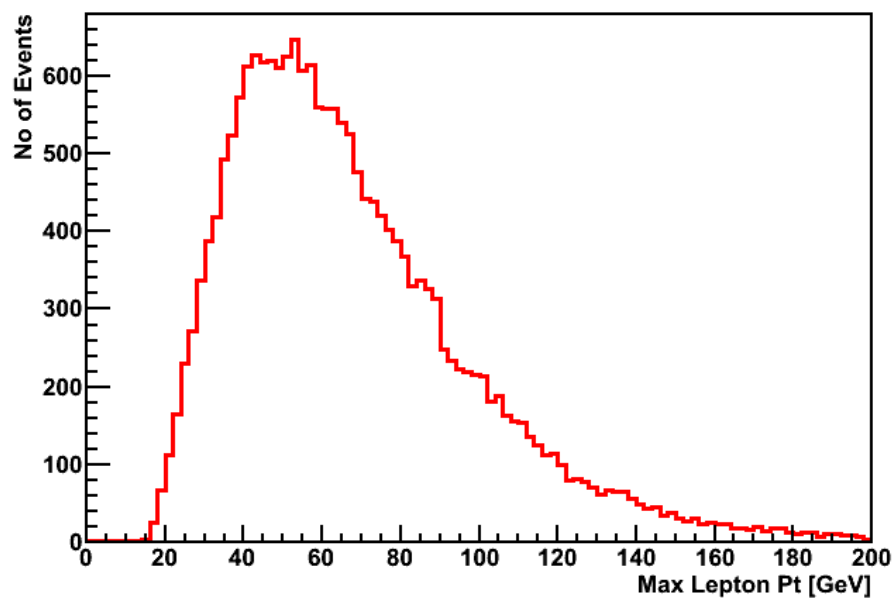
Figure 4.18: Maximum P_T distribution of the leptons obtained from the theory case with smearing for the 180 GeV sample.
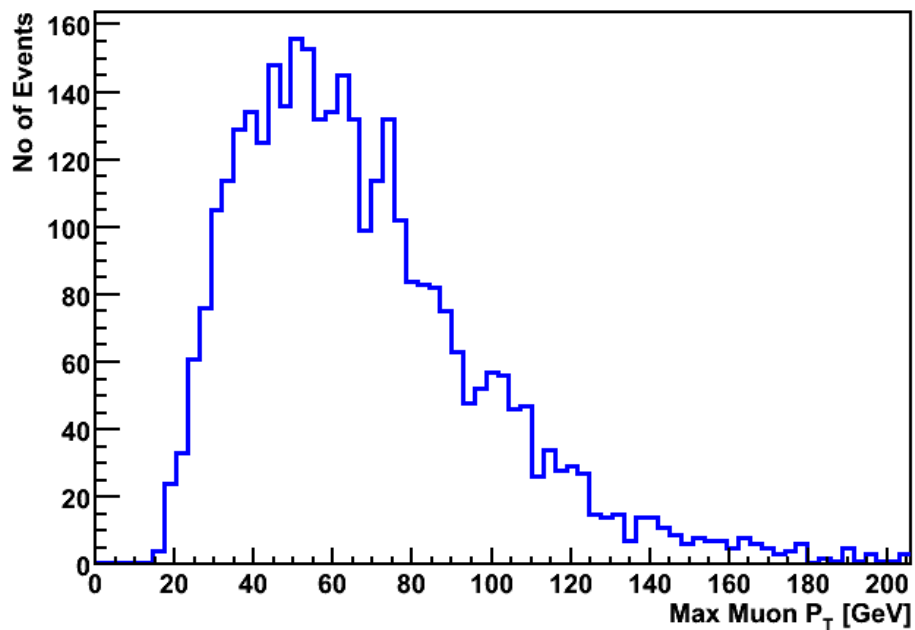
Figure 4.19: Maximum P_T distribution of the leptons obtained from the detector output for the 180 GeV sample.

The mean values for the All P_T and All Hadron P_T are much higher for the code output. (The All Hadron P_T is defined to be the sum of the P_T of the four jets in the final state.) Also, the jet separation in the pseudorapidity – azimuthal angle plane, given by $\Delta R = [(\Delta\Phi)^2 + (\Delta\eta)^2]^{1/2}$, has different mean values for the two cases. The existence of pile-up, differences and deficiencies in jet reconstruction algorithms, theory assumptions which are not exact can be the reasons of these differences.

4.5.4 The Pile-up

When running at high luminosity with the bunch crossing of the LHC, the interaction rate is about 10^9 events/s. On average 25 minimum bias events (soft interactions) will occur simultaneously at each crossing. As a consequence, every 25 ns about 1000 charged particles will be seen in the detector over the region of $|\eta| < 2.5$ [68].

When a high P_T event is produced during a bunch crossing, on average 25 additional soft events will overlap with this event. These soft events are therefore called 'pile-up'. The fact that minimum bias events have small P_T can be used to separate the 'useful' high P_T events from the pile-up. Also, for $|\eta| < 2.5$, the location of the events along the beam axis can be located to within very small distances using the tracker. This allows the identification of most of the pile-up events.

The pile-up is one of the major difficulties encountered during the experimental operation of the LHC and the design of the detector is largely affected by this problem. To reduce the pile-up the detectors must have a fast response time and a fine readout granularity [68].

In order to see the effects of pile-up events in FAMOS, we created the signal events for a 180 GeV Higgs mass with and without pile-up events without any kinematic cuts. In the pile-up case, 3.5 pile-up events are added to every event. This number is very small compared to the real amount of pile-up events. Unfortunately, software related constraints do not allow the simulation of too many pile-up events. Since the number is small, the pile-up effect is small too. However, it is possible to see a change in the expected direction when the pileup is taken out. When the same sets of events are created with pile-up, the mean number of jets in one event is increased from 5.5 to 6.3, and the number of entries is increased from 9670 to 9716. As it is expected, in the case of pile-up we are dealing with more particles. During this study, we did not use any additional jet cuts to highlight the difference. The only cut made was the 10 GeV jet cut which is present in the reconstruction code by default. Figures 4.20 and 4.21 show the transverse momentum distributions of the jets for samples with and without pile-up, respectively. The mean minimum P_T value for the pile-up case is 12.9 GeV and 14 GeV for the no pile-up case. This is reasonable, since the pile-up events introduce soft jets. Hence, there will be more jets with lower P_T values. The effect of these soft jets is also seen in the average of the P_T of jets. The mean value is decreased from 33.1 to 31.1 GeV. On the other hand, the energies of some of the minimum bias jets can be added to the jets by the calorimeter. This would cause an increase in some of the distributions, such as the maximum P_T of the jets. To make up for the pile-up deficit in the experiments, adequate P_T cuts should be applied for the jets.
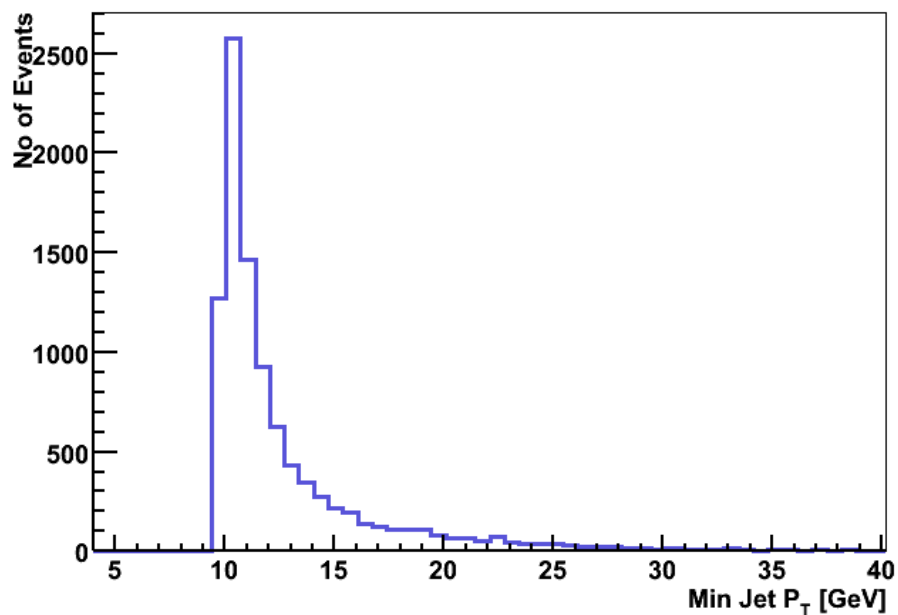
Figure 4.20: Minimum P_T distribution of jets with pile-up and without cuts for the 180 GeV sample.
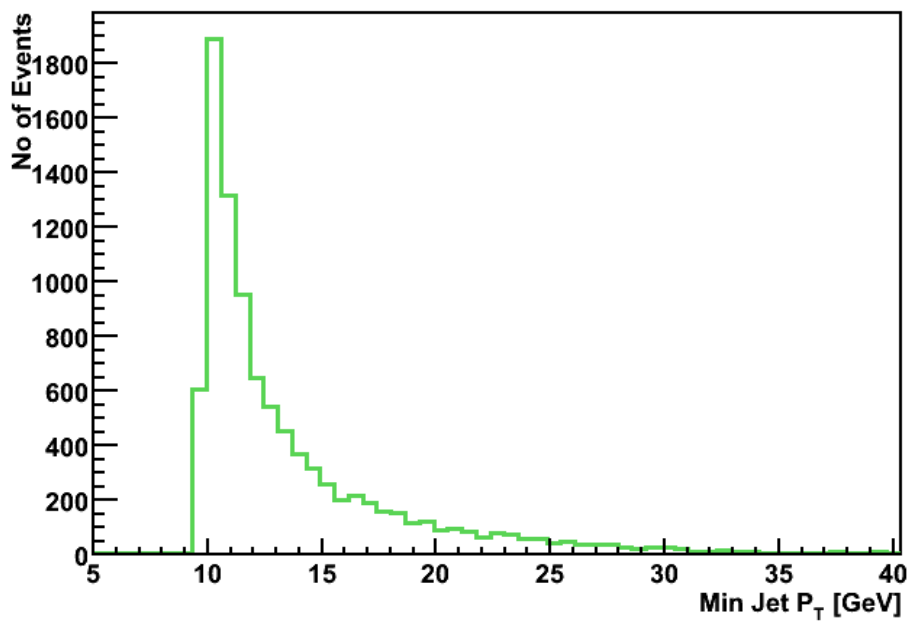
Figure 4.21: Minimum P_T distribution of jets with no pile-up and no cuts for the 180 GeV sample.

Also, one could expect that pile-up would add to the MET. The production of extra neutrinos or a misreading of the soft jet momenta can be the cause of this increase. When the METs obtained from calorimeter hits for each case are compared, it is seen that, the pile-up case has a slightly higher MET than the no-pileup case. Figures 4.22 and 4.23 show the MET distributions of the pile-up and no pile-up cases respectively. The mean values are 59.8 GeV for the pile-up case and 59.6 GeV for the no pile-up case.
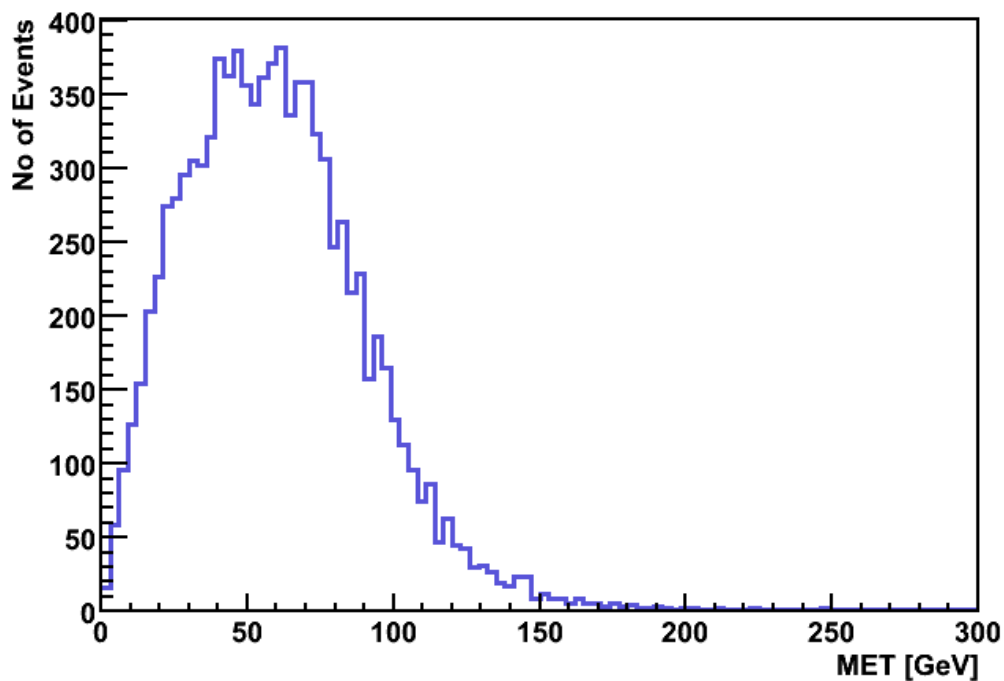
Figure 4.22: MET of the pileup and no cuts case for 180 GeV sample.
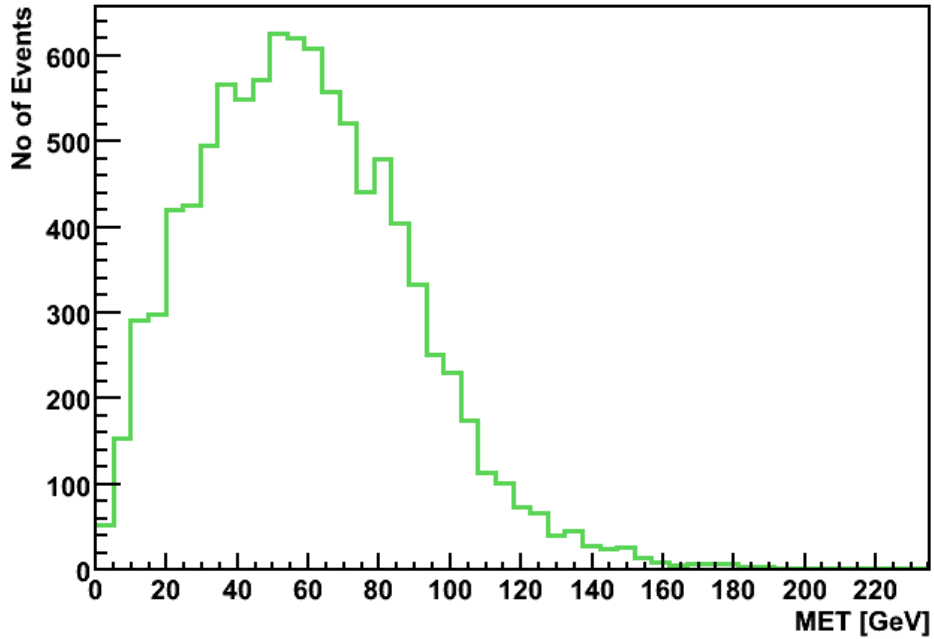
Figure 4.23: MET of the no-pileup and no cuts case for 180 GeV sample.

4.6 The Background and the Signal

4.6.1 The Largest Background Channel

As stated before, the background processes that produce two same sign leptons and four well-separated jets, which reconstruct in two pairs to a window around the W boson mass, are the SM backgrounds of interest. The background channel that has the biggest contribution is, $pp \rightarrow W^{\pm} W^{+} W^{-} jj$ where one W decays to two jets and other two W's leptonically. This background is follwed by $pp \rightarrow t\bar{t} W^{\pm}$, where one top quark decays leptonically, the other hadronically, and neither b quark jet is tagged. The generator level events for these two biggest background channels are produced using ALPGEN [77], which is an event generator created for the study of hard multiparton processes in hadronic collisions. The leading order in quantum chromodynamics (QCD)

and electroweak (EW) interactions is included in the code. This generator performs calculations of the exact matrix elements for a large set of parton level processes of the Tevatron (Fermilab) and LHC. The full information about the color and flavor structure of the parton level events is provided. This enables the partons to evolve into fully hadronised final states in other software codes.

Events generated with ALPGEN were put into CMKIN and, then into the CMS software.

The transverse momentum distribution of generator level jets for the largest background is shown in Figure 4.24 and the generator level missing transverse E_T distribution is given in Figure 4.25. The plots look scattered due to the small number of events.
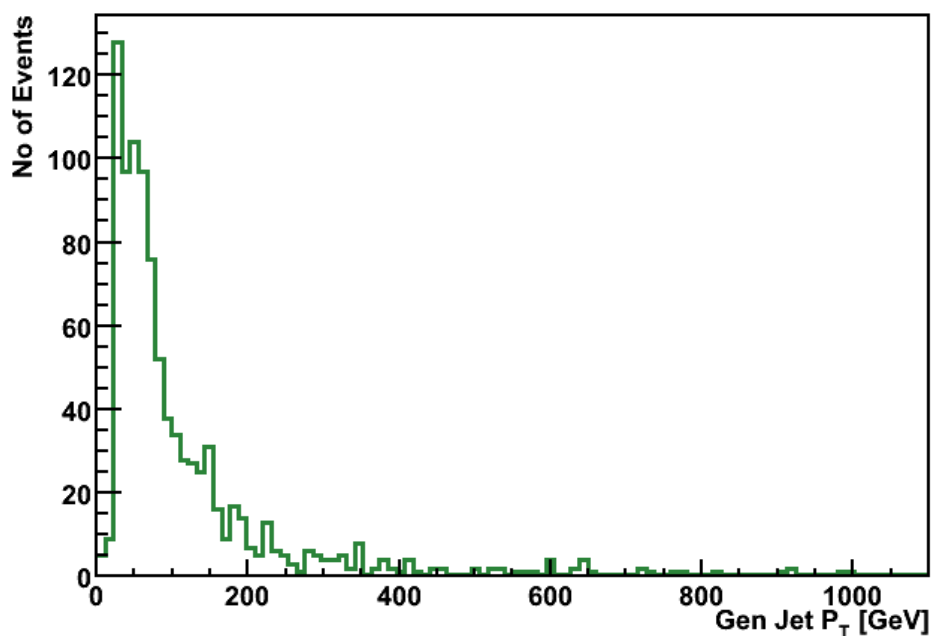
Figure 4.24: The P_T distribution of the generator level jets for the background sample. The average is 116.1 GeV.
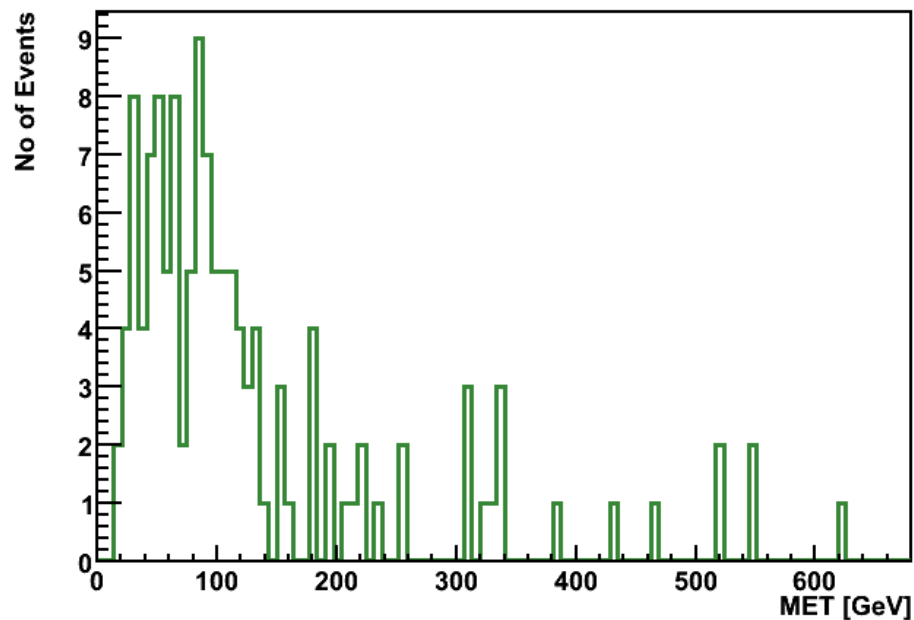
Figure 4.25: The generator level MET distribution for the background. The mean is 132.4 GeV.

4.6.2 How to Distinguish the Signal from the Background?

As stated earlier, the signal is a two body process, whereas, all the background channels are multibody processes. This fact affects the visible mass distribution. Figure 4.26, 4.27 and 4.28 show the visible mass distribution for the signal with 180 GeV and 170 GeV Higgs masses and the main background. The visible mass is calculated using the reconstructed objects.
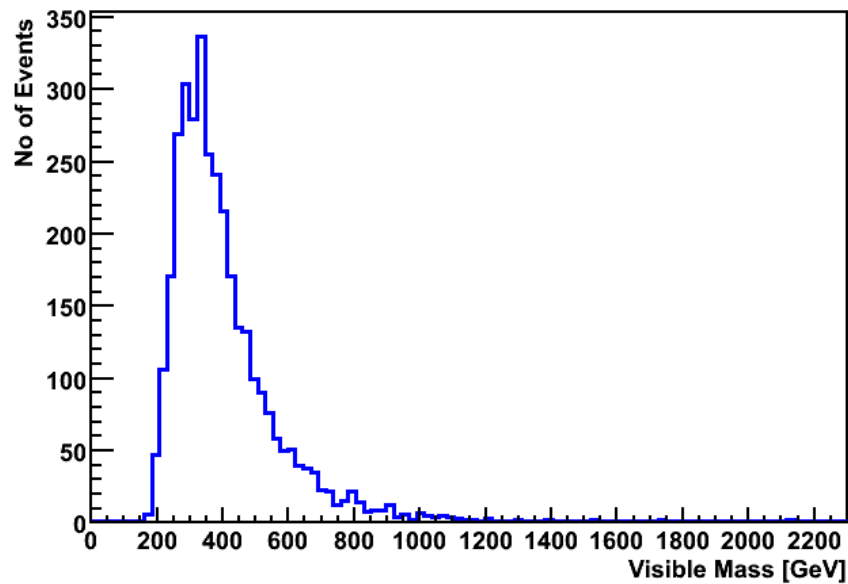
Figure 4.26: The visible mass distribution for the 180 GeV sample. The mean is 407 GeV.

The background has a mean of around 855 GeV which is much higher than that of the signal samples (407 GeV for 180 GeV sample and 395 GeV for the 170 GeV sample). The fact that the signal peaks at smaller values of the visible mass is expected [70]. Also, the background has a tail that extends to higher values of the visible mass. As the Higgs mass decreases, the signal peak moves gradually at lower m_{vis} values [70]. This can be seen in Figure 4.29 where the visible mass distributions for the two signal samples are displayed together. The logarithmic y axis represents the number of events per fb^{-1}. The red line represents the 180 GeV sample and the blue line the 170 GeV sample. The peak for the 170 GeV sample is at slightly lower values. The tail of the 180 GeV sample extends to higher values of the visible mass. This is also predicted by the theory.
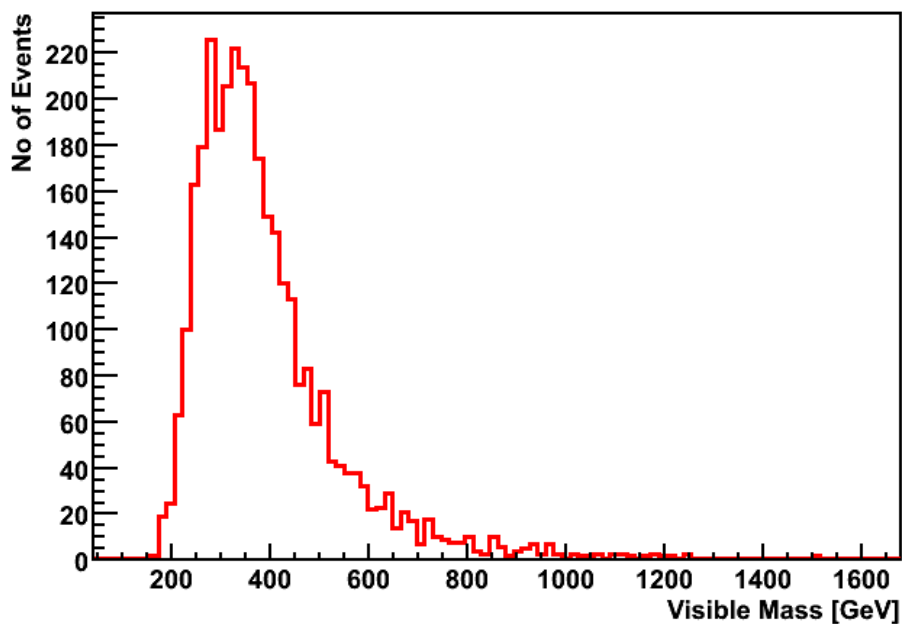
Figure 4.27: The visible mass distribution for the 170 GeV sample. The mean is 395 GeV.
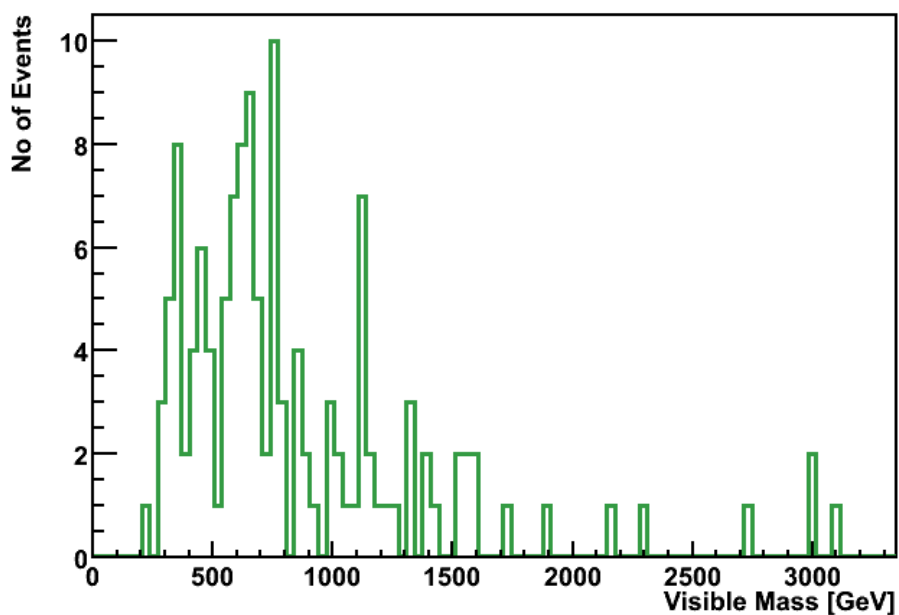
Figure 4.28: The visible mass distribution for the background. The mean is 855 GeV, which is much higher than the means of the signal samples.
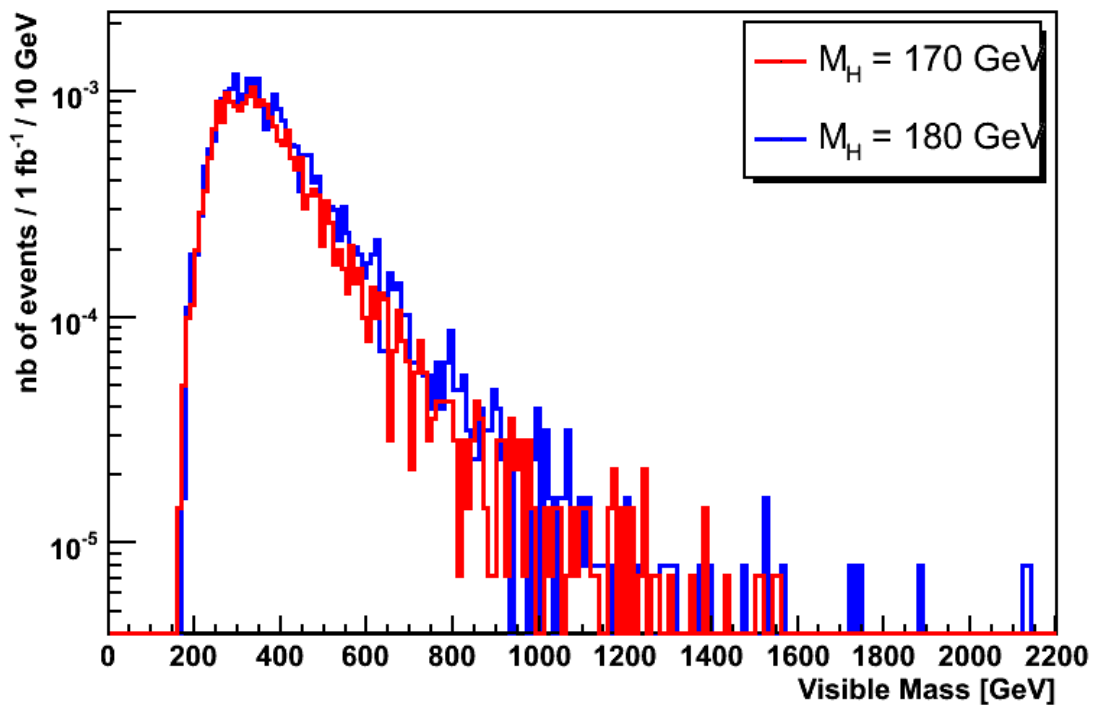
Figure 4.29: The comparison of the visible mass distributions of the 180 (red line) and 170 (blue line) GeV samples. The y axis represents the number of events per 1fb[-1] and it is in logarithmic scale. The tail for the 180 GeV sample extends to higher visible mass values.

Also, the final state particles for the signal are distributed fairly isotropically, since the Higgs bosons are produced almost at rest [75]. This results in a minimum jet-jet separation higher than the background. As can be seen in Figure 4.30, the mean for the minimum jet-jet separation of the signal is around 1.14, whereas the mean for the main background is 0.97 (see Figure 4.31).
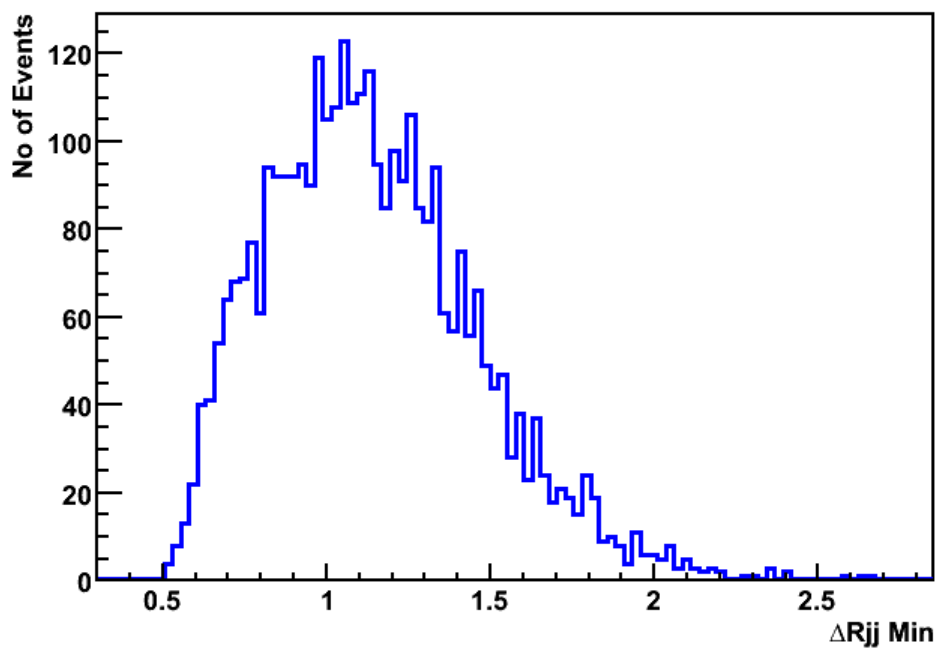
Figure 4.30: Minimum jet jet separation for the signal with the 180 GeV Higgs mass (from reconstructed particles). The distribution is wide and the peak is around 1.1.
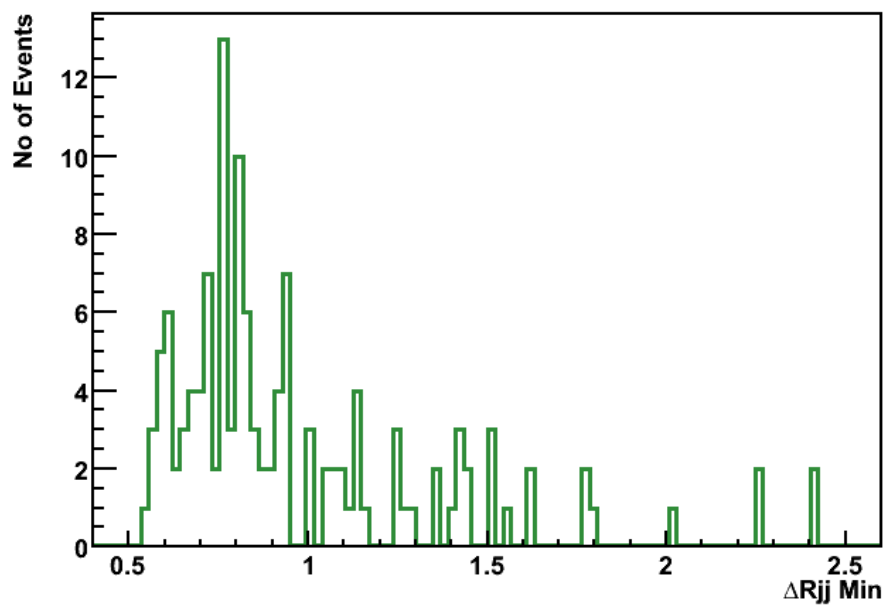
Figure 4.31: The minimum jet-jet separation for the background from the reconstructed particles. The peak is around 0.8.

Simulations will ultimately allow one to refine the kinematic cuts to eliminate as much of background as possible.

4.7 Future Directions

Right now, the CMS software is in a transition stage. The 'old' detector simulation software (OSCAR+ORCA) is being replaced by a newer version called CMSSW. In this study, the events are put into a format which can be used in the CMS software and fast simulations are performed. The next step should be to perform the same study with the CMSSW when it is ready. Having a full simulation of the detector would help to have a more realistic picture of the physics processes of interest.

After understanding the features of the signal, it would be possible to calculate the quantitative sensitivity bounds on the Higgs boson self-coupling by observing the change in adequate distributions (such as visible mass) with non-standard λ values and by performing the χ^2 based test.

Sensitivity limits should be calculated for different luminosity values and for different Higgs boson masses, assuming that SM is valid except for the Higgs boson self-coupling.

The final results should give a plot of $\Delta\lambda_{HHH}$ versus different Higgs boson masses, allowing us to see the lower and upper limits achievable for $\Delta\lambda$. Figure 4.32 is an example from U. Baur et al. of this kind of plot for theoretical research on Higgs boson self-coupling.
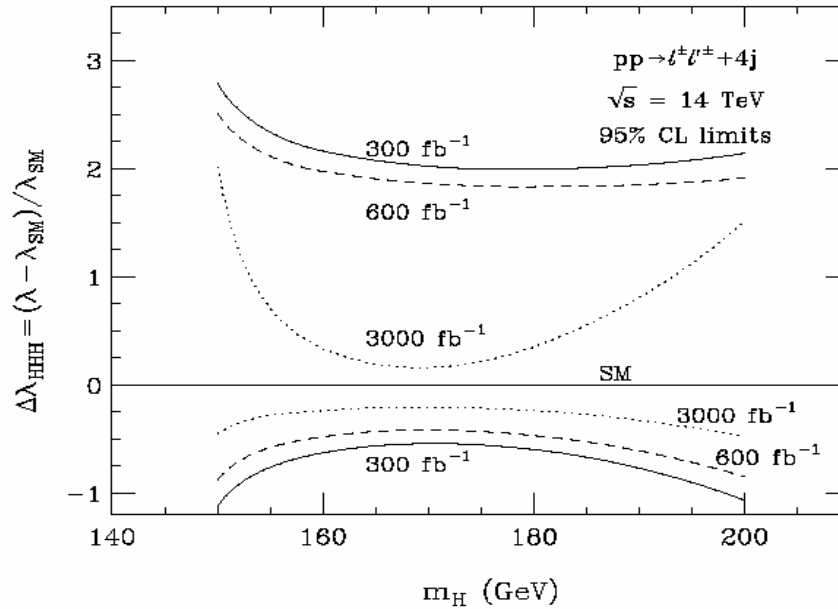
Figure 4.32: $\Delta\lambda_{HHH}$ versus different Higgs boson masses (in GeV) from U. Baur et al., (2002). The solid, dashed and dotted lines show the bounds for different luminosity values. (λ vanishes at for $\Delta\lambda_{HHH}$ = -1) [70].

4.8 Conclusion

In this study the gg $\rightarrow$ HH $\rightarrow$WWWW $\rightarrow$ μυjj μυjj signal channel is analyzed

along with the main background channel qq $\rightarrow$ WWWjj. The events which are generated

with a Fortran code by Baur et al., are first put into CMKIN where the parton showers are

created, and then the output is put into the fast detector simulation of the CMS (FAMOS).

While the original code had a smearing switch the events used in the simulation are

created without the smearing. Then, the sample output of this code with smearing is

produced. Every stage of the showering and detector simulation is compared to this

sample with smearing. It is seen that in many distributions, the mean values of the

detector output and of the theory with smearing are fairly close to each other.

Also, the generator level information obtained using reconstruction algorithms on the FAMOS output, is compared to the final detector output. The plots show that the mean values of the distributions are almost two times higher in the generator level case. This is believed to be due to reconstruction inefficiencies.

We conclude that better results can be obtained with the improvement of both detector simulations and the theoretical calculations. In the case of the detector, the reconstruction algorithms should be improved and the calibration of the detector should be performed. The cuts on the events should be studied in detail in order to find the ones which best eliminate the background and pileup caught by the detector. As far as the theory goes, additional parameters should be involved. The detector effect and the influence of the pileup and the effects of hadronization should be analyzed and included in the calculations.

CONCLUSION

The Large Hadron Collider which is designed to be the largest particle accelerator in the world, will provide new frontiers in physics. It will operate at very high luminosities and center of mass energies, allowing new physics discoveries. The Compact Muon Solenoid experiment is one of the four big experiments at the LHC. Its powerful magnet and muon detection efficiency makes it capable of studying many aspects of proton collisions at 14 TeV of center of mass energy. Its powerful magnet and muon detection efficiency are CMS detector's main features. This is a huge project that requires constant renovations and updates.

The first part of this thesis summarized the R&D studies performed on the hadronic calorimeter of the CMS experiment. Chapter I explained the tests and simulations performed on the air core light guides used in the readout system of the hadronic forward calorimeter. Light guides with three different reflected materials in them were tested for radiation hardness. Results show that the Type-1 AM reflective film lost almost 14% of light transmission capability after 10 Mrad of radiation, while the HEM and Type-2 AM lost only about 3%. It is seen that the reflectivity of aluminum on Mylar is not very resistant to radiation. This can partly be avoided by using a thicker aluminum layer. Also, the light transmission efficiencies of the three reflective films were compared using a blue LED (450 nm), a UV LED (380 nm), and a mercury light bulb. The results show that the Type-1 AM was more efficient than the other two in the UV range. Even though the Type-2 AM reflective film has poorer light transmission in the UV region, it is superior in visible region. Also, the HEM is a good reflective film in the visible range but transmits light at 30 % of that of the Type-1 AM in the UV region.

X-Y uniformity tests showed that the PMT X-Y uniformity improves and reaches a plateau when the HEM reflecting material is used instead of the AM. It is also observed that the straight and the tapered light guides give similar responses. Finally, the study of the reflective properties of different materials showed that German Mylar and HEM are better reflective materials than Al-Mylar for the 450 nm wavelength light.

After a few years of running, the luminosity of the LHC will be increased to 10^{35}cm^{-2}s^{-1}. During this period, which is referred to as the SuperLHC era, the scintillator plates used at the hadronic endcap calorimeter will lose their efficiency due to high radiation exposure. As a solution, we propose to substitute scintillators by quartz plates. We performed tests and simulations to find the most efficient way to collect the Čerenkov light from radiation hard quartz plates. The radiation damage tests performed at Argonne Laboratories showed that Polymicro FBP 600-660-710 solarization resistant quartz is the most radiation hard of the tested quartz types.

Different plates with different sizes and different embedded fiber geometries were investigated. Our studies showed that a quartz plate embedded with the Bar-Shape fiber geometry collects almost 70 percent of the light that the original HE tile would yield. The plate with the Bar-Shape fiber geometry is very uniform in light collection since the fibers are distributed uniformly throughout the surface. To improve the light collection, thicker quartz and smaller sized plates, and more embedded WLS fibers should be used.

According to the simulation results the surface non-uniformity is around 26% for the Bar- Shape, and the ratio of collected light with respect to the HE scintillator is around 70%. The mean arrival time is very small (< 4 ns) which makes quartz a good candidate in the SLHC era, since the photon arrival time will be within the gate.

The second part of the thesis consists of the physics simulations done on two different decay channels. It is crucial to study the decay channels in advanced in order to understand the deficiencies of the detector and to be able to 'act fast' when the data arrives. In the first chapter of the second half of the thesis, the detailed study on the MSSM channel b b H $\rightarrow$ $\tau\tau$, along with the Drell-Yan background channel, is performed to show different Higgs mass reconstruction methods and to analyze the effect of jet and missing transverse energy [MET] corrections on the mass reconstruction. This channel is very important towards understanding the MSSM since it has distinct kinematics that serve as a benchmark for tuning our reconstruction tools. Three reconstruction methods and three different jet corrections are studied. The methods known and used thus far do not work efficiently, and standard CMS jet correction methods do not give satisfying answers, though some of them go a short way towards improving the mass reconstruction. With the V1 jet correction method, it is possible to achieve slightly better distributions than the MC and Gamma jet correction methods. However, some of the algorithms shift the Higgs mass peak in the wrong direction. Since the missing transverse energy for this channel is very low, it is necessary to improve the MET using adequate jet reconstruction algorithms. It is important to realize the "error" in the reconstruction and find methods which work better.

Finally, in Chapter IV, the gg $\rightarrow$ HH $\rightarrow$WWWW $\rightarrow$ $\mu\upsilon$jj $\mu\upsilon$jj signal channel is analyzed along with the main background channel pp $\rightarrow$ WWWjj. The events, which are generated with a Fortran code by Baur et al., are first put into CMKIN where the parton showers are created, and then the output is put into the fast detector simulation of the CMS. The original code had a smearing switch, but the events used in the simulation are

created without smearing. Then, the sample output of this code with smearing is produced. Every stage of the showering and detector simulation is compared to this sample with smearing. It is seen that in many distributions, the mean values of the detector output and of the theory with smearing are fairly close to each other.

We conclude that closer results can be obtained with the improvement of both detector simulations and theoretical calculations. In the case of the detector, the reconstruction algorithms should be improved and the calibration of the detector should be performed. The cuts on the events should be studied in detail in order to find the ones which best eliminate the background and pileup caught by the detector. As far as the theory goes, additional parameters should be involved. The detector effect, the influence of the pileup and the effects of hadronization should be analyzed and included in the calculations.

At the end of this study, we conclude that the CMS detector and software requires some innovations and updates in order to better function. R&D studies are necessary to update the detector according developing conditions. Physics simulations help both to learn the signal channel of interest and to test the detector (software and performance). Extracting physics out of the data will be easier and faster thanks to these studies.

REFERENCES

[1] The CMS Collaboration, CMS Technical Proposal, CERN/LHCC 94-038, 1994.

[2] "CMS Outreach", http://cmsdoc.cern.ch/cms/outreach/html/ (accessed June 2, 2007).

[3]"How do physicists study particles? Discover the Cern accelerator complex", http://press.web.cern.ch/Public/Content/Chapters/AboutCERN/HowStudyPrtcles/CERN AccelComplex/CERNAccelComplex-en.html/ (accessed June 2, 2007).

[4] Journal of Physics G, Nuclear and Particle Physics, Review of Particle Physics, Institute of Physics Publishing, 2006.

[5] G. Flügge, Future Research in High Energy Physics. In N. Ellis and M. B. Gavela, editors, *1993 European School of High Energy Physics*, Yellow reports. CERN 94-04, 1994.

[6] H. Ballintijn et al., Heavy Ion Physics at the LHC with the Compact Muon Solenoid Detector, CMS Heavy Ion Proposal, 2002.

[7] The ATLAS Collaboration, ATLAS Technical Proposal, CERN/LCC 94-043, 1994.

[8] The ALICE Collaboration, ALICE Technical Porposal, CERN/LHCC 95-071, 1995.

[9] The LHCb Collaboration, LHCb Technical Porposal, CERN/LHCC 98-4, 1998.

[10] The CMS Collaboration, Physics Performance, Physics Technical Design Report, Volume 2: Physics Performance, CERN/LHCC 2006-021, 2006.

[11] F. Gianotti and M. Mangano, LHC Physics: the first one-two year(s), CERN-PH-TH, 2005-072, hep-ph/0504221, 2005.

[12] Claudia-Elisabeth Wulz, CMS Physics Overview, CMS Conference Report, CMS CR 2001-016, 2001.

[13] Norbert Neumeister, The CMS Experiment at the LHC, Status and Physics Potential, Czechoslovak Journal of Physics, Vol. 50, 2001.

[14] G. Bayatian et al., 1997c, CMS Magnet Technical Design Report, Technical Report 97/10, CERN LHCC, 1997.

[15] G. Bayatian et al.,1997d, CMS Muons Technical Design Report, Technical Report 97/32, CERN LHCC, 1997.

[16] G. Bayatian et al., 1998, CMS Tracker Project Technical Design Report, Technical Report, 98/6, CERN LHCC, 1998.

[17] G. Bayatian et al. 2000a, CMS TriDAS Project Technical Design Report, Volume 1, The Trigger Systems, Technical Report 2002/38, CERN LHCC, 2002.

[18] G. Bayatian et al., 2000b, CMS TriDAS Project Technical Design Report, Volume 2, The Data Acquisition System, Technical Report 2002/26, CERN LHCC, 2002.

[19] U. Akgun et al., Radiation Damage and Light Transmission Studies on Air Core Light Guides, IEEE TRANSACTIONS ON NUCLEAR SCIENCE, Vol. 53, No 3, 2006.

[20] U. Akgun et al., Comparison of PMTs from three Different Manufacturers for the CMS-HF Forward Calorimeter, IEEE Trans. Nucl. Sci., vol.51, pp. 1909-1915, 2004.

[21] U. Akgun et al., Complete Tests of 2000 Hamamatsu R7525HA Phototubes for the CMS-HF Forward Calorimeter, Nucl. Instrum. Meth., Vol A 550, pp. 145-156, 2005.

[22] J. Lachance, Radiation Induced Degradation of Polymeric Spacecraft Materials under Protective Oxide Coatings, Nucl. Instrum. Meth., vol B 185, pp. 328-335, 2001.

[23] A. M. Koehler, Radiation Damage of Mylar and H-film, Nucl. Instrum. Meth., vol 33, pp. 341-342, 1965.

[24] M. Ambrosio, Preliminary Results on Dielectric Mirror Damage due to the Radiation of a High K Undulator, Nucl. Instrum. Meth., vol A 25o, pp. 289-292, 1986.

[25] A. Braem, Metal Multi-dielectric Mirror Coatings for Cherenkov Detectors, Nucl. Instrum. Meth., vol. A 250, pp. 289-292, 1986.

[26] M. F. Webber, Giant Birefringent Optics in Multilayer Polymer Mirrors, Science, vol. 287, p.2451, 2000.

[27] P. Bruecken et al., Radiation Effect Studies on High Efficiency Mirror (HEM) and Aluminized Mylar for the HF Optical Design, CMS Internal Note, IN 2002/031, 2002.

[28] U. Akgun et al., CMS HF Calorimeter Light Guide System Radiation Damage Studies, CMS Internal Note,CMS-IN 2003/029, 2003.

[29] U. Akgun et al., Tests of the CMS-HF Light Guide System at the University of Iowa PMT Test Station, CMS Internal Note, CMS-IN 2002/029, 2002.

[30] F. Gianotti et al., "Physics Potential and Experimental Challenges of the LHC Luminosity Upgrade", hep-ph / 0204087, (2002).

[31] M. Bruzzi, "Recent results on the development of ultra radiation hard semiconductor detectors for very high luminosity colliders", http://lhc-workshop-2004.web.cern.ch/lhc-workshop-2004/2-overheads/16.2Bruzzi(fm).pdf/ (accessed May 15, 2007).

[32] The CMS Collaboration, The Hadron Calorimeter Project, Technical Design Report, CERN/LHCC 97-31, 1997.

[33] P. A. Čerenkov, Nobel Lectures in Particle Physics, New York, Elsevier, 1964.

[34] G. F. Knoll, Radiation Detection and Measurement, John Wiley & Sons, 1989.

[35] P. Bruecken et al., Radiation Damage in Quartz Fibers Exposed to Energetic Neutrons, CMS Internal Note, CMS-IN 2006/014, 2006.

[36] The People of Polymicro Technologies, The Book on the Technologies of Polymicro, Polymicro Technologies, 2002.

[37] "DuPont[TM] Tyvek", http://www.tyvek.com/ (accessed June 2, 2007).

[38] S. Agostinelli et al., Nuclear Instruments and Methods in Physics Research, NIM A 506, 250-303, 2003.

[39] M. Chiorboli, Supersymmetric Particle Reconstructions with the CMS Detector at LHC, Universita Degli Study di Catania, Ph.D. Thesis.

[40] F. Moortgat, Discovery Potential of MSSM Higgs Boson Using Supersymmetric Decay Modes with the CMS Detector, Universiteit Antwerpen, Ph.D. Thesis, 2001.

[41] S. Gennai, MSSM Higgs Searches with Tau Lepton Final States in CMS, hep-ex/0209044, v1, 2002.

[42] Particle Data Group, Particle Physics Booklet, Institute of Physics Publishing, 2006
.
[43] R. Kinnunen et al., Measurement of the H/A$\rightarrow \tau\tau$ Cross Section and Possible Constraints on tanβ, CMS NOTE 2004/027, 2004.

[44] A. Datta et al., Detection of MSSM Higgs Boson from Supersymmetric Particle Cascade Decays at the LHC, CERN TH 2002-375, hep-ph/0303095, v1, 2003.

[45] R. Kinnunen, Higgs Physics at LHC, CMS CR 2002/020, 2002.

[46] A. Heister et al., Measurement of Jets with the CMS Detector at the LHC, CMS NOTE 2006/036, 2006.

[47] P. Haifeng et al., Measurement of Missing Transverse Energy with the CMS Detector at the LHC, CMS NOTE 2006/035, 2006.

[48] The CMS Collaboration, Physics Performance, Physics Technical Design Report, Volume 1: Detector Performance and Software, CERN/LHCC 2006-001, 2006.

[49] F. Duru et al., Mass Reconstruction and Missing E_T Studies on MSSM A/H$\rightarrow \tau^+\tau^-$ Leptonic Decay, CMS Internal Note, CMS IN 2007/021, 2007.

[50] "JetMET physics object group", http://twiki.cern.ch/twiki/bin/view/CMS/JetMET/ (accessed May 15, 2007).

[51] R. Kinnunen and A. Nikitenko, Study of H$\rightarrow\tau\tau$ with Hadronic τ Decays in CMS, CMS NOTE 2003/006, 2003.

[52] D. Cavalli and G. Negri, Extension of the Study of A/H$\rightarrow \tau\tau\rightarrow$ Lepton – Hadron in the High m_A Region, ATLAS Internal Note, ATL-PHYS-2003-009, 2003.

[53] "IguanaCMS", http://iguanacms.web.cern.ch/iguanacms/ (accessed May 15, 2007).

[54] A. Nikitenko et al., Missing Transverse Energy Measurement with Jet Energy Corrections, CMS NOTE 2001/040, 2001.

[55] D. Rainwater and D. Zeppenfeld, Observing $H \rightarrow W^{(*)}W^{(*)} \rightarrow e^\pm\mu$ p_T in weak boson fusion with dual forward jet tagging at the CERN LHC, Phys. Rev. D 60, 113004, 1999.

[56] T. Plehn et al., Method for Identifying H$\rightarrow\tau\tau\rightarrow$e$^\pm\mu^\pm$p$_T$ at the CERN LHC, Physical Review D, 61, 093005, 2000.

[57] F. Pauss, LHC Physics, HEP Proceedings, 1998.

[58] C. Jarlskog, Fundamental Forces, Edited by D. Frame and K. J. Peach, SUSSP Publications, 1985.

[59] D. Griffiths, Introduction to Elementary Particles, John Wiley and Sons, 1987.

[60] F. Halzen and A. D. Martin, Quarks & Leptons: An Introduction Course in Modern Particle Physics, John Wiley and Sons, 1984.

[61] S. Weinberg, A Model of Leptons, Phys. Rev. Lett. 19, 1264, 1967.

[62] S. Glashow, Partial Symmetries of Weak Interactions, Nucl. Phys. B22, 579, 1961.

[63] LEP Collaboration, The LEP Electroeak Working Group, 2005.

[64] B. Volker and K. Jakobs, Higgs Boson Searches at Hadron Colliders, International Journal of Modern Physics Letters A, Vol.20, 2005.

[65] P. W. Higgs, Broken Symmetries and the Masses of Gauge Bosons, Phys. Rev. Lett., Vol. 13, 1964.

[66] F. Englert and R. Brout, Broken Symmetry and the Mass of Gauge Vector Bosons, Phys. Rev. Lett., 321, 1964.

[67] P. W. Higgs, Broken Symmetries, Massless Particles and Gauge Fields, Phys. Lett., Vol. 12, 132, 1964.

[68] F. Gianotti, Collider Physics: LHC, open-2000-293, 2000.

[69] T. Hambye and K. Riesselmann, Matching Conditions and Higgs Boson Mass Upper Bound Reexamined, Phys. Rev. D55, 7255, 1997.

[70] U. Baur, T. Plehn, D. Rainwater and Theory Group, Fermilab, "Determining the Higgs Boson Self Coupling at Hadron Colliders", hep-ph/0211224, (2002).

[71] S. Abdullin et al., Summary of the CMS Potential for the Higgs Boson Discovery, CMS NOTE 2003/033, 2003.

[72] C. Quigg, Gauge Theories of the Strong, Weak, and Electromagnetic Interactions, Frontiers in Physics, V. 56, The Benjamin/Cummings Publishing Company, Inc, 1983.

[73] A. Blondel, A. Clark, F. Mazzucato, "Studies on the Measurement of the SM Higgs Self-couplings", ATL-PHYS-2002-029, 2002.

[74] M. Spira, OCD Effects in Higgs Physics, hep-ph/9705337v1, 1997.

[75] U. Baur, T. Plehn, D. Rainwater, "Measuring the Higgs Self Coupling at the LHC and Finite Top Mass Matrix Elements", hep-ph/0206024, 2002.

[76] K. A. Assamagan et al., "The Higgs working Group: Summary Report 2003", hep-ph/0406152, 2004.

[77] M. L. Mangano et al., ALPGEN, a Generator for Hard Multiparton Processes in Hadronic Collisions, CERN-TH/2002-129, FTN/T-2002/06, hep-ph/0206293, 2005.

[78] "CTEQ4", http://www.phys.psu.edu/~cteq/fortran/pdfs/cteq4.f / (accessed June 2, 2007).

[79] "CTEQ6", http://user.pa.msu.edu/wkt/cteq/cteq6/cteq6pdf.html/ (accessed June 2, 2007).

[80] J. Pumplin, D.R. Stump, J. Huston, H.L. Lai, P.Nadolsky, W.K. Tung, "New Generation of Parton Distributions with Uncertainties from Global QCD Analysis", hep-ph/0201195, 2002.

[81] D. Stump, J. Huston, J. Pumplin, W.K. Tung, H.L. Lai, S. Kuhlmann, J. Owens, "Inclusive Jet Production, Parton Distributions, and the search for New Physics", hep-ph/0303013, 2003.

[82] "CMKIN, CMS KINematics interface with physics generators. A tutorial for new users", http://cmsdoc.cern.ch/~karimaki/cmkin/CMKINtutorial.html/ (accessed June 2, 2007).

[83] "CMKIN", http://www.uscms.org/LPC/lpc_simul/examples/web/CMKIN.html/ (accessed June 2, 2007).

[84] T. Sjostrand et al., PYTHIA 6.3 Physics and Manual, arXiv :hep-ph/0308153, 2003.

[85] S. Wynhoff, Fast Monte-Carlo Simulation in CMS, CMS IN 1999-037, 1999.

[86] S. Wynhoff, FAMOS: A Dynamically Configurable System for Fast Simulation and Reconstruction for CMS, Computing in High Energy and Nuclear Physics, eprint physics/0306052, 2003.

[87] S. V. Checanov, Jet Algorithms: A Mini Review, hep-ph/0211298, 2002.